Light Space Adaptive Removal of CCD Noise in Digital Images

by

Hilda Faraji

A thesis submitted in conformity with the requirements
for the degree of Master of Applied Science
Graduate Department of Electrical and Computer Engineering
University of Toronto

Abstract

Light Space Adaptive Removal of CCD Noise in Digital Images

Hilda Faraji

Master of Applied Science

Graduate Department of Electrical and Computer Engineering

University of Toronto

2004

In this thesis, we propose a denoising scheme to restore images degraded by CCD noise. The CCD noise model, measured in the space of incident light values (light space), is a combination of signal-independent and signal-dependent noise regions. This model becomes more complex in image brightness space (normal camera output) due to the nonlinearity of the camera response function that transforms image data from light space to image space. We develop two adaptive restoration techniques, both accounting for this nonlinearity. One operates in light space, where the relationship between the incident light and light space values is linear, while the second method uses the image space noise model to operate in image space. Both techniques apply multiple adaptive filters and merge their outputs to give the final restored image. Experimental results suggest that light space denoising is more efficient, since it enables the design of a simpler algorithm.

Dedication

Acknowledgements

Contents

Chapter 1

Introduction

1.1 Introduction

The past few decades have witnessed fundamental breakthroughs in image capture technology. Today digital cameras have replaced conventional cameras in many modern applications such as astronomy, microscopy, biotechnology, security, and consumer applications. The first commercial digital cameras came into the consumer-level market in mid 1990s. Today digital cameras are everywhere.

These cameras have advantages over film-based cameras. Factors such as a large need for digital images in the Internet, ease of image transmission via the Internet, no developing cost (in case of digital representation), LCD view screens, permanent storage without degradation, and high capacity storage, make them popular for commercial and consumer applications. The primary difference between a film-based camera and a digital camera is the image capturing method. Digital cameras incorporate image sensors instead of conventional film. Instead of relying on chemical or mechanical processes, images are recorded in an entirely electronic format. We now give a brief and simple description of digital camera operation. Further details are provided in the next section. The basic image formation procedure can be summarized as follows:

- A digital camera is exposed to the light coming from a scene.
- Photons arrive at the image sensor and are converted to an electrical charge due to a reaction between the light and sensor material.
- The electrical charge is then amplified and converted to a digital signal.
- A processor may perform some degree of compression of the digital data.
- The resulting image data is then stored in memory devices such as floppy disks, CDs, hard disks, or flash memories.
- Digital images can also be transferred to a computer and/or be printed.

The fundamental component in any digital camera is its image sensor. These sensors are able to detect and convert photons into an electrical signal. In many modern digital cameras, the light-sensors are based on semiconductor technologies such as Charge-Coupled Devices (CCD). CCDs are one of the most popular imaging devices due to factors such as high resolution, high quantum efficiency, low noise, fast response, and low power consumption [5]. This technology was invented in 1969 by Bell Telephone Laboratory researchers [9].

1.2 History

Digital camera technology is evolved from the same technology that was used to record television images. In 1951, the first video tape recorder (VTR) captured live images from television cameras by converting the information into electrical impulses (digital) and saving the information onto magnetic tape.

During the 1960s, NASA converted from using analog to digital signals with their space probes to map the surface of the moon (sending digital images back to earth). Computer technology was also advancing at this time and NASA used computers to enhance the images that the space probes were sending.

Texas Instruments patented a film-less electronic camera in 1972, the first to do so. In 1981, Sony released the Sony Mavica electronic still camera, which was the first commercial electronic camera. Images were were put into a video reader that was connected to a television monitor or color printer.

The first digital cameras for the consumer-level market that worked with a home computer via a serial cable were the Apple QuickTake 100 camera (1994), the Kodak DC40 camera (1995), the Casio QV-11 (with LCD monitor, late 1995), and Sony's Cyber-Shot Digital Still Camera (1996).

However, Kodak entered into an aggressive co-marketing campaign to promote the DC40 and to help introduce the idea of digital photography to the public. Kinko's and Microsoft both collaborated with Kodak to create digital image-making software workstations and kiosks which allowed customers to produce Photo CD Discs and photographs, and add digital images to documents. IBM collaborated with Kodak in making an Internet-based network image exchange. Hewlett-Packard was the first company to make color inkjet printers that complemented the new digital camera images.

Today the market has exploded with every major camera maker carrying a wide array of digital cameras, from those geared towards the amateur market to high-end professional models.

1.3 Image noise

Any electronic imaging system includes various sources of noise. Noise, and specifically electronic noise, is the introduction of any unwanted disturbance that interferes with proper reception of useful signals. As a result noise can distort the information carried by the signal. It happens in digital and analog systems and affects many sorts of data files such as text, audio, and images. Noise can be introduced to a signal in a variety of ways. It can be additive, multiplicative, independent or dependent of the noise-free

signal. If noise is a function of the signal, it is called "signal-dependent".

For a digital camera, noise sources such as random photon arrival, camera electronics, and compression noise impair the quality of digital images and limit the performance of a digital camera. These sources are introduced to the image in various stages of image formation.

In this thesis we address additive, signal-dependent sensor noise. Let I, n_I, and I_n denote the noise-free image, image noise, and noisy image respectively. The noisy image can then be described as

$$\begin{aligned} I_n(x,y) &= I(x,y) + n_I(x,y) \\ n_I(x,y) &= \mathcal{F}\left(I(x,y)\right). \end{aligned} \tag{1.1}$$

The dependency of noise on the noise-free image is embedded in the function $\mathcal{F}$. Parameters x and y represent the image coordinates. The following figures provide a visual representation of Equation 1.1. Figure 1.1 shows a noise-free image and the associated noisy image corrupted by simulated sensor noise. Depending on the type of noise, corrupted images look different.

Figure 1.1: Noise-free image(I) and the corresponding noisy image(I_n).

The refined image corresponding to the noisy image shown in Figure 1.1, is given in

Figure 1.2. As a result of applying our image restoration technique, noise in this image has been reduced to a large degree.

Figure 1.2: An example of filtered image using our image processing algorithms.

1.4 Objective

A variety of CCD noise sources can seriously restrict the ability to achieve high quality images with commercial sensors. Increasing resolution, applying super sensitive sensors, bringing down the compression rate, and implementing hardware-based filters all can lower noise to a large degree and therefore improve the image quality. However these techniques come at the expense of significant cost increases. In addition CCDs still exhibit inevitable noise sources such as photon noise.

To keep costs to a reasonably affordable level, and meanwhile reduce the noise effects, advanced image processing tools are needed to restore and enhance images degraded by noise and consequently make better quality images. The primary objective of this research is to design a post-processing software-based algorithms to restore images contaminated by the CCD noise sources outlined earlier. This algorithm could also be potentially valuable for hardware implementation. To approach the objective of image restoration, it is essential to address the following sub-objectives:

- finding the CCD noise model, and

- accounting for camera electronics in filter design.

1.5 Chapter description

This thesis begins with a description of CCD operation, noise sources, photon transfer curves, light space concept, and restoration filter concepts and derivation. In chapter three, we outline two novel methods for image restoration. One method is applied to the light-space representation of the image, and requires an estimate of the camera's photon transfer curve. The second method operates in image space but uses a noise model which is more complex than photon transfer curve due to the nonlinear mapping between the incident light and image intensities. The details of filter implementation are also given in this chapter. In Chapter four we show results regarding the acquired photon transfer curve, simulation results, and evaluate the performance of our filters based on a series of test images. We also compare the performances of our two denosing schemes and detail a parameter sensitivity analysis. The last chapter will provide the general conclusion of this research, with some discussion of future direction.

Chapter 2

Background

2.1 Introduction

In this chapter we initially provide the background on CCD operation and CCD noise sources. We then explain the concept of light space and nonlinear camera response function. Representation of noise model in light space is then described in the noise measurement section. The description of restoration filters with the main emphasize on adaptive smoothing filters are provided in the last section. We also review the literature related to CCD noise modeling and CCD noise removal techniques. Some of the previous work, addressing signal-dependent noise, is also illustrated in this chapter.

2.1.1 Image formation and CCD Noise Sources

This section addresses the geometry of image formation and provides information about the properties of CCD sensors and their noise sources.

A CCD chip is a semiconductor material which is divided into an array of picture elements or "pixels". When light photons strike the CCD chip, electrons are generated by a process known as the *photoelectric effect*. The electrons in each pixel are stored, transferred, and finally read out. The final image is then a representation of the electronic

charge at any pixel, which is expected to be proportional to the image brightness at that pixel. In what follows, we will describe these stages in details.

Image sensors

An important aspect of image formation is the behavior of sensors. The operation of digital cameras is mainly associated with image sensors. An image sensor is an analog integrated circuit that converts incoming photons into an electronic output.

The most common types of image sensors are Charge-Coupled Devices (CCD) and Complementary Metal Oxide Semiconductors (CMOS). These sensors are two different technologies used to generate electrical charge. Each of these types have their own advantages, depending on the application.

Both sensors convert photons to an electrical charge. The charge-voltage conversion (readout), however is conducted differently. Capabilities, limitations, and applications of CMOS and CCD image sensors are considerably different due to the difference in readout techniques. In CMOS image sensors the charge is converted to voltage at any pixel and most functions take place on the chip [12]. For CCDs most functions are integrated on the camera circuit board to which the CCD chip is affixed. Figure 2.1 gives the general structure of CCD and CMOS sensors.

CMOS sensors are superior to CCDs in terms of speed. Additionally, CMOS-based cameras are notably smaller than CCD cameras. This is because most functions are implemented on-chip. CCDs still have significant noise advantages over CMOS detectors and therefore offer superior image quality. Several factors such as less on-chip circuitry, and a common output amplifier make CCDs more tolerant to noise. On the other hand since the analog process circuitry is on-chip, CMOS detectors are more susceptible to noise. CMOS is a low-power sensor while CCDs use a process that consumes considerable power.

In summary CMOS sensors have some advantages over CCDs in applications where

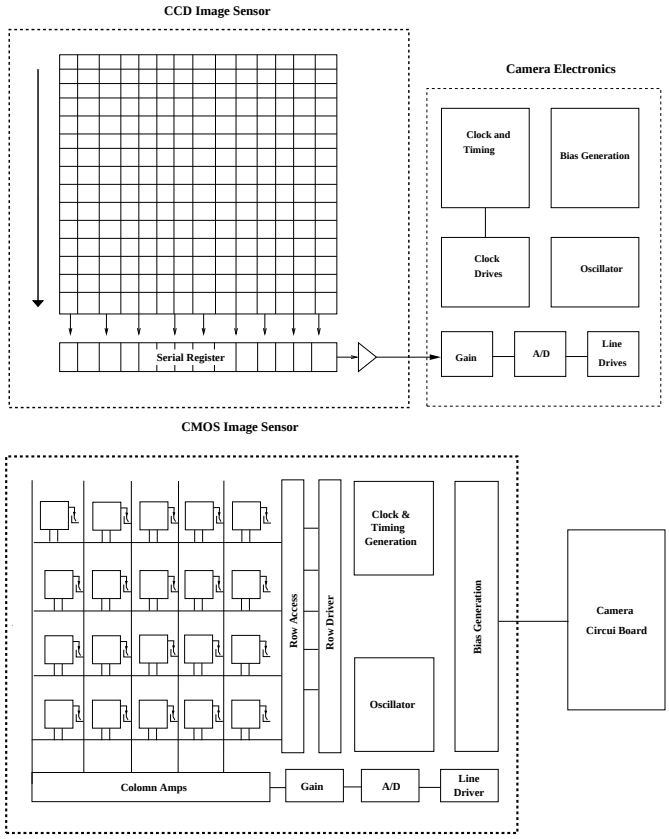

Figure 2.1: Simple sensor-camera architecture in CCDs (above) with most functions implemented off-chip and CMOS structure (below) with most functions take place on-chip.

high speed and low-cost are of main concerns [8]. For example they can be used for security cameras, videoconferencing, and fax machines. CCDs remain more suitable in high performance applications such as digital photography, astronomy, medical imaging, and broadcast television which require high image quality. As outlined earlier, throughout this thesis we will focus on CCD sensors.

2.1.2 CCD principles and operation

As a semiconductor device, the CCD is structured mainly of silicon. Germanium is sometimes used in place of silicon. In this research we always refer to silicon as a semiconductor material. The CCD structure can be described as a rectangular grid of electron-collection

sites (electrodes) over a silicon wafer, each used to record the amount of incident light. Each site is formed by growing a layer of silicon dioxide on the wafer. This layer is used as an insulator to protect the silicon layer [9]. The larger the grid, the larger number of pixels and hence higher image resolution. Figure 2.2 shows the CCD pixel layout.

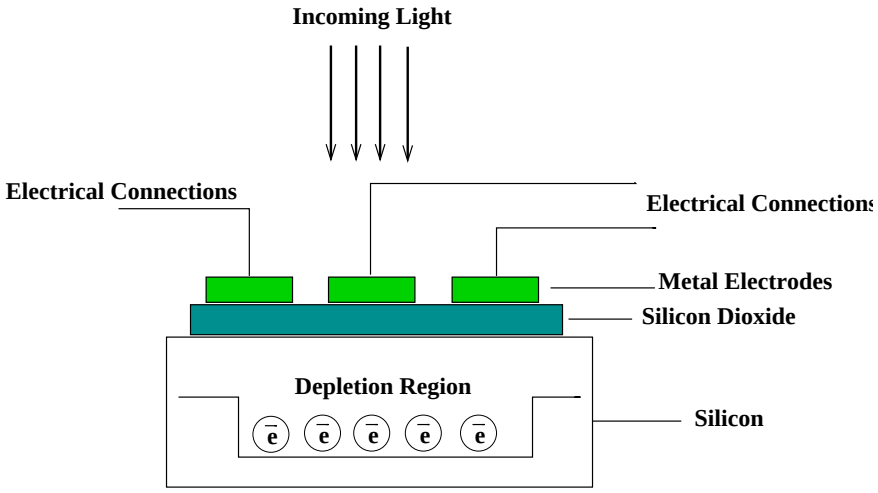

Figure 2.2: Simple pixel architecture. The location of electrodes above the silicon layer defines the pixels. A positive charge on the electrode, creates a depletion region in which the freed electrons are collected in the silicon layer.

Photons arriving at the electron collection site, are converted to an electrical charge due to a physical phenomenon known as the photo-electric effect. Photons with higher energy generate more electrons. Generally there are four major steps in CCD systems to create a digital image; (1) Charge generation (2) charge collection and storage, (3) charge transfer and finally (4) charge measurement [9]. These steps are explained below.

Charge generation

A basis of a CCD chip is the semiconductor crystal. Every crystal structure consists of atoms arranged in a regular lattice. The electrons in every atom posses different energy levels depending on how close they are to the protons. External energy can make electrons move from low energy levels or valance band and occupy higher energy levels or conduction band. Valence band refers to a an energy level filled with electrons in

which electrons can not move without applying the external energy. On the other hand electrons can freely move in the conduction band. This band is not filled with electrons [24]. Band-gap energy of a semiconductor is the energy separating the conduction band from the valence band.

If the photons arriving at the CCD sensors, can provide sufficient energy, they can excite the electrons from the valence band to the conduction band [25]. The required amount of the energy depends on the band-gap energy of the semiconductor material. If the energy of a photon is greater than the band-gap energy of the semiconductor material, electrons can move to the conduction level.

Photon energy is defined as:

$$E(photon) = \frac{hC}{\lambda} \tag{2.1}$$

where h is Planck's constant ($6.63 \times 10^{-34} \frac{m^2 kg}{s}$), C refers to the speed of light, and λ represents the wavelength. The band-gap energy of silicon is approximately 1.12 eV. In general, a silicon chip is responsive to photons with energy of 1.1 to 3.1 eV, covering the wavelength range of near infra-red and visible light. The number of electrons generated by one photon depends on the energy of the photon. Photons corresponding to very short wavelengths (shorter than visible) can generate more than one electron. With applying a positive electrical potential, the freed electrons can be moved, stored, and measured for further processing.

Charge collection and storage

The generated electrons are captured by a depletion region known as a potential well, and collected over a fixed period of time (Figure 2.2). This region attracts free electrons generated by the striking photons. Photons with higher energy can produce electrons in the potential well more effectively than longer wavelength photons.

In this stage, the number of electrons that a pixel can hold, and the ability of a pixel to collect the generated charge efficiently, are the most important parameters that need to be taken into consideration. However, the depletion region can only hold a limited number of freed electrons. When the number of electrons exceeds the limit, the pixel is "saturated". The pixel ability to collect electrons is perfect if there is no leakage to the adjacent pixels. The "Blooming" effect is a problem associated with the charge leakage to adjacent pixels as a result of an excess number of photoelectrons.

Charge transfer

The image from a CCD is read out by transferring rows of charge into a single horizontal register, followed by the transfer of individual pixel charges along the horizontal register toward a single output node for the final measurement (Figure 2.3).

This process is called charge coupling. During this process every charge corresponding to one pixel is transferred to the adjacent site. All the charge packets are transferred in parallel. Each parallel row is then transferred to a serial register. This register transfers each single charge to the output node where the read out takes place. After all the charges in the serial register are transferred to the output node, the next row of parallel charge is transferred to the serial register. This procedure continues until all the rows are read out [5].

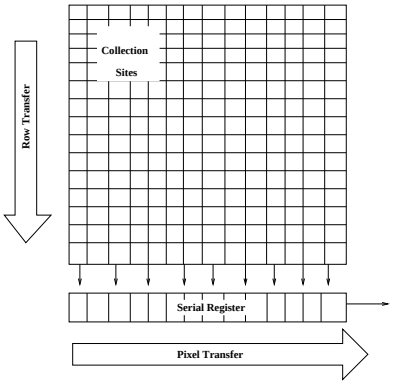

Figure 2.3: Charge transfer scheme.

Today CCD sensors are capable of transferring charge with 99.99% efficiency [9]. Therefore it is reasonable to neglect the noise associated with charge transfer inefficiency. Every pixel's electronic charge at the output node is then read out by a single output amplifier.

2.1.3 Charge measurement

As each pixel's charge reaches the output node, it is read by an output MOSFET amplifier. This amplifier generates a voltage for each pixel proportional to the signal charge transferred. An off-chip processor then amplifies the signal and through an Analog to Digital converter (A/D), the signal is quantized and thus the digital image is formed.

2.1.4 Noise sources

Any digital camera gives rise to noise, therefore resulting in uncertainty regarding the readout of a given pixel. Despite the remarkable improvements in CCD manufacturing techniques, raw CCD images still suffer from various noise sources. In what follows, we examine the main sources of noise in digital images.

Noise sources can be on-chip or off-chip. On-chip noises are associated with sensor noise, while off-chip noise, such as quantization noise, is inherent in the camera electronics. This thesis is limited to on-chip noise sources and their effect on digital images.

Some noise sources can be removed during the camera calibration procedures, while the remaining noise needs to be removed by a post-processing procedure. Although it is feasible to reduce the noise level created by CCDs, it is not possible to eliminate noise sources. The total electronic charge, transferred in a CCD, not only carries the useful signal, but it also includes electrons generated by noise components such as photon noise, read-out noise, or dark current. Descriptions of primary CCD noise sources as well as quantization noise are presented below.

- **Photon noise**- The presence of statistical variations and fluctuations in the photon flux at a given pixel is known as *photon noise* (or shot noise) and follows Poisson Statistics. In a Poisson distribution the amount of variation depends on the average number of photons, which is given by

$$n_s^{ave} = \rho T \tag{2.2}$$

where n_s^{ave} is the average number of photons, ρ is the number of photons hitting the sensor per second and T is the exposure time. For a large average value, the standard deviation of a Poisson distribution is the square root of the average value,

$$\sigma_{ns} = \sqrt{\rho T} \tag{2.3}$$

where σ_{ns} is the standard deviation of the photon noise. Since noise power is a function of average number of photons (noise-free signal), photon noise is signal dependent.

- **Dark current noise**- Charge in a CCD is generated by both the photoelectric process and also a thermal effect process. The latter generates an undesirable signal component known as dark current. Dark current increases the signal level. The model for dark current is the known formula:

$$I_d = 2.5 \times 10^{15} P_s I_{dc} T^{1.5} e^{\frac{-E_g}{2kT}} \tag{2.4}$$

where I_d is the average dark current, P_s is the pixel area (cm^{-2}), T is the operating temperature, E_g is the silicon band-gap energy(eV), k is Boltzmann's constant and I_{dc} is the dark current at 300K. Equation 2.4 shows that increasing temperature will result in larger dark current.

Additionally, dark current carries a statistical fluctuation known as *dark current*

noise. This kind of noise exhibits a Poisson distribution. Dark noise standard deviation is the square root of the average number of thermal electrons generated at a given temperature as

$$\sigma_{n_d} = \sqrt{I_d T_i} \tag{2.5}$$

where σ_{n_d} is the dark noise, I_d is the dark current, and T_i is the integration time. The longer the exposure, the more dark noise will be generated.

- **Readout noise**- This noise is introduced during the process of measuring the electronic signal on the CCD. The on-chip pre-amplifier accounts for the major component of read-out noise. This noise is usually modeled as white noise. Since this type of noise is spatially invariant, it is independent of the location of the pixel on the chip. This is the dominant noise in low-level lighting. Readout noise in modern CCDs has been considerably reduced due to significant improvements in the amplifier technology [9].

- **Fixed pattern noise**- CCD cameras also suffer from a special kind of noise that is more prominent in higher light levels. Photo-response non-uniformity generates a special kind of noise called Fixed Pattern Noise (FPN). CCD fabrication process allows for slight differences in pixels' quantum efficiency and thus introduces different responsivities from one pixel to another. FPN is signal-dependent and its statistics are proportional to the original signal.

- **Quantization noise**- Quantization is one of the main sources of off-chip noise. Quantization noise can be modeled as a uniform noise with zero mean and variance of $\frac{1}{12}Q^2$ in the $[-0.5Q, 0.5Q]$ interval, where Q is the quantization step. This noise is introduced to the signal after passing through the A/D converter.

For short exposure times, readout-noise is the dominant noise, while photon noise

exceeds other noise sources at longer exposure times. Since SNR is higher at longer exposure time (photon-noise limited), by reducing the dark noise and read-out noise, we can achieve higher SNR and consequently better performance. Figure 2.4 shows the major noise sources being added in different stages to the CCD camera system.

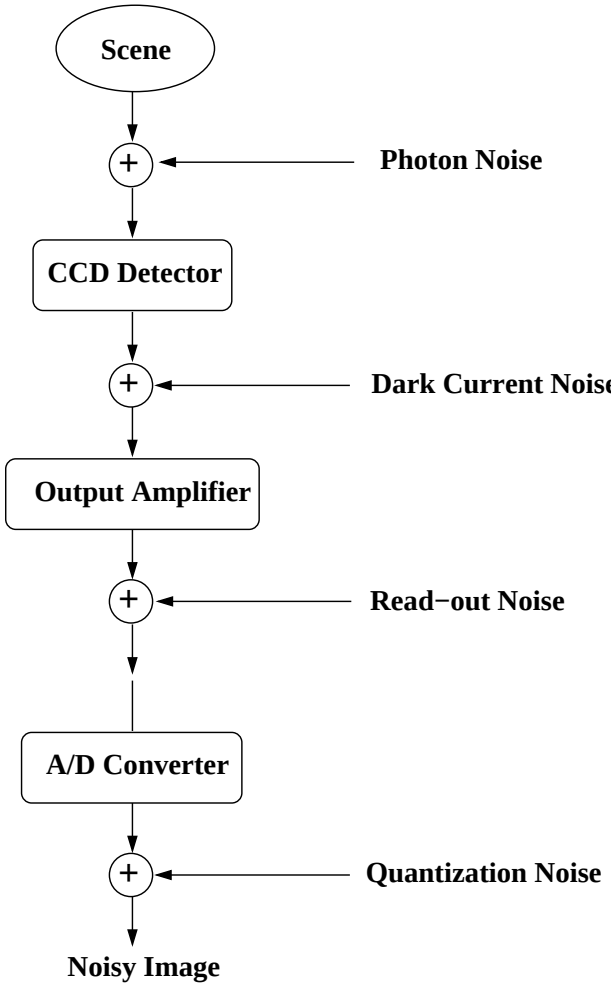

Figure 2.4: Main noise sources for CCD. At different stages different types of noise is added to the signal. Photon noise is due to the nature of light. Dark current noise and read-out noise are the main on-chip noise sources, while quantization noise is off-chip.

2.1.5 CCD noise removal

Several pre-processing procedures can significantly reduce the amount of CCD noise sources such as dark current and FPN. In practice, noise arising from dark current can

be significantly reduced by cooling the CCD [6]. In doing so it is feasible to reduce dark current generation to less than one electron per collection site per second [9].

Electronic noise sources such as readout noise in high performance CCD cameras are lowered by employing carefully designed electronics. In particular, to reduce on-chip amplifier noise, capacitances are reduced to allow greater sensitivity.

Fixed pattern noise can be eliminated by a process called "flat fielding". In this process, the sensitivity of all pixels are adjusted to the same level through a pixel-by-pixel division of the raw image data by a calibration flat-field image. Illuminating the camera by a standard uniform object produces a flat-field image. In this image, it is assumed that FPN accounts for the majority of variation among pixels. The results are then multiplied by the average value of the flat field image μ_F so that

$$I_C(x,y) = \mu_F \frac{(I(x,y) - I_{DC}(x,y))}{I_F(x,y) - I_{DC}(x,y)} \tag{2.6}$$

where (x,y) are the image coordinates, I_C is the calibrated image value, I is the original image value, I_{DC} is the dark current offset, and I_F is the flat-field image value.

Photon noise can not be removed via camera design [6]. This is because photon noise is associated with the nature of light rather than camera electronics. Therefore a post-processing algorithm is required to reduce its effect.

The work in [19] addresses the variation in a pressure sensitive paint (PSP) instrumentation system, which includes CCD image detectors for image detection. The two main CCD error sources are assumed to be shot noise and FPN. A general uncertainty analysis is utilized to characterize the two CCD noise sources. If $y = f(x_1, x_2)$, where parameter y represents the total image intensity, x_1 represents shot noise, and x_2 refers to FPN, propagation of errors in x_1 and x_2 to the output y is

$$\sigma_n^2 = \sigma_{x_1}^2 \left(\frac{\partial y}{\partial x_1}\right)^2 + \sigma_{x_2}^2 \left(\frac{\partial y}{\partial x_2}\right)^2 + 2\sigma_{x_1 x_2} \left(\frac{\partial y}{\partial x_1}\right)\left(\frac{\partial y}{\partial x_2}\right). \tag{2.7}$$

Here σ_n^2 is the approximate total CCD noise, $\sigma_{x_1}^2$ is the shot noise variance, and $\sigma_{x_2}^2$ represents FPN variance. Under the assumption of no correlation between these two noise sources, *i.e.* $\sigma_{x_1 x_2} = 0$, Equation 2.7 results in $\sigma_n^2 = \sigma_s^2 + \sigma_{FPN}^2$, where σ_s^2 is the variance of shot noise and σ_{FPN}^2 represents the FPN variance.

2.2 Light space versus Image space

This section will examine the concept of light space, comparametric equations and describe the nonlinear camera response function. It also discusses the effect of the response function on the noise model in image space.

2.2.1 Light space

Light itself is the electromagnetic spectrum ranging from short-wavelength subregions (such as X-ray) to very high-wavelength portions (such as infra-red). A camera measures the light intensity, or spectral power which is mainly a function of wavelength. The term *Light space* is defined as a linear representation of the photon flux. This space is a domain of quantifiable values known as "photo-quantities", denoted by q [18]. Light space image processing is then the processing of raw camera responses. Photo-quantity values, q, vary as a function of number of photons and the spectral response of sensor [17]. More specifically, q represents the quantity of light integrated over the spectral response of the camera. The value q can be found as

$$q = \int_{\lambda_l}^{\lambda_h} q_s(\lambda) s(\lambda) d\lambda \tag{2.8}$$

where q_s refers to the the number of photons hitting the image sensor, λ is the photon wavelength, and s is the spectral response of the sensor. Parameters λ_l and λ_h are the wavelengths beyond which the sensor spectral sensitivity is zero. The integration over wavelengths is due to the fact that photons of a scene object cover a range of wavelengths.

Moreover the energy of the photons are inversely proportional to their wavelengths and the spectral sensitivity of a typical camera sensor is not flat. Spectral sensitivity also varies from one camera to another and hence for two different cameras, the same number of photons may result in two different photo-quantity values.

Figure 2.5 gives the general components of the camera with respect to light space and image space. The quantity q refers to the light space image value, while I is the digital image value. Photons falling on the sensors are converted into electron charges and finally voltage. This voltage is shown in Figure 2.5 by the symbol q. Sensor noise is the noise which is associated with on-chip disturbances such as shot noise or pre-amplifier noise.

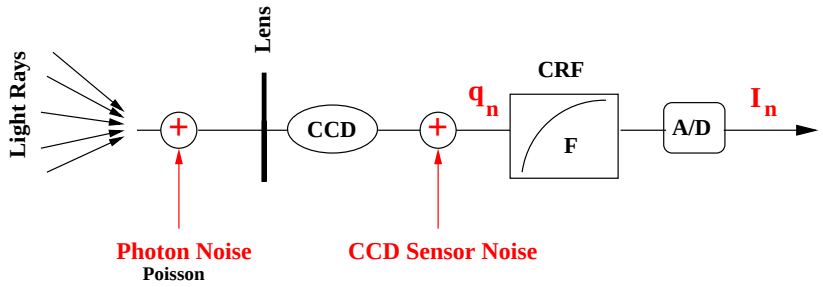

Figure 2.5: Digital camera main components.

An off-chip processor then converts the q values and the sensor noise into image values. In this stage image noise, due to camera electronics and quantization, is added to the image.

2.2.2 Camera response function

In an ideal imaging system, final brightness values are linearly related to the photo-quantity values, which are in turn a linear function of light. However, in image sensor systems (CCD or CMOS), there are several stages in the formation process, preventing a linear mapping between the image brightness and scene radiance. Nonlinear mapping between the raw sensor output and the digital responses might be designed into a cam-

era system if the dynamic range of the sensor itself is larger than that of the camera. This nonlinearity is then used to compress the large dynamic range to a smaller range of which the camera is capable of recording. In addition A/D conversion device may introduce more nonlinearity. As a result the overall camera system may exhibit a nonlinear response.

This nonlinearity is generally called the *camera response function* (CRF). The camera response curve is a plot of image intensity values versus the photo-quantity value q, which is assumed to be linearly related to the incident light. For low signal levels the response function can be approximated with a linear function with sharp slope. As the intensity grows, the nonlinearity becomes more evident and for the highest intensities it levels off. This is the saturation area. As an example, the Kodak DCS260 camera response function is shown in Figure 2.6.

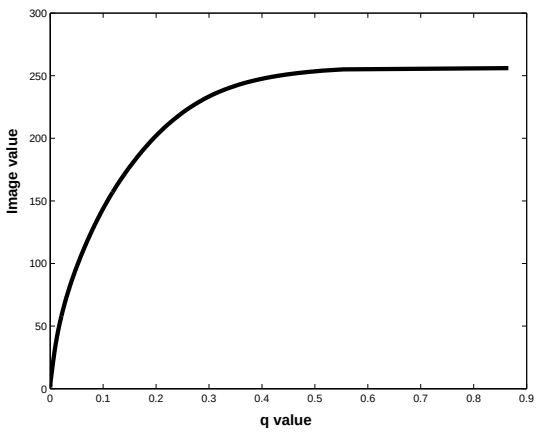

Figure 2.6: Kodak DCS260 camera response function.

For a typical still camera, the response function has a semi monotonic logarithmic shape. The function given in Equation 2.9 appears to be a good match for a large number of camera functions.

$$\mathcal{F} = \left(\frac{e^b q^a}{e^a q^b + 1}\right)^c \tag{2.9}$$

where parameters a, b, and c vary form one camera to another [15].

2.2.3 Comparametric equations

Comparametric equations can be used to compare sets of images, where the images differ only in exposure time. Such a set of images is known as a Wyckoff set [18]. In this set one image is considered as a reference image and the other images are defined as a function of this image. The reference image is assumed to have a unity exposure constant, and other images have relative exposure constants in terms of the reference image. Solving the comparametric equation results in the camera response function $\mathcal{F}$, with the constraints including semi monotonicity, $\mathcal{F}0) = 0$, and $g(0) = 0$. The general form of a comparametric equation is

$$\begin{aligned} f_i(\mathbf{m}) &= \mathcal{F}(k_i q(\mathbf{m})) \\ &= G(\mathcal{F}q(\mathbf{m}))). \end{aligned} \tag{2.10}$$

Here $\mathbf{m}$ denotes the image coordinates, f_i refers to the ith image with a scale constant k_i called the exposure ratio or the "comparametric ratio". This ratio is related to the shutter speed or exposure period. This period is the length of time for which the camera sensor is exposed to the light source. The longer the exposure time, the larger k_i. Parameter G refers to the nonlinear comparametric function relating the reference image to the image with k_i exposure time, and $\mathcal{F}$ is the camera response function.

To estimate $\mathcal{F}$ and k_i, at least two images taken with different shutter speeds are required. For instance let us consider two images of the same scene object with exposure ratios of k_1 and k_2 as given in

$$\begin{aligned} f_1(\mathbf{m}) &= \mathcal{F}(k_1 q(\mathbf{m})) \\ f_2(\mathbf{m}) &= \mathcal{F}(k_2 q(\mathbf{m})). \end{aligned} \tag{2.11}$$

We can then assume that f_1 is the reference image with unity exposure ratio. Therefore the second image f_2 will have the exposure k which is equal to $\frac{k_2}{k_1}$. As an example, Figure 2.7 shows two images in which the ratio $\frac{k_2}{k_1}$ is set to two.

Figure 2.7: An example of two images different only in exposure. The exposure ratio is 2 in this set.

Comparagram and Comparagraph

A *comparagram* is defined as a joint histogram between the two images different only in exposure. It refers to the plot of the comparametric equation. Due to the uncertainties in the image capturing process, this plot is not a thin curve and is rather spread out [14] (Figure 2.8). For example in case of a two-image set, corresponding to one intensity in the first image, there are multiple values in the second image. The degree of the spread depends on the amount of noise. By applying regression techniques, the comparagram can be fitted by a semi-monotonic function relating the two images. This slenderized curve is called *comparagraph*. Figures 2.8 and 2.9 show an example of a comparagram, and comparagraph. These graphs correspond to two images different only in exposure.

2.2.4 Camera function estimation

This function can be estimated by using a proper test chart with known reflection values. Also, we can recover the function using numerical methods such as solving the comparametric equation [14].

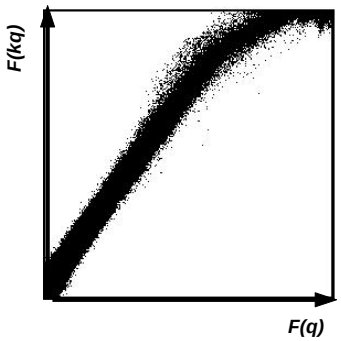

Figure 2.8: Comparagram corresponding the two images only different in exposure ratios.

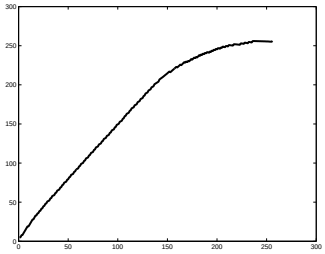

Figure 2.9: Comparagraph corresponding to two images only different in exposure ratios.

Standard estimation

The ground-truth camera response function can be accurately obtained by using a standard test pattern. Multiple images of the test chart with different exposure times can be used to obtain multiple pairs of $(q, \mathcal{F}(q))$. Since the reflectance of each bar is known, q can be assumed to be a known parameter. Also $\mathcal{F}(q)$ is simply the corresponding pixel value. Each image in the set generates a different camera function depending on the value of exposure constant k_i. In the logarithmic scale, the recovered camera functions are shifted versions of each other. The final step to produce the camera response function involves the proper alignment of these response functions.

Estimation using unrolling the comparagraph

This non-parametric estimation method involves solving the comparametric equation (Equation 2.10), and results in the camera response function. The unrolling process is

shown in Figure 2.10. A small value, q_0, is initially considered as a reference for which $\mathcal{F}(q_0) = q_0$. The corresponding value on the vertical axis results in $G(\mathcal{F}(q_0)) = \mathcal{F}(kq_0)$. If $\mathcal{F}(kq_0)$ is found along the x-axis, the comparagraph then gives $\mathcal{F}(k \cdot kq_0) = \mathcal{F}(k^2 q_0)$ along the y-axis. We can repeat the process to find $\mathcal{F}(k \cdot k^2 q_0) = \mathcal{F}(k^3 q_0)$ on the vertical axis.

Continuing this process determines multiple pairs of the form $(q, \mathcal{F}(kq))$, where q refers to a set of known values $\{q_0, kq_0, k^2 q_0, k^3 q_0, ...\}$. These data points can then be used by an interpolation method to generate the continuous format of the camera response function. The function is recovered as a lookup table which can be used to convert images into light space and vice versa.

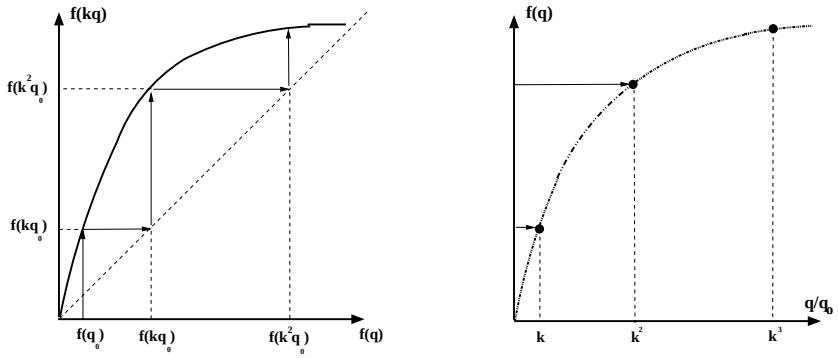

Figure 2.10: Comparagraph and the unrolling process (left). Final response function (right) [15].

2.2.5 Photo-quantity estimation

Once the camera response function, as well as the exposure ratio, are known, any image acquired by the camera can be converted to light space by applying the inverse of the camera response function, *i.e.*

$$q = \frac{1}{k_i} \mathcal{F}^{-1}(f_i(q)), \tag{2.12}$$

where q is the light space value, and $\mathcal{F}^{-1}$ refers to the inverse of the camera response. In the presence of noise, the estimated q values do not represent the true photo quantity values any more. One way to deal with this problem is to recover light space values using multiple images of the same object scene. The final estimate $\hat{q}$ can then be computed by a weighted averaging of multiple estimates [15].

2.2.6 Noise distribution in light and image space

Image noise can be found as the difference between the noisy image and the noise-free image. Assuming that noise originates in light space we can write

$$q_n = q + n_q, \tag{2.13}$$

where q_n is the noisy image in light space, q is the noise-free image in light space, and n_q is the CCD noise. Let n_I, I_n, and I denote the image noise, noisy image and the noise-free image respectively. Thus noise in the image can be written as

$$\begin{aligned} n_I &= I_n - I \\ &= \mathcal{F}(q_n) - \mathcal{F}(q) \\ &= \mathcal{F}(q + n_q) - \mathcal{F}(q) \end{aligned} \tag{2.14}$$

where $\mathcal{F}$ is the camera response function. For the notational simplicity we have dropped the coordinate indices. Expanding the Taylor series of $\mathcal{F}(q+n)$ about $\mathcal{F}(q)$ and ignoring the higher order terms results in

$$\begin{aligned} \mathcal{F}(q+n) &\approx \mathcal{F}(q) + \dot{\mathcal{F}}(q) n_q \\ \implies n_I &\approx \dot{\mathcal{F}}(q) n_q. \end{aligned} \tag{2.15}$$

Therefore the distribution of noise in the image not only depends on the noise distribution in light space but also varies according to the first derivative of the camera response function. Equation 4.1 also implies that image noise n_I is always signal dependent. A constant noise in light space results in a signal dependent noise in image space. As the derivative of the response function decreases, so does the power of noise in image space. The response function and the derivative of the response function are provided in Figure 2.11. Notice that the domain is in the logarithmic scale. The derivative begins with a sharp increase and gradually for high intensities approaches zero. In other words as intensity increases the noise power in image space begins to decrease sharply. It is

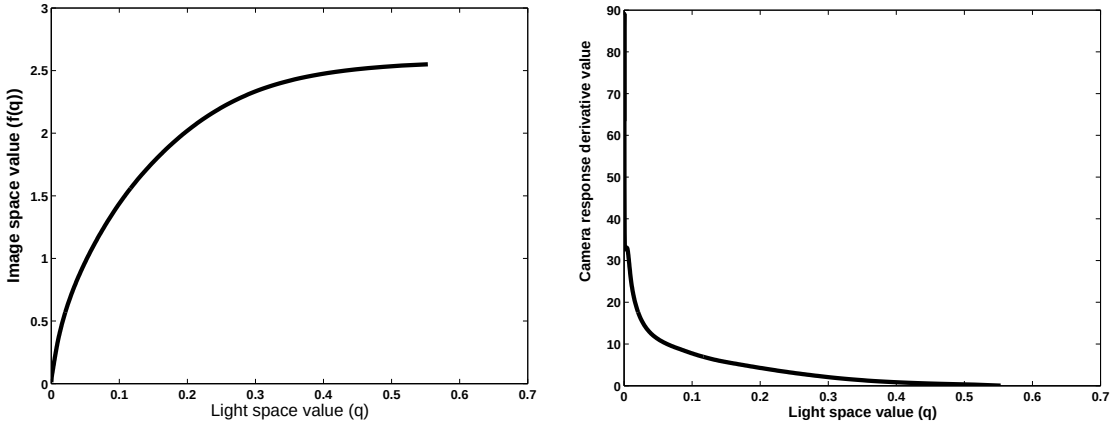

a b

Figure 2.11: Kodak DCS260 camera response function (a) and scaled derivative of the camera response function (b).

desirable to find the probability density function of the noise in image space in terms of the corresponding density function in light space. Let $P_{n_I}(n_I)$ and $P_{n_q}(n_q)$ represent the probability density function of image noise values and the corresponding density function in light space respectively. Statistically it is known that if

$$\begin{aligned} y &= G(x) \\ P_y(y) &= \frac{P_x(G^{-1}(y))}{\frac{dG}{dx}|_{x=G^{-1}(y)}}, \end{aligned} \tag{2.16}$$

therefore

$$\begin{aligned} n_I &\approx \dot{\mathcal{F}}(q) n_q = G(n_q) \\ P_{n_I}(n_I) &= \frac{P_{n_q}(G^{-1}(n_I))}{\frac{dG}{dn_q}|_{n_q = G^{-1}(n_I)}} \\ \Longrightarrow P_{n_I}(n_I) &= \frac{1}{\dot{\mathcal{F}}(q)} P_{n_q}\left(\frac{n_I}{\dot{\mathcal{F}}(q)}\right). \end{aligned} \tag{2.17}$$

Equation 2.17 gives the final distribution of the noise in image space in terms of the noise distribution in light space.

In what follows we will give an example of Gaussian noise in light space and determine the corresponding distribution in image space. Let us assume that a zero-mean Gaussian noise with a standard-deviation of σ is added to the photo-quantity values q. The density function of light space noise is then given by

$$P_{n_q}(n_q) = \frac{1}{\sqrt{2\pi}\sigma} e^{\left(\frac{-n_q^2}{2\sigma^2}\right)}. \tag{2.18}$$

The final density function in the image domain can then be found as

$$\begin{aligned} P_{n_I}(n_I) &= \frac{1}{\dot{\mathcal{F}}(q)} P_{n_q}\left(\frac{n_I}{\dot{\mathcal{F}}(q)}\right) \\ &= \frac{1}{\dot{\mathcal{F}}(q)} \frac{1}{\sqrt{2\pi}\sigma} e^{\left(\frac{-n_I^2}{2(\dot{\mathcal{F}}(q)\sigma)^2}\right)}. \end{aligned} \tag{2.19}$$

Therefore to the first order approximation of Taylor series, the distribution in image space is a mixture of Gaussian distributions. For any q_0, noise standard deviation in image space is $\dot{\mathcal{F}}(q_0)\sigma$.

Figure 2.12 shows that a single Gaussian noise in light space results in multiple noise distributions of which the standard-deviations vary as a function of $\dot{\mathcal{F}}(q)$. Higher image intensities will incorporate narrow Gaussian distributions as $\dot{\mathcal{F}}(q)$ is reduced.

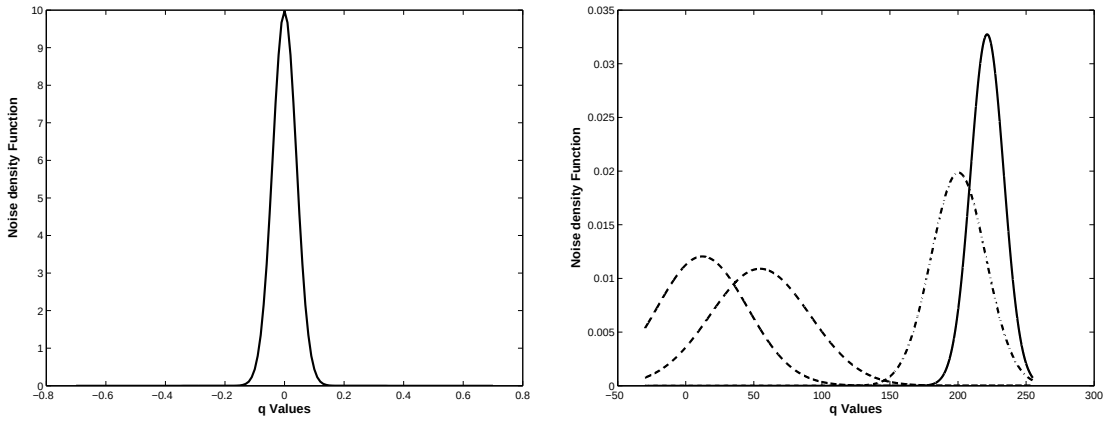

Figure 2.12: A single Gaussian noise in light space results in multiple noise distributions in image space. (left) Noise Gaussian distribution in light space and the example of four corresponding density functions centered at image intensities of 10, 55, 190, and 200 respectively (right).

2.2.7 The role of nonlinearity in image restoration

In image processing applications, which depend on the linear response assumption, it is important to verify that this assumption is not violated. For such applications, processing the raw camera responses leads to more satisfactory results when the sensor data is required or where the source of the defect in the image has originated in light space. Examples include expansion of image dynamic range using multiple exposures [14], quantimetric motion analysis [16], and eigen-tracking tracking in light space [13].

Motion analysis of image sequences assumes a constant exposure time for all the frames. But due to the existence of Automatic Gain Control (AGC), built in to many digital cameras, the exposure may vary from one frame to another, depending on the scene. As a result, well-known algorithms such as Brightness Constraint Constraint or eigen-tracking techniques fail. By correcting for nonlinearity, any change in exposure time is equivalent to multiplying an image by a scalar, which can be simply corrected.

Despite the importance of a nonlinear camera response on image restoration, its application has not been stressed in the literature. A *maximum a priori* (MAP) adaptive approach to the restoration of images recorded by nonlinear sensors in the presence of

signal-dependent noise is provided by Trussell and Hunt [26]. The adaptivity is achieved by sectioning the image into overlapping windows. For every section, the estimate of the noise-free values are achieved through an iteration-based technique. However their approach results in an iterative algorithm which suffers from heavy computational requirements [20].

In [20] a Wiener filter is applied for the restoration of images recorded by photographic film. A nonlinear mapping is considered between the incident light on the photographic film and the recorded image. In the proposed method this nonlinearity is incorporated into their image restoration algorithm by transforming the image into "exposure domain" in which there is a linear relationship between the degraded image and the noise-free image. The "exposure domain" [20] is a domain where there is a linear relationship between the image intensity and the incident light. It is similar to light space in that the sensor output is linearly dependent on the incident light.

Regardless of the type of image domain, the performance of denoising filters depends on knowledge of the noise model. This model, which is known to be simple in light space, is transformed by the camera response function to a more complex form. As an example, let us consider the Gaussian noise model mentioned in the previous section. Figure 2.13 shows a plot of noise standard deviation against image intensities in both light and image domains. The noise power in light space is almost constant (independent), whereas the noise curve in image space remains approximately steady up to the intensity of 3.49, followed by a mild increase until the intensity of 4.5. Beyond this intensity level we observe a steep fall.

Since the goal of this research is to remove CCD noise, it is of interest to apply the image restoration algorithms in light space. To do so, we convert the image to light space by applying the inverse of the camera response function, apply our restorations algorithm in this domain, and finally transform the filtered light space image to image space by applying the nonlinear camera response function.

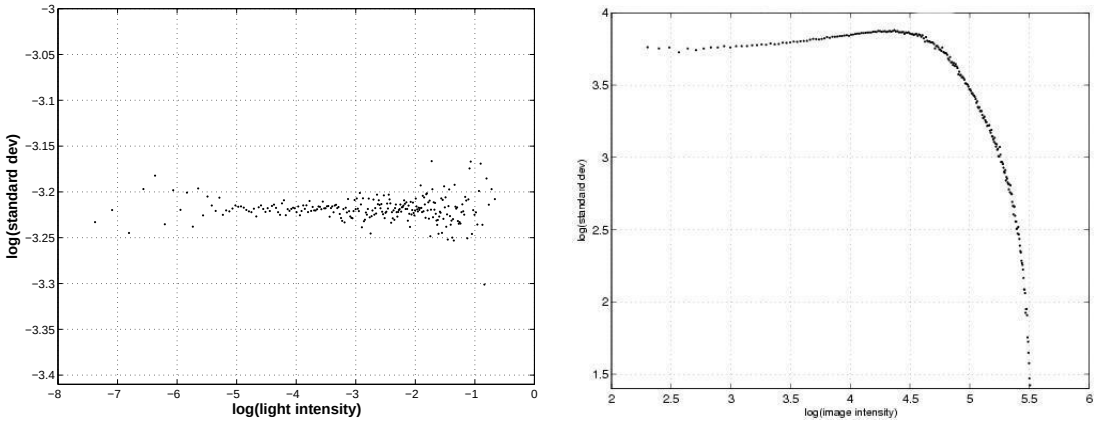

Figure 2.13: Plot of noise Gaussian standard deviation versus light space intensities in the logarithmic scale (left) and the corresponding plot in image space (right).

2.3 CCD Noise Measurement Techniques

Proper reduction of sensor noise calls for a proper modeling of the noise. Noise can be measured using a sensor model and a calibration scheme. Noise can also be plotted as the function of average image intensity.

2.3.1 Noise measurement based on sensor model in light space

The physical model for the sensor can be used to quantify the CCD noise [5]. The sensor model mentioned in the previous chapter can be utilized to measure CCD noise. Equation 2.20 illustrates the statistical properties of the sensor model as

$$I = A(Kq + N_{DC} + N_S + N_R) + N_Q \tag{2.20}$$

where q and I represent the light space values and the final noisy image values respectively, A is the output amplifier gain, K is a random variable having Gaussian distribution with unity mean and represents pixel sensitivity. This value is fixed for a given pixel location. The variation in K is associated with fixed pattern noise, which is due to the variation in pixel sensitivities. Dark noise is denoted as N_{DC}, N_s is the shot noise, N_r

refers to readout noise, and finally N_Q is the quantization noise.

If there is no correlation between different noise components, the total CCD noise variance can be formulated as the addition of the variances of the signal-dependent noise and the signal-independent noise. Equation 2.20 can then be rewritten as

$$Im = \mu + N \tag{2.21}$$

where $\mu = A(KI + \mu_{DC})$. Here μ represents the average image value, N represents the total noise, and μ_{DC} is the expected value of dark noise.

Let N_I denote the signal-dependent portion of the total noise and N_C be the independent component. Total noise can then be subdivided into independent and dependent components as

$$\begin{aligned} N &= N_I + N_C \\ N_I &= N_s A \\ N_C &= N_R + N_Q \\ \sigma_N^2 &= \sigma_I^2 + \sigma_C^2. \end{aligned} \tag{2.22}$$

The total noise standard deviation, σ_N, is the combination of standard deviation of the independent and dependent noise components. Since shot noise has a Poisson distribution, its variance is equal to the square of the average value. Therefore the signal-dependent noise variance is given as

$$\sigma_I^2 = A^2 \left(KI + \mu_{DC}\right). \tag{2.23}$$

The variance of the independent portion is

$$\sigma_C^2 = A^2 \sigma_R^2 + \frac{Q^2}{12}, \tag{2.24}$$

where σ_R^2 is the the read noise standard deviation, and Q is the quantization step so that N_Q has a uniform probability distribution over the range of $[-0.5Q, 0.5Q]$ [5]. To measure the CCD noise, multiple images corresponding to a standard uniform card are collected. Each pair of images is obtained at a different exposure level. From each pair the total noise and the average intensity are estimated. Independent noise variance and the total gain are then estimated using a regression technique. Some remarks are necessary here, first the camera response is assumed linear, second, the shot noise, corresponding to high intensities, is approximated by Gaussian noise.

Tsin *et.al.* [27] modify the model presented by Healey [5] by incorporating a nonlinear camera response function in the estimation process. The developed model is used to estimate the camera response function. The estimate of this function is through a maximum-likelihood procedure in an iterative fashion. In the estimated image model, it is assumed that the dark offset has been already removed by subtracting the dark offset from the images, and fixed pattern noise (FPN) is reduced by flat fielding (see Section 2.1.5). Therefore the the CCD output is modeled as combination of noise-free sensor output, shot noise and thermal noise. The final image intensity is modeled as a nonlinear function of sensor output, CCD noise components (shot noise and thermal noise) , and additive image noise such as quantization noise.

Photon Transfer Curve

Another alternative to generate the CCD noise model is to generate a noise curve, known as a photon transfer curve (PHTC). For CCD systems, a photon transfer curve is one of the calibration standards used as a performance criterion. A photon transfer curve can be used to model different variations of digital images due to CCD sensor noise. Obtaining an accurate photon transfer curve is crucial as it can be used as the base to model and characterize the CCD noise. Different CCD cameras are expected to generate similar photon transfer plots [9].

Figure 2.14 displays a schematic representation of a typical PHTC. This curve is the result of exposing the CCD to different light levels. It is a plot of standard-deviation of noise as a function of the average number of photo-electrons for any illumination. The number of photo-electrons represents the amount of illumination. The plot is in the logarithmic scale. As shown, this curve can be organized into three categories.

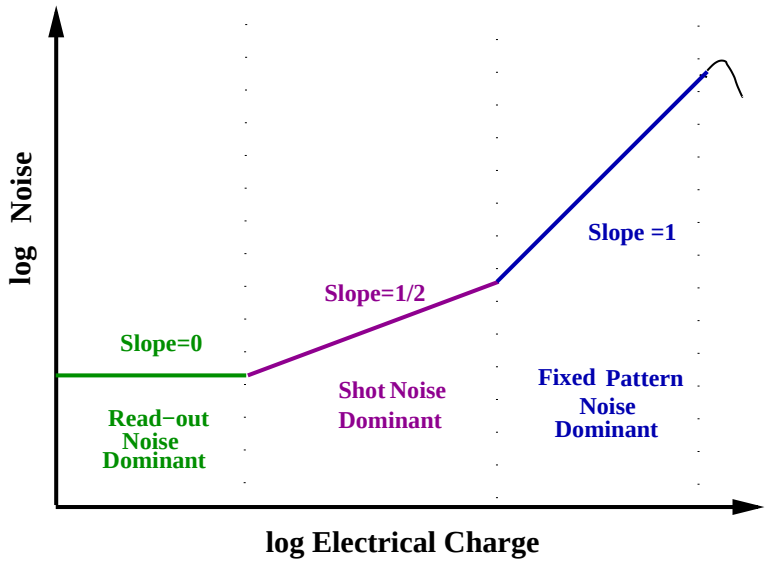

Figure 2.14: Photon transfer curve ([9]). It displays three noise regimes over the dynamic range of the CCD.

At the lowest signal level, the curve is almost flat. This fact shows that noise in the dark areas of the image is independent of the image value. Any independent type of CCD noise such as amplifier noise or shot noise generated by dark current, is the dominant noise under dark conditions.

As the illumination increases, noise becomes more signal dependent (non-zero slope). For the middle intensity range, a mild upward trend can be observed. This region is dominated by shot-noise. As mentioned earlier, this type of noise is due to the random arrival of photons, which usually exhibits Poisson distribution. If a random variable has a Poisson density function, its standard deviation is proportional to the square root of the average value. Therefore in the middle range a slope of $\frac{1}{2}$ can be observed.

The third part of the curve, corresponding to the light regions of the image, has a sharp rise in comparison with previous regions. Fixed pattern noise is the dominant noise in this region. Standard deviation of this type of noise is proportional to the original signal. Consequently the slope of the plot in the high intensity region is equal to one. This type of noise can be removed by a proper pre-processing procedure. And thus the third region can be treated as shot-noise limited.

Finally, the steep fall at the end of the FPN noise region is the result of a well-known photoelectric effect, namely the blooming effect. When a pixel is over-exposed, the charge overflows and it mixes with the charges of the adjacent pixels. The charge spread between pixels accounts for a sudden reduction in the noise components.

2.3.2 CCD noise model based on the PHTC

In [9], a photon transfer curve is used to characterize the CCD sensor noise. The model for noise variance in light space is somewhat similar to that presented in [27]. However, for low image intensities, independent noise with constant power is dominant and therefore the effect of shot noise is negligible. In the middle region, noise is modeled as purely shot noise. For high intensities FPN is dominant, but it can be removed by flat fielding.

The PHTC is pointed out to emphesize dominant CCD noise sources in [19]. But it is not used as a reference noise model. We use the PHTC as a noise model, but our approach is different from that presented here. Instead of one single model for all intensities, our model incorporates multiple noise models whose form depends on the dominant noise in the specific intensity region in the PHTC.

2.4 Restoration Filters

Image restoration refers to the problem of recovering an image from its noisy observation for the purpose of improving its quality. In mathematical terms, image restoration is an

ill-posed inverse problem. To overcome this problem, prior information about the actual image and the noise needs to be incorporated in restoration algorithms [23]. In doing so, the ill-posed restoration problem converts to a well-defined process in which an estimate of the actual image is determined from the degraded image using *a priori* information and constraints. Since prior knowledge of the image and the noise are not often available, it is necessary to model the image and noise. Hence the process of image restoration has two main stages: (1) modeling and identification, and (2) restoration.

Image restoration methods can be developed in spatial domain, frequency, a combination of time and frequency such as wavelet domain, or based on signal amplitude. Our denoising algorithm incorporates a combination of spatial and signal amplitude.

Restoration filters can be linear or nonlinear. The filter design depends on the image statistics and noise characteristics. Filters can be global or local. Global filters operate on the entire image. Examples include noise removal techniques in frequency domain. Local filters operate on a predefined neighborhood. Local filters use pixels from a local neighborhood to estimate the new value for a single pixel. Figure 2.15 shows the local region in which a 3×3 filter operates on an image. Typical window sizes are 3×3, 5×5, and 7×7.

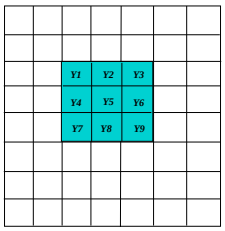

Figure 2.15: A local window for filtering operations. Parameters Y_i are the pixel values. A local filter restores the central pixel Y_5 using the values of the pixels in the window to generate the estimated value $\hat{X}_5$.

For a 3×3 window size, the center pixel in the local window is restored using the

neighboring pixels in the window, such that

$$\hat{X}_5 = \mathcal{T}(Y_1, Y_1, ..., Y_9) \tag{2.25}$$

where $\hat{X}_5$ is an estimate of the noise-free value of center pixel X_5 (before degradation). Here Y_i values represent the observed noisy version of the neighborhood pixels. To restore the entire image, the operator is moved across the image and each pixel is restored individually. In this section we will briefly characterize the derivation of a specific type of restoration filter, which will be applied to degraded images to address CCD noise.

2.4.1 Linear filtering

Linear filters are usually used when dealing with short-tailed noise distributions such as white Gaussian noise. If the function $\mathcal{T}$ in Equation 2.25 is linear, the restoration filter is linear. In this case the value of any pixel in the output image is determined by a linear combination of the values of the pixels in the input pixel's neighborhood as

$$\hat{x} = \sum_{m=1}^{M} a_m y[m] \tag{2.26}$$

where $\hat{x}$ is the output pixel, $y[m]$ represents the input pixels in the neighbor window, and M is the total size of the neighbor window. Parameters $\{a_m\}_{m=1}^{M}$ are the filter coefficients. For modeling purposes and notational simplicity images are defined as one-dimensional arrays of intensities.

Linear Minimum Mean Square Error (LMMSE) estimator

Optimal filtering of a noisy image is equivalent to the best possible estimation of the original image using the prior knowledge available. A class of methods that achieve this goal is generally known as Bayesian estimation. Let X and Yrepresent a noise-free image and the corresponding noisy observation respectively. The posterior conditional

probability of the original image $p(X|Y)$is given by

$$p(X|Y) = \frac{p(Y|X)p(X)}{p(Y)} \tag{2.27}$$

where $p(X)$ represents random variation in the noise-free data, and $p(Y|X)$ is a distribution encoding our beliefs about what the noisy version of X will look like. The *Minimum Mean Square* (MSE) estimate of X is the mean of the posterior density. Figure 2.16 shows a stochastic approach to MSE filters. This filter takes the corrupted version Y and attempts to estimate the original central point of the window.

We begin with a general assumption that there exist M random variables and the goal is

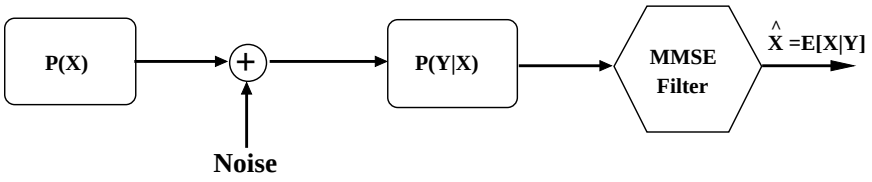

Figure 2.16: A stochastic approach to the linear MSE filter. $P(X)$ represents the random variation in a $N \times N$ window, and $P(Y|X)$ is a probability distribution corresponding to the noisy version of X. The MMSE filter estimates the original value in a least square sense [28].

to come up with a single scalar output as a linear combination of these random variables. If the data set is denoted as

$$\{y[0], y[1], ..., y[M-1]\}, \tag{2.28}$$

a class of affine estimators is of the form

$$\hat{x} = \sum_{m=0}^{M-1} a_m y[m] + a_M \tag{2.29}$$

Parameter $\hat{x}$ is a scalar representing the estimator result. The weighting coefficients are denoted as a_m.

The objective is to find the weighting coefficients to minimize the Bayesian MSE

$$\begin{aligned} Bmse(\hat{x}) &= E\left[(x-\hat{x})^2\right] \\ &= E\left[(x-\sum_{n=0}^{M-1} a_m y[m] - a_M)^2\right] \end{aligned} \tag{2.30}$$

where E represents the expected value, and $Bmse$ is the Bayesian error function. The resultant estimator is termed the *linear minimum mean square error* (LMMSE) estimator, which is a linear version of a MSE filter [10]. To determine the LMMSE filter coefficients, we differentiate $Bmse$ with respect to the weighting coefficients and set the results equal to zero. The coefficient a_M can be computed as

$$\begin{aligned} \frac{\partial}{\partial a_M} E\left[(x-\sum_{n=0}^{M-1} a_m y[m] - a_M)^2\right] &= 0 \\ -2E\left[x-\sum_{n=0}^{M-1} a_m y[m] - a_M\right] &= 0 \\ \rightarrow a_M &= E[x] - \sum_{n=0}^{M-1} a_m E(y[m]). \end{aligned} \tag{2.31}$$

We define vector $\mathbf{a} = [a_0, a_1, ...a_{M-1}]^T$ and $\mathbf{y} = [y_0, y_1, ...y_{M-1}]^T$. Replacing a_M in Equation 2.30 results in

$$\begin{aligned} Bmse(\hat{x}) &= E\left\{\left[\sum_{n=0}^{M-1} a_m(y[m]-E(y[m])) - (x-E(x))\right]^2\right\} \\ &= E\left\{\left[\mathbf{a}^T(\mathbf{y}-E[\mathbf{y}]) - (x-E(x))\right]^2\right\} \\ &= E\left[\mathbf{a}^T(\mathbf{y}-E[\mathbf{y}])(\mathbf{y}-E[\mathbf{y}])^T\mathbf{a}\right] \\ &- 2E\left[(x-E[x])(\mathbf{y}-E[\mathbf{y}])^T\mathbf{a}\right] + E\left[(x-E[x])^2\right]. \end{aligned} \tag{2.32}$$

Let $\mathbf{C}_{yy}$ denote the $N \times N$ covariance of $\mathbf{y}$, $\mathbf{C}_{xy}$ refer to the $1 \times N$ cross-covariance

vector with the property of $\mathbf{C}_{xy}^T = \mathbf{C}_{yx}$, and $\mathbf{C}_{xx}$ be the variance of x. Therefore $Bmse$ is rewritten as

$$Bmse(\hat{x}) = \mathbf{a}^T C_{yy}\mathbf{a} - 2\mathbf{a}^T C_{yx} + C_{xx}. \tag{2.33}$$

Differentiating $Bmse$ with respect to the vector $\mathbf{a}$ results in

$$\frac{\partial Bmse(\hat{x})}{\partial \mathbf{a}} = 2\mathbf{C}_{yy}\mathbf{a} - 2\mathbf{C}_{yx}. \tag{2.34}$$

Setting the derivation result equal to zero produces

$$\mathbf{a} = \mathbf{C}_{yy}^{-1}\mathbf{C}_{yx}, \tag{2.35}$$

And finally the LMMSE estimator [10] is

$$\begin{aligned} \hat{x} &= \mathbf{a}^T\mathbf{y} + a_M \\ &= \mathbf{C}_{yx}^T\mathbf{C}_{yy}^{-1}\mathbf{y} + E[x] - \mathbf{C}_{yx}^T\mathbf{C}_{yy}^{-1}E[\mathbf{y}] \\ &= E[x] + \mathbf{C}_{xy}\mathbf{C}_{yy}^{-1}\left(\mathbf{y} - E[\mathbf{y}]\right). \end{aligned} \tag{2.36}$$

Equation 2.36 reveals that the LMMSE filter only requires the first and second moments of the joint probability of $\mathbf{y}$ and x.

2.4.2 Order statistics filtering

If the function $\mathcal{T}$ in Equation 2.25 is nonlinear, the filter is nonlinear. Order statistics filters (OSF) form a general group of non-linear filters. These filters are more appropriate when dealing with long-tailed noise such as speckle noise. OSFs operate on a ranked set of neighboring pixels in an attempt to remove very high frequency effects while retaining edges. Given N observations $\{y_1, y_2, ...y_n\}$ of a random variable Y, the order statistics

are obtained by sorting the variables in ascending order satisfying

$$y_1^s \leq y_2^s \leq y_3^s .... \leq y_N^s \tag{2.37}$$

where $\{y_1^s, y_2^s, ...y_n^s\}$ represents the sorted observations of Y observation. The filter function is then defined as a linear combination of the sorted values

$$\mathcal{T} = \sum_i a_i y_i^s. \tag{2.38}$$

The rth order statistic filter is given by setting all a_i coefficients equal to zero except for a_r [21].

Median filtering

A median filter is a popular kind of nonlinear order statistic filter. In Median filtering the output pixels are computed by first selecting a neighboring window of pixels around a center pixel we wish to restore. Then the pixels in the window are ranked according to their brightness. The median value is then assigned to the output value. In terms of Equation 2.38, median filter has coefficients

$$a_i = \begin{cases} 1 & i = \frac{N+1}{2} \\ 0 & otherwise \end{cases} \tag{2.39}$$

where N is an odd number referring the size of the filter window. Median filters preserve edges better than linear averaging filters when dealing with long-tailed noise such as salt-pepper noise.

Trim mean

To obtain a robust estimate of the average value, trim mean filter can be used in place of a simple averaging filter. Trim mean is the combination of the OSF filter and the

averaging filter that calculates the mean by first sorting the data in ascending order and excluding the highest and lowest values of the observations. The percentage of rejection is a filter parameter, which can be set to different values. The higher the percentage, the more samples eliminated from the data set.

2.4.3 Adaptive filtering

It is known that local statistics in an image change from one region to another. This is called the "non-stationary" property. Human eyes seem to adapt to these variations. Also, noise characteristics may vary in different image regions. For instance, if the noise is signal-dependent, different regions will have different degrees of degradation depending on the average value of the image region. For these reasons a filter must have adaptive structure [21].

We use adaptive filters to learn the local signal and noise characteristics so that the filter parameters can be adjusted accordingly. Adaptive filter is a nonlinear filter since the coefficients change with the data. These filters treat each pixel as a random variable whose observed samples are within the $N \times N$ local window. The filter parameters are found by minimizing a distance between the noise-free and the estimated values. A typical schematic of an adaptive filter is provided in Figure 2.17.

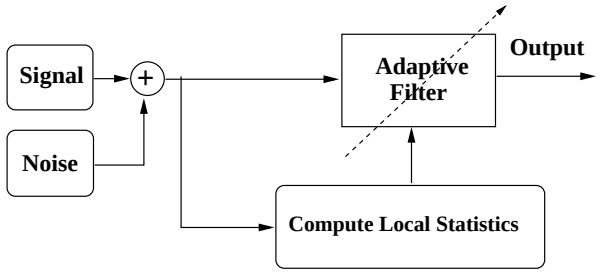

Figure 2.17: Simple adaptive filter block diagram.

Local LMMSE (LLMMSE) filter

At this stage we will explain the Local LMMSE derivation based on the LMMSE estimate derived in section 2.4.1. If

$$g = f + \eta, \tag{2.40}$$

where η represents the noise, the objective is to estimate f by $\hat{f}$, using the prior knowledge of a known noise model. Equation 2.36 can be rewritten as

$$\hat{f}_{LMMSE} = E[f] + \mathbf{C}_{fg}\mathbf{C}_{gg}^{-1} \cdot (g - E[g]) \tag{2.41}$$

in which $\mathbf{C}_{gg}$ and $\mathbf{C}_{fg}$ are the covariance and cross-covariance of the noisy and noise-free image, and $E[f]$ is the average image value. If the image in a vector form is $N \times 1$, $\mathbf{C}_{gg}$ is $N \times N$.

The problem of global minimization will be simplified to a local minimization procedure, if (1) noise is uncorrelated to the signal and (2) $\mathbf{C}_{ff}$ is diagonal. If noise is zero mean and uncorrelated to the signal, $E[f\eta] = E[f]E[\eta]$ is zero. The derivation of LLMMSE filter is based on a non-stationary-mean, non-stationary variance (NMNV) image model. Under this model, an image is decomposed to a non-stationary mean $E[f]$, and non-stationary residual component $f_0 = f - E[f]$. The first component represents the structure of the image, while the second provides the contextual information such as edges [3]. The expected value $E[f]$ can be estimated by sectioning method in which every pixel is replaced by averaging over neighbor pixels in a $N \times N$ window centered around the pixel. The correlation between adjacent pixels is implicitly embedded in $E[f]$ [4]. Image covariance $\mathbf{C}_{ff}$ is formulated as

$$\mathbf{C}_{ff} = E\left[f_0 f_0^T\right]. \tag{2.42}$$

The residual image f_0 is approximated by an uncorrelated non-stationary white noise process and is characterized by its non-stationary variance $\sigma_f^2(x, y)$. Therefore, based on the assumptions for residual image f_0, $\mathbf{C}_{ff}$ is diagonal. However, the regions around the edges in f_0 are correlated, thus violating the NMNV model.

The filter formula, denoted in Equation 2.41, can then be converted to a scalar point processor [4]. Let $(E[f] = \mu_f)$ and $(E[g] = \mu_g)$ be the local average of noise-free and noisy image respectively. As the noise is zero mean, it is clear that

$$\begin{aligned} E[g] &= E[f + \eta] \\ \rightarrow \mu_g &= \mu_f. \end{aligned} \tag{2.43}$$

Based on the diagonality assumption of the covariance of the noise-free image $(\mathbf{C}_{ff})$, the noisy image will also have a diagonal covariance matrix. To prove this, we assume that image g consists of only two elements, namely, $g(1)$ and $g(2)$. The covariance of g can be defined as

$$\begin{aligned} \mathbf{C}_{gg} &= E\left[(g - \mu_g)((g - \mu_g))^T\right] \\ &= E\left[\begin{pmatrix} g(1) - \mu_g(1) \\ g(2) - \mu_g(2) \end{pmatrix} \begin{pmatrix} g(1) - \mu_g(1) & g(2) - \mu_g(2) \end{pmatrix}\right] \end{aligned} \tag{2.44}$$

For notational simplicity, let $\mu_f(1) = \mu_1$, $\mu_f(2) = \mu_2$, $g(1) = g_1$, $g(2) = g_2$, $v(1) = v_1$, and $v(2) = v_2$. Here we will show that the non-diagonal elements of the matrix in Equation 2.44 are zero. The non-diagonal element, A, can be written as

$$\begin{aligned} A &= E\left[(g_1 - \mu_1)(g_2 - \mu_2)\right] \\ &= E\left[g_1 g_2 - \mu_1 g_2 - \mu_2 g_1 + \mu_1 \mu_2\right] \\ &= E\left[(f_1 + v_1)(f_2 + v_2) - \mu_1(f_2 + v_2) - \mu_2(f_1 + v_1) + \mu_1 \mu_2\right] \\ &= E\left[f_1 f_2 + f_1 v_2 + f_2 v_1 + v_1 v_2 - \mu_1 f_2 - \mu_1 v_2 - \mu_2 f_1 + \mu_2 v_1 + \mu_1 \mu_2\right] \\ \rightarrow A &= 0 \end{aligned} \tag{2.45}$$

All the terms in Equation 2.45 are zero, because noise is zero-mean and uncorrelated. Furthermore $E[f_1 f_2] = E[f_1]E[f_2] = \mu_1 \mu_2$ and $E[v1] = E[v2] = 0$. This can be generalized to the $N \times N$ matrix, and hence C_{gg} is diagonal. Also $\mathbf{C}_{fg} = \mathbf{C}_{ff}$. This is because

$$\begin{aligned} \mathbf{C}_{fg} &= E\left[(f - \mu_f)(g - \mu_g)^T\right] \\ &= E\left[(f - \mu_f)(f + v - \mu_f)^T\right] \\ &= E\left[(f - \mu_f)(f - \mu_f)^T\right] + E\left[(f - \mu_f)v^T\right] \\ &= E\left[(f - \mu_f)(f - \mu_f)^T\right] \\ &= \mathbf{C}_{ff}. \end{aligned} \tag{2.46}$$

Therefore any estimation parameter, $f(m)$, in Equation 2.41, will be correlated to one observed variable, $g(m)$. Finally the global estimate f_{LMMSE} can be simplified to an adaptive local optimization as

$$\hat{f}_{LLMMSE}(m) = E\left[f(m)\right] + \frac{\sigma_f^2(m)}{\sigma_g^2(m)} \cdot (g(m) - E[g(m)]) \tag{2.47}$$

where σ_g^2 and σ_f^2 are the local variance of noisy and noise-free image. If we rearrange the

above equation as

$$\hat{f}_{LLMMSE}(m) = \left(1 - \frac{\sigma_f^2(m)}{\sigma_g^2(m)}\right) E\left[f(m)\right] + \frac{\sigma_f^2(m)}{\sigma_g^2(m)} \cdot g(m). \tag{2.48}$$

It is apparent from Equation 3.6 that a f_{LLMMSE} filter functions as a weighted average of the local mean and the noisy observation. When the local image region is uniform, the estimated σ_f^2 is considerably smaller than the corresponding σ_g^2, causing the ratio $\frac{\sigma_f^2}{\sigma_g^2}$ to be close to zero. Thus the filter puts most of the weight on μ_g, smoothing the areas. Conversely, in the presence of a sharp edge, $\frac{\sigma_f^2}{\sigma_g^2}$ is close to one, and as a result the filter puts more weight on the noisy values, g [4]. In this case the edge sharpness is preserved.

However, local noise-free parameters σ_f^2 and μ_f are not available *a priori*, thus need to be estimated based on the noisy local variance σ_g^2 and local mean μ_g^2, and prior knowledge of noise model. Replacing σ_f^2 and μ_f in the LLMMSE filter formula results in an adaptive noise smoothing filter.

2.4.4 Filtering of signal-dependent noise

In this section we will explain how we can apply LLMMSE filters to images degraded by signal-dependent noise (SDN). Generally a degraded image can be modeled as [7]

$$\begin{aligned} g(m) &= f(m) + \eta(m) \\ \eta(m) &= H\left(f(m)\right)\mathcal{N}(0, \sigma_u), \end{aligned} \tag{2.49}$$

where $g(m)$ refers to the noisy image, and $f(m)$ is the original image. Function H in Equation 2.49 indicates the dependency of noise on the signal. The noise term $\mathcal{N}$ is assumed to be zero-mean, with variance of σ_u. The noise model expressed in Equation 2.49 is applicable in a large number of situations [7]. Most types of signal-dependent noise

can be expressed in a parametric form as in

$$\eta(m) = f^{\gamma}(m)\,\mathcal{N}(0, \sigma_u) \tag{2.50}$$

where parameter γ gives the dependency of noise on the noise-free signal and σ_u is the standard deviation of the independent Gaussian term $\mathcal{N}$ [7].

In what follows, we will show how Equation 3.6 converts to an adaptive noise smoothing (ANS) filter, given a known noise model. Here we will utilize the noise model expressed in Equation 2.50 to estimate the noise-free parameters in terms of the noisy ones. As mentioned earlier, since the Gaussian noise is assumed to be independent of the noise-free image, f, there is no correlation between f and the Gaussian noise, thus $\mu_f = \mu_g$.

Furthermore, the local variance of the reference image, $\sigma_f^2(m)$, can be expressed as a function of $\sigma_g^2(m)$. We know that

$$\begin{aligned}
\sigma_g^2(m) &= \mathrm{E}\left[g^2(m)\right] - \mathrm{E}[g(m)]^2 \\
&= \mathrm{E}\left[(f(m) + u(m))^2\right] - \mathrm{E}[f(m)]^2 \\
&= \mathrm{E}\left[f^2(m) + f^{2\gamma}(m)u^2(m) + 2f^{\gamma+1}(m)u(m)\right] - \mathrm{E}[f(m)]^2 \\
&= \sigma_f^2(m) + \sigma_u^2 \mathrm{E}[f^{2\gamma}(m)].
\end{aligned} \tag{2.51}$$

The term $E[2f^{\gamma+1}(m)u(m)]$ is equal to zero as the two signals are not correlated. We drop m for notational simplicity. To simplify the expression for $\mathrm{E}[f^{2\gamma}(m)]$, we use the Taylor series expansion of $f^{2\gamma}$ around μ_f, so

$$f^{2\gamma} \approx \mu_f^{2\gamma} + \frac{\partial f^{2\gamma}}{\partial f}|_{\mu_f} \cdot (f - \mu_f) + \frac{\partial^2 f^{2\gamma}}{\partial f^2}|_{\mu_f} \cdot \frac{(f - \mu_f)^2}{2}, \tag{2.52}$$

where μ_f is equal to $E[f(m)]$. Replacing the above expression for $E[f^{2\gamma}]$ results in

$$\begin{aligned} E[f^{2\gamma}] &= E\left[\mu_f^{2\gamma} + \frac{\partial f^{2\gamma}}{\partial f}|_{\mu_f}(f-\mu_f) + \frac{\sigma^2 f^{2\gamma}}{\sigma f^2}|_{\mu_f}\frac{(f-\mu_f)^2}{2}\right] \\ &= \mu_f^{2\gamma} + \mathrm{E}\left[2\gamma\mu_f^{2\gamma-1}(f-\mu_f) + 2\gamma(2\gamma-1)\mu_f^{2\gamma-2}\frac{(f-\mu_f)^2}{2}\right] \\ &= \mu_f^{2\gamma} - 2\gamma\mu_f^{2\gamma} + 2\gamma\mu_f^{2\gamma} + \gamma(2\gamma-1)\mu_f^{2\gamma-2}\mathrm{E}\left[f^2\right] \\ &+ \gamma(2\gamma-1)\mu_f^{2\gamma} - 2\gamma(2\gamma-1)\mu_f^{2\gamma}. \end{aligned} \tag{2.53}$$

We replace $E[f^2]$ with $(\mu_f^2 + \sigma_f^2)$ and the above derivation is summarized as

$$\begin{aligned} E[f^{2\gamma}] &= \mu_f^{2\gamma} + \gamma(2\gamma-1)\mu_f^{2\gamma-2}(\mu_f^2+\sigma_f^2) \\ &+ \gamma(2\gamma-1)\mu_f^{2\gamma} - 2\gamma(2\gamma-1)\mu_f^{2\gamma} \\ &= \mu_f^{2\gamma} + \gamma(2\gamma-1)\mu_f^{2\gamma} + \gamma(2\gamma-1)\mu_f^{2\gamma-2}\sigma_f^2 - \gamma(2\gamma-1)\mu_f^{2\gamma} \\ &= \mu_f^{2\gamma} + \gamma(2\gamma-1)\mu_f^{2\gamma-2}\sigma_f^2. \end{aligned} \tag{2.54}$$

At this stage σ_g^2 in Equation 2.51 will be written as

$$\begin{aligned} \sigma_g^2 &= \sigma_f^2 + \sigma_u^2\mathrm{E}[f^{2\gamma}] \\ \sigma_g^2 &= \sigma_f^2 + \sigma_u^2\left(\mu_f^2 + \gamma(2\gamma-1)\mu_f^{2\gamma-2}\sigma_f^2\right) \\ \rightarrow \sigma_f^2 &= \frac{\sigma_g^2 - \sigma_u^2\mu_f^{2\gamma}}{1+\gamma(2\gamma-1)\mu_f^{2\gamma-2}\sigma_u^2}. \end{aligned} \tag{2.55}$$

Therefore Equation 3.6 can be rewritten as the function of noisy image statistics, σ_g^2 and μ_g.

$$\hat{f}_{ANS}(m) = \mu_g + \frac{1-\sigma_u^2\cdot\frac{\mu_g^{2\gamma}}{\sigma_g^2}}{1+\gamma(2\gamma-1)\mu_g^{2\gamma-2}\sigma_u^2}\cdot(g(m)-\mu_g). \tag{2.56}$$

Equation 2.56 provides the formula for the ANS filter $\hat{f}_{ANS}$. This filter, even though it has the same form as the LLMSE filter, is in fact a nonlinear filter. The nonlinearity is due

to ratio of local variances (Equation 2.47) and their estimation by nonlinear functions of the noisy observation g. As indicated by Equation 2.56, when the statistics of the noisy image vary from one block to another, the filter adapts to local variations such that the uniform regions are smoothed, while edges and fine details are invariant to the averaging process. When the observation is too noisy, the ANS filter assigns more weight on the local average and for strong edge regions, it put more weight on the noisy image value $g(m)$. The ANS filter derived in Equation 2.56 can be applied in both image space and light space as long as the noise can be modeled as Equation 2.50.

2.4.5 Filtering of signal-independent noise

When dealing with additive signal-independent noise, *i.e.* $\gamma = 0$, σ_f^2 is simply equal to $\sigma_g^2 - \sigma_c^2$, where σ_c^2 is the variance of signal-independent noise. By this replacement Equation 3.6 converts to a pixel-wise Wiener filter:

$$\hat{f}_{Wiener}(m) = \mu_g + \frac{\sigma_g^2(m) - \sigma_c^2}{\sigma_g^2(m)} \left(g(m) - \mu_g(m)\right) \tag{2.57}$$

where m is the image location. The adaptive Wiener filter performs a two-dimensional, adaptive, noise-removal filtering, with the assumption that noise has constant power. These filters are superior to conventional Wiener filters in terms of edge preservation [29]. This is because they adapt for variations in local windows. It then estimates the local mean and variance of each pixel, based on statistics estimated from a local neighborhood of the pixel [11]. Mean and variance in a local $N \times N$ window are computed such that

$$\mu_g = \frac{1}{N^2} \sum_{i=1}^{N^2} g_i \tag{2.58}$$

$$\sigma_g^2 = \frac{1}{N^2} \sum_{i=1}^{N^2} \left(g_i^2 - \mu_g\right)^2. \tag{2.59}$$

Many attempts have been made to restore images degraded by signal-dependent noise

(SDN) [4], [2]. Kuan *et. al.* [4] use the NMNV image model to derive an adaptive, local LMMSE estimator to filter signal-dependent noise. Different types of SDN are addressed in this work. Nonlinear adaptive smoothing filters, with the same structure as LLMSE filters, are developed to reduce the effect of multiplicative noise and film grain noise. The noise-free local statistics are estimated from the noisy observations in the absence of prior information about the original image.

To reduce the effect of SDN noise Alparone *et. al.* [2] implement a wavelet-based LLMSE filter on the corrupted images in the wavelet domain. A noisy image is initially converted to the wavelet domain. After the wavelet coefficients are estimated using the LLMSE filters, the restored image is reconstructed.

Assuming that uniform patches are available in the noisy image, estimate of the noise parameters is trivial, as the filter formula is simplified when σ_f is set to zero [1]. Accurate estimate of noise parameters heavily depends on the successful identification of uniform patches in the noisy image. This important issue, however, has not been discussed in [1]. In general, detecting the uniform image regions in the noisy image is challenging when dealing with SDN and as a result the estimated noise parameters may not be accurate.

We also use a combination of adaptive smoothing filters, each of which corresponds to a specific noise model. In our scheme noise parameters are found using an estimated PHTC. Therefore there is no need to accurately find uniform patches in the noisy image. However, to deal with the artifacts around the edges after the filtering operation, we generate an edge map based on the ratio $\frac{\sigma_f^2}{\sigma_g^2}$ in local patches.

In summary, we have provided the background on which our restoration algorithm is based on. We first described the CCD operation and gave a brief description of the main noise sources such as dark current noise, photon noise, read-out noise and FPN. These dominant noise sources form the general noise model called the photon transfer curve. This curve is generated in light space, where there is a linear relationship between the incident light and light space values. We also explained the concept of light space and

the camera response function, which is used to convert the image to light space. Since CCD noise has signal dependent characteristics, the restoration algorithm needs to be based on signal-dependent noise-removal techniques. In the last section we showed the derivation of adaptive noise smoothing filters, which address signal-dependent noise.

Chapter 3

Procedure

3.1 Introduction

In the techniques described in this chapter, CCD sensor noise is addressed in both image space and light space. This chapter is organized as follows. First the CCD noise estimation procedure will be explained, followed by the general filter design procedure based on the noise model. We finally describe the performance measures used in this research. Our procedure can be summarized as

- Step 1: Modeling the CCD noise.
- Step 2: Developing a restoration algorithm based on the known noise model.
- Step 3: Evaluating the performance of the filters and comparing the results in light space and image space.

Based on our general denoising scheme as shown in Figure 3.1, we conduct two sets of experiments. The first set of experiments deals with filtering of noise in light space, while the second set attempts to restore degraded images in image space.

In light space, our denoising algorithm consists of three main stages. A noisy image is initially converted to light space by applying the inverse of the camera response function.

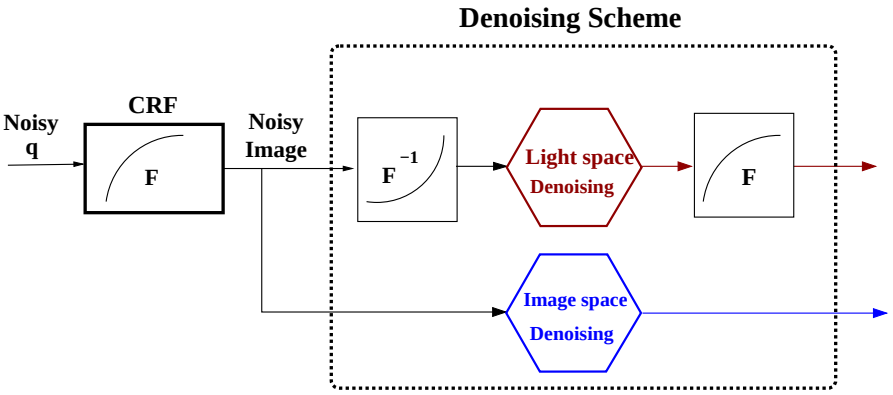

Figure 3.1: Our general denoising scheme. A noisy image can be filtered in both domains, as long as the noise model is known in each domain.

It is then processed using a combination of adaptive noise smoothing (ANS) filters with different window sizes and an adaptive Wiener filter. A weighted average of individual output images generates the final image, which is then converted back to image space by applying the camera response function. In image space we first estimate the noise model and develop filters based on noise characteristics in image space.

3.2 Noise parameter estimation in light space

Noise parameters in light space are estimated using the PHTC. Therefore the first step to estimate the noise parameters is to build the PHTC. As mentioned in Section 2.3.1, the PHTC is a logarithmic plot of signal (electric charge) against its noise variance. Even though light space is not the exact representation of electric charge, we continue to denote the PHTC as the light space noise curve. In the following section we describe how noise variance can be found for any noise-free intensity.

3.2.1 Experimental set up

We used a real scene and collected multiple images at a fixed exposure level. In this case the variations are computed in the temporal direction rather than spatial. Since

more samples yield more accurate statistics, a large number of images are collected. Our procedure of PHTC generation is summarized in four main steps as follows.

- We initially collect a series of images in the absence of light. The images are then converted to light space. The average of the dark images is considered as a dark offset image.
- Another series of images are collected at a fixed exposure level. The histogram of these images should ideally cover the image's dynamic range. These images are also transformed to light space.
- The offset image is then subtracted from these images in light space. The average of the resulting images are computed in the temporal direction.
- Samples corresponding to each intensity in the average images are collected over all the frames. The variance of the ensemble is computed. These variance values are used to construct the PHTC.

The key point in the performance of this procedure is the reduction of the effect of other external factors such as motion or variations in the source of illumination in the estimation. Such factors prevent the estimated noise data from being exclusively associated with CCD sensor variations and photon noise. The camera position is fixed during the experiments and we use three incandescent light bulbs which are evenly located around the object scene.

The offset image was determined by temporal averaging of a series of images in the absence of light. Let I_{OFF} denote the offset image, it can then be expressed as

$$I_{OFF} = \frac{\sum_j I_{D_j}}{J}, \tag{3.1}$$

where I_{D_j} is the set of dark images, and J is total number of dark images. Ideally all the pixels should have zero intensities in the offset image. However, due to several

noise sources as well as pixel manufacturing defects, this image may contain non-zero intensities. Using a threshold, we can also detect faulty pixels which exhibit abnormally high intensities in the images. These pixels are then excluded from further analysis.

After correcting for the dark offset, the resultant images are averaged together yielding the average image I_{ave}. In light space it is assumed that I_{ave} is approximately proportional to the average number of incident photons. Let I_k denote the kth frame in the sequence where $k = 1, 2, ...K$. The average image is

$$I_{ave} = \frac{\sum_k I_k}{K}. \tag{3.2}$$

The I_{ave} image is assumed to be an expected value or a noise-free image. In the average image all pixels with like intensities are identified and all the corresponding pixel values are collected over all the frames. Figure 3.2 shows an example in which multiple images at the same exposure level are used to collect samples of the same intensities.

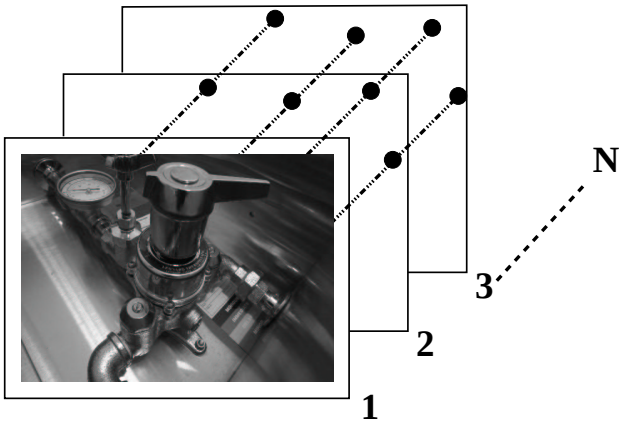

Figure 3.2: The estimation of statistics based on multiple images at the same exposure level. Samples of the same intensity, are collected in the temporal direction over all the N frames.

To improve statistics for photon transfer data, two thresholds are applied to the collected data. The first threshold is used to exclude the intensities with non-adequate number of samples. Care should be taken to make sure that for any intensity in the

average image, sufficient samples can be collected. At the end of this process, there is an ensemble corresponding to each intensity in the average image satisfying the above condition. We then use the second threshold to set a maximum limit for the number of samples. This makes the computation faster.

Noise variance is then calculated for all ensembles. For instance the standard deviation of samples in the ith ensemble is computed as

$$\sigma_i^2 = \frac{\sum_n (s_i^n - \mu_i)^2}{N} \tag{3.3}$$

where N is the number of samples in the ith ensemble, σ_i^2 is the ensemble variance with mean μ_i, and s_i^n represents a sample in the ensemble.

3.3 Simulation

We add synthetic noise according to a typical CCD PHTC. The simulation procedure works as follows. First a test image, assumed to be noise-free, is transformed to light space, then corrupted with noise. Since FPN can be removed by the flat-fielding technique, we can reasonably assume a two-region PHTC in which the FPN dominant region no longer exists. The first region, where readout noise dominates, is modeled as a constant independent zero-mean Gaussian with σ_c standard-deviation (Figure 3.3). On the logarithmic scale, noise in the second region is characterized by a straight line with the slope of γ and an offset of σ_u with respect to the origin:

$$\begin{aligned} \log(\sigma_{n_2}) &= \gamma \log(q) + \log(\sigma_u) \\ \rightarrow \sigma_{n_2} &= \sigma_u \cdot q^\gamma \\ \rightarrow \eta_2 &= q^\gamma \cdot \mathcal{N}(0, \sigma_u) \end{aligned} \tag{3.4}$$

where q refers to the light space value, σ_{n_2} denotes the noise standard deviation in the second region of the PHTC, $\mathcal{N}$ is Gaussian noise, and η_2 refers to the noise associated with the second noise region. Ignoring the FPN, the total standard-deviation of the simulated noise, σ_n, associated with a typical CCD sensor is formulated as

$$\sigma_n = \begin{cases} \sigma_c & f \leq e^B \\ \sigma_u \cdot f^{\gamma} & f > e^B \end{cases} . \tag{3.5}$$

where e^B is the border intensity at which the noise characteristics shift from signal-independent to signal-dependent. The simulated noise model in light space is shown in Figure 3.3. To evaluate the effect of noise parameters on the noise models and filtering performance, several noisy images corresponding to distinct values of γ and σ_u are generated.

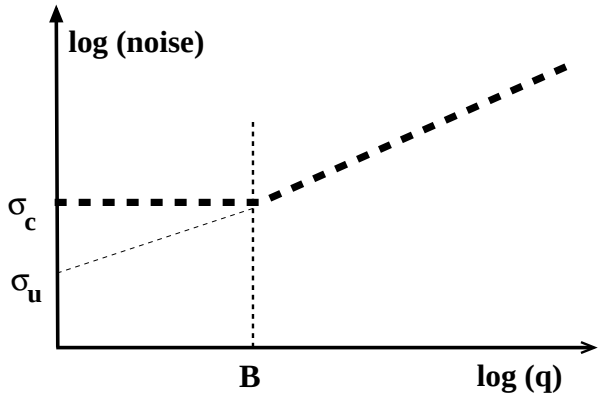

Figure 3.3: A linear representation of a two-region PHTC. The low signal level with constant noise ends at light space intensity e^B. The second region has a slope of γ and intercept of $\log(\sigma_u)$.

3.4 Noise model comparison in image space and light space

The noise model in light space is shown in Figure 3.3. To show the effect of the camera response function on sensor noise characteristics, we estimate the noise model in image space. To estimate this model in image space, the noisy image in light space is initially converted to image space. We then calculate the standard deviation of pixels whose intensities are equal in the noise-free image. To improve this process we only use those intensities for which there are adequate samples. Finally the noise model is a plot of noise-free intensities against the calculated standard deviations using a logarithmic scale. Any noise region is then approximated by a straight line. The slope yields the γ parameter and the intercept is σ_u in image space. We also use the estimated noise model in image space as a base for our restoration algorithm in image space. Figure 3.4 shows an example of a noise curve in image space, when the noise curve in light space is shown in Figure 3.4(a). The spread in the dark region (light space intensity less than e^{-5}) is due to presence of few dark areas in a typical image. The two-region noise model is transformed to a more complex noise model, which includes at least three noise regions as shown in Figure 3.4(b).

3.5 Restoration algorithm

Based on a typical CCD noise model, noise appears to be approximately signal-independent for dark areas and signal-dependent for other intensities. We describe two filtering approaches to address the two noise types. The first approach deals with SDN, while the latter attempts to remove the independent noise from the degraded images. These methods can be used in image space or light space, if the appropriate noise model is available. The filtering structure remains fixed regardless of which domain they operate on. Our

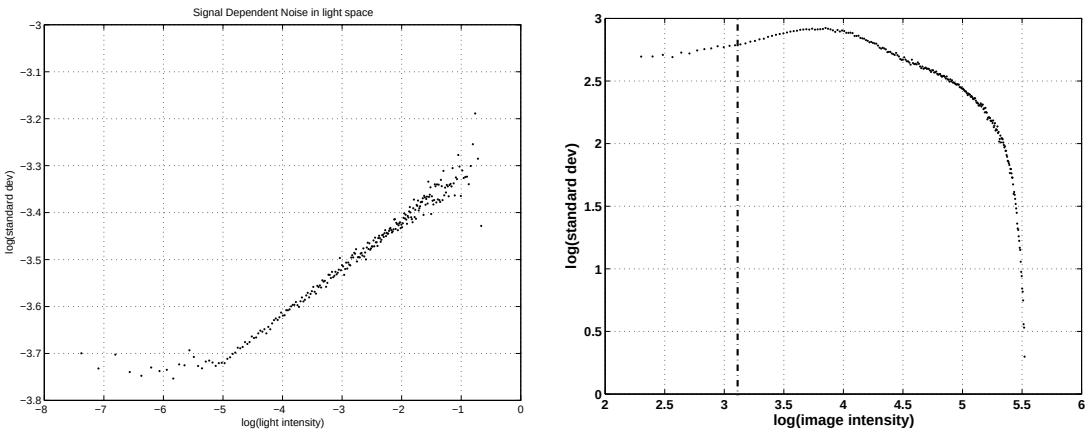

(a) (b)

Figure 3.4: Noise model in light space (a) and noise model in image space (b), which includes at least three noise regions. Vertical dotted line in (b) represents the image intensity at which the constant noise in light space shifts to signal-dependent noise.

restoration algorithm involves several steps, which are described in the following sections.

3.5.1 Adaptive noise smoothing filter implementation for SDN

We implement an adaptive noise smoothing (ANS) filter, which has the same linear form as the LLMSE filter. This filter is applied to the entire image. The target areas are the regions contaminated with SDN. As mentioned in Section 2.4.4, the formula for ANS filter is

$$\hat{f}(m) = \left(1 - \frac{\sigma_f^2(m)}{\sigma_g^2(m)}\right) E\left[f(m)\right] + \frac{\sigma_f^2(m)}{\sigma_g^2(m)} \cdot g(m) \tag{3.6}$$

where m refers to the image index, $\hat{f}$ is the estimate of the noise-free image, and g is the noisy image. The block diagram of the filter is shown in Figure 3.5.

Noisy local statistics are calculated over a uniform moving window of size $N \times N$.

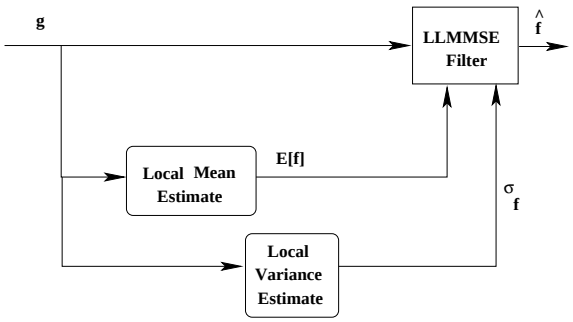

Figure 3.5: Structure of the adaptive smoothing filter used to deal with signal-dependent noise. Local noise-free mean and variance are computed based on the noisy image g and then fed to the filter. The output is the LLMMSE estimate of noise-free image.

Therefore for any local $N \times N$ region we have

$$\begin{aligned} \mu_g &= \frac{1}{N^2} \sum_n g(m) \\ \sigma_g^2 &= \frac{1}{N^2} \sum_n \left(g(m) - \mu_g\right)^2 \end{aligned} \tag{3.7}$$

where m is the pixel index in the local $N \times N$ window. To obtain a more robust estimate for μ_g, we also use a trim mean estimate to compute the local mean values. It should be noted that because the local windows do not have adequate samples, we can not set a high rejection percentage when estimating the trim mean values. Noise-free local statistics σ_f^2 and μ_f are estimated based on the noisy local variance σ_g^2, local mean μ_g, and prior knowledge of the noise model such that

$$\begin{aligned} \mu_f &= \mu_g \\ \sigma_f^2 &= \frac{\sigma_g^2 - \sigma_u^2 \mu_f^{2\gamma}}{1 + \gamma(2\gamma - 1)\mu_f^{2\gamma-2}\sigma_u^2}. \end{aligned} \tag{3.8}$$

The estimated local parameters are then substituted in Equation 3.6. Finally the center pixel in the local window is replaced by the estimate $\hat{f}$. To restore an entire image, the $\hat{f}$ operator is moved across the image and each pixel is restored individually.

The procedure to estimate the local statistics can be done separately from the filtering

algorithm. To ease the computation we combine the two operations and put the local estimate procedure as a part of filtering method as shown in Figure 3.5.

3.5.2 Filtering technique for signal-independent noise

For areas corrupted with signal-independent noise, the noise parameter γ is zero. The LLMMSE filter thus converts to a Wiener filter. We apply a standard adaptive Wiener filter to deal with signal-independent noise with known variance σ_c. This filter creates a pixel-wise Wiener filter using the local estimates μ_g and σ_g^2 [7]:

$$\hat{f}_{Wiener}(m) = \mu_g + \frac{\sigma_g^2(m) - \sigma_c^2}{\sigma_g^2(m)} \left(g(m) - \mu_g(m)\right) \tag{3.9}$$

where m represents the image index in the local window, and σ_g^2 is the estimate of variance in the local window.

3.5.3 Edge map

The estimation in Equation 3.7 assumes that local windows only contain samples from one distribution. It is clear that this assumption does not hold for edge areas, and as a result artifacts around the edges are created in the restored image. In the edge regions the estimated σ_g^2 is larger than the variance in either distribution existing in the local region. The mean estimate also deviates from the true values. The inaccurate estimate for σ_g^2 has a considerable effect on the filter output, since the local variance characterizes the edge information [4]. The bigger the window size the broader the distorted regions around the edges.

We deal with this problem by taking advantage of the fact that ANS filters with small window sizes create less artifacts, thus can considerably reduce this effect. On the other hand satisfactory performance in the uniform areas improves significantly by increasing the window size. To make the window size adaptive so that edge regions are filtered with

small window sizes, we apply two ANS filters, one with window of size 3×3 and the other with window size of 9×9, on the entire image.

To blend the outputs of these two filters so that the combined filter performs well in uniform patches while reducing artifacts, an edge map is generated. A raw edge map is initially generated by a neighborhood operation. This operator calculates the ratio between the estimated σ_f^2 to σ_g^2 for any pixel centered in a $N \times N$ window. This enables us to create an edge map in which all the pixels in the vicinity of edges are labeled as edge pixels. Small window sizes are not useful as they interpret any minor intensity variation as edge information. To remove the non-zero values not associated with edge regions, we multiply the raw edge map image by a thresholded binary image. The result is a binary image whose nonzero values represent edges. We use sensitivity analysis through which we find an acceptable range for the threshold that can be applicable for a large number of images. In this analysis, we degrade a series of test images equally, *i.e.* with the same noise parameters. After the raw edge map is constructed, its histogram is used to find a proper threshold. Finally the average of all thresholds is used as a fixed value associated with those specific noise parameters. Finally the binary map is smoothly expanded to let the edges diffuse throughout a small neighborhood, thus creating a smooth transition between the two adaptive smoothing filters. An example of an edge map corresponding to a small portion of "Lena" image is shown in Figure 3.6.

Let $\hat{f}_L$ and $\hat{f}_S$ denote the output images corresponding to the two ANS filters with large and small window sizes. The final output image at this stage is a combination of the two filtered image such that

$$\hat{f}_{LNMMSE}(m) = EG(m)\hat{f}_S(m) + (1 - EG(m))\hat{f}_L(m) \tag{3.10}$$

where m is the image coordinate, EG is the edge map in the range of $[0, 1]$, and $\hat{f}_{LNMMSE}$ is the Local Nonlinear Minimum Mean Square Error (LNMMSE) estimate. As indicated

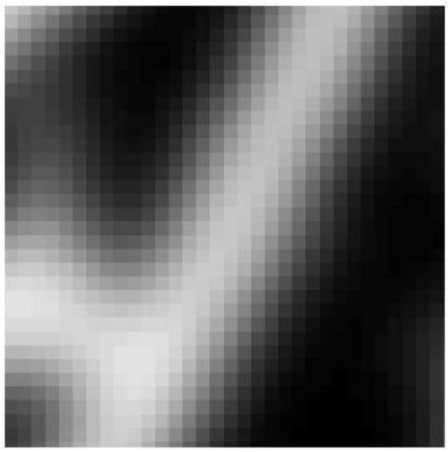

Figure 3.6: Cropped "Lena" edge map. High intensities in the edge map corresponds to the edges. Edges in the binary image diffuse over a small neighborhood to make a smoother transition between the two LLMSE filters.

by Equation 4.6, the two estimated filters $\hat{f}_S$ and $\hat{f}_L$ are combined so that the filter with smaller window size is dominant in edge regions, but gradually reduces its influence in uniform regions where the second filter becomes dominant.

Another alternative is to use a combination of an ANS filter and a median filter or adaptive Wiener filter. However these filters seem to blur the image as a result of making a wrong assumption about the noise model and thus, should not be used.

3.5.4 Intensity map

At this stage we need to design a weight function in order to merge the results of different noise regions in the noise curve. A intensity map is composed of several weight functions depending on the number of noise regions in the noise model. Denoising in light space calls for two weight functions because the noise model in light space only contains two regions as shown in Figure 3.3. In this domain, the intensity map assigns all the weight to the Wiener filter where the signal-independent noise is the dominant noise. For image intensities close to e^B, the output is the weighted average of two filters. The LNMMSE filter is dominant for image values beyond e^B by putting all the weight on the LNMMSE

filter. The weight graph is shown in Figure 3.7.

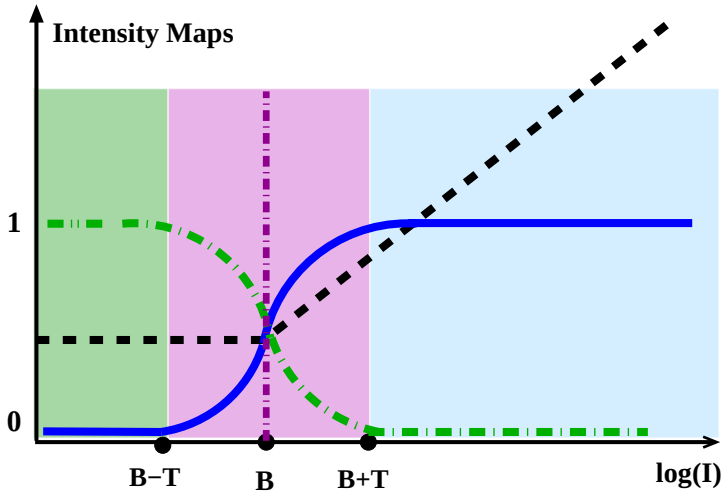

Figure 3.7: Sigmoid-like weighting functions (solid and dash-dot curves) provide a smooth mapping around the breakpoint e^B between the adaptive Wiener and LNMSE filters. The width of the overlap is determined by a threshold value denoted as T.

The final LNMMSE filter is smoothly combined with the output of the adaptive Wiener filter by superimposing two weight functions on the output images. We use a weight function which has a similar form to a sigmoid function. To do this, a region is considered around the border of the two noise regions. The threshold determines the width of this region. This threshold, which is a function of noise parameters, should be large enough to provide a smooth combination between the output images, and small enough to prevent a large influence of the filters on the wrong regions. Often we assign a larger threshold for images corrupted with more noise. As an example in light space (Figure 3.7), let τ denote the threshold value. For the first noise region, the first weight function consists of three portions. Corresponding to image values smaller than $e^{B-\tau}$ (dashed-dot curve), we assign values of one. In the overlap region the weight function monotonically declines. Weight function values for intensities larger than $e^{B+\tau}$, are set to zero. The second map (solid curve) is formed in a similar manner. It should be mentioned that in any image coordinate m, the weight coefficients sum to one, $W_1(I(m)) + W_2(I(m)) = 1$, where W_1 and W_2 are the two intensity maps shown in Figure 3.7 and I is the image.

In image space the noise model usually includes more than two regions, thus requiring more weight functions. Generally if there are K noise regions associated with a known noise model, K weight functions are used to combine the results of different outputs. All these weight functions have similar structures to those shown in Figure 3.8.

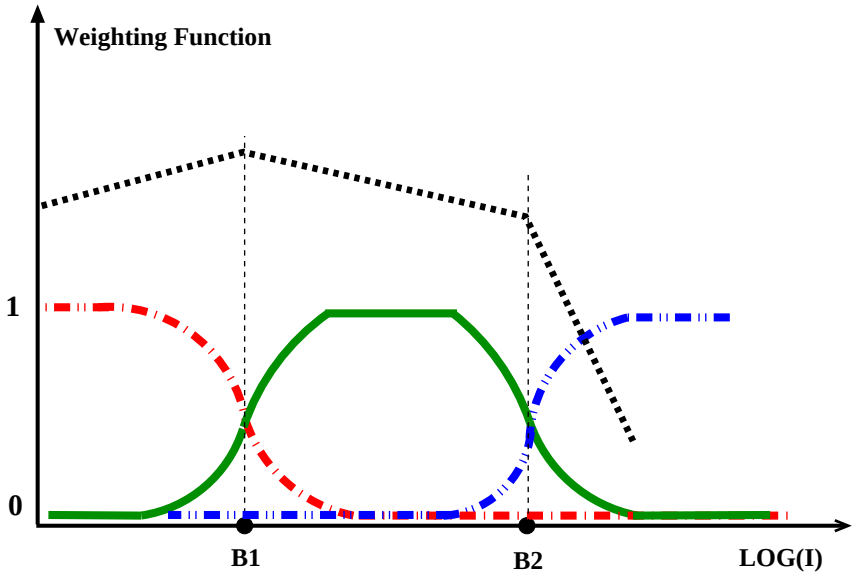

Figure 3.8: Three weighting functions (dash-dot, solid, and dash-dot-dot curves) provide a smooth combination of ANS filtered images around the noise curve knees e^{B_1} and e^{B_2}.

3.5.5 Final stage

The final output $\hat{f}_{Final}$ is the weighted average of all individual outputs as

$$\hat{f}_{Final}(m) = \sum_{k=1}^{K} W_k(m)\hat{f}_k(m) \tag{3.11}$$

where m is the image coordinate, K is number of noise regions, W_k and $\hat{f}_k$ are the weight function and the filtered image corresponding to the kth noise region. The summary of the denoising scheme in light space is shown in Figure 3.9.

Denoising in image space in general includes two or more weight functions, depending

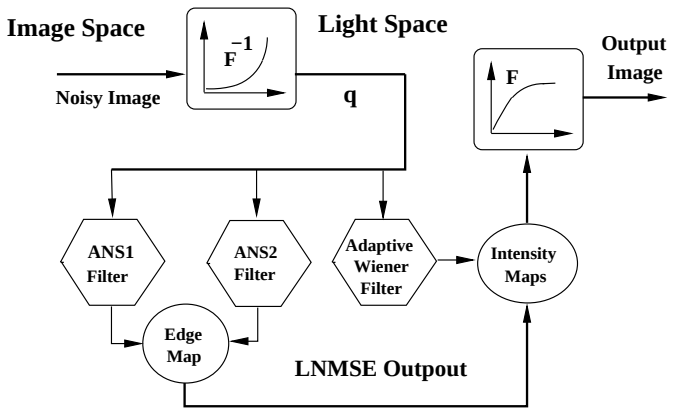

Figure 3.9: Our general filtering scheme in light space. A noisy image is initially converted to light space, then processed using a combination of adaptive noise smoothing filters with different window sizes and an adaptive Wiener filter. The final image is a weighted average of output images. This image is then converted back to image space.

on noise regions in the noise model. Figure 3.10 shows our general hierarchical denoising scheme in image space.

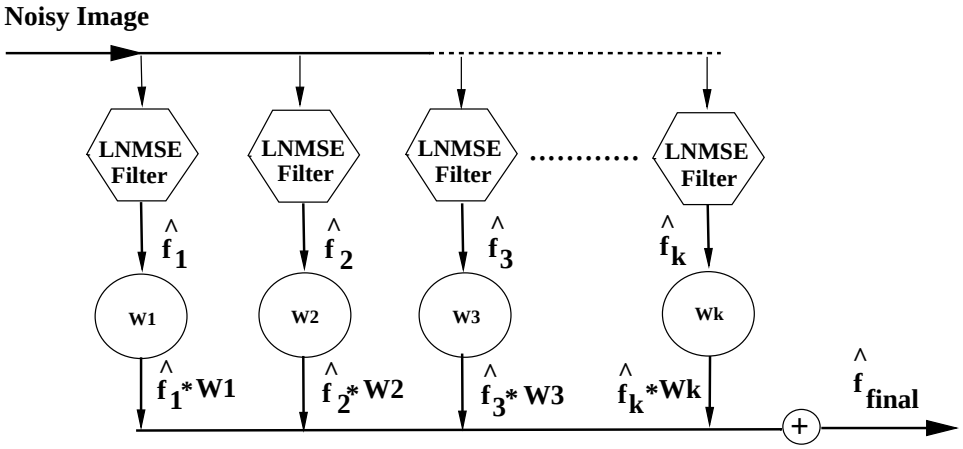

Figure 3.10: Our general filtering scheme in image space. Corresponding to any portion of the noise model an adaptive smoothing filter is designed and applied to the entire noisy image. The final output image is a weighted average of the individual outputs.

3.5.6 Performance criteria

The performance of a restoration filter highly depends on human visual perception criteria [4]. It also depends on the validity of noise model. Due to the complexity of the human

vision system, several criteria are needed to asses the performance of the filter [21]. In our work, we use both quantitative and qualitative criteria. MSE or SNR are examples of the first category which correspond to the noise attenuation measures. These measures are formulated as

$$MSE = \frac{1}{NM}\sum_{m}\left(f(m)-\hat{f}(m)\right)^2, \tag{3.12}$$

$$SNR = 20\log_{10}\frac{\sum_m f^2(m)}{\sum_m\left(f(m)-\hat{f}(m)\right)^2} \tag{3.13}$$

where $\hat{f}$ is the estimate of the noise-free image f, and NM is the size of the image. Furthermore, as human perception highly depends on edge information [22], its preservation is important. This motivates using edge preservation as a qualitative criterion. Edge preservation is assessed visually.

Chapter 4

Results and discussion

4.1 Introduction

We have performed experiments on a series of images corrupted by simulated noise based on the typical photon transfer curve. In this section we present results and discuss the performance of our denoising schemes in both image space and light space, followed by a performance comparison between the two methods. We first begin with the experimental results associated with the photon transfer curve.

4.2 Experimental results

The uncertainty measurement of CCD sensors are obtained by generating the photon transfer curve. The photon transfer curve (PHTC) is obtained by acquiring images through the procedure explained in Section 3.2.1. The first step is to calculate the dark offset image. Dark image results are presented in the following section. A real image whose histogram approximately covers the entire image dynamic range is selected. A Kodak DCS260 camera, with a known camera response function, was used for the experiments. We collected 700 frames of a real scene with the exposure time of $\frac{1}{2.5}$s. Exposure time could be set to a different value provided that the recorded image exhibits

Table 4.1: Intensity statistics for dark images in image space, where σ represents the standard-deviation.

Intensity	Mean	σ in image space	σ in light space
0	0.16	0.41	0.00006
1	0.694	0.753	0.0001
2	1.7	1.1	0.00015
3	2.827	1.573	0.00026
4	3.9766	1.891	0. 00039

most of the dynamic range, *i.e.* $[0, 255]$. The offset image was subtracted from all 700 images in light space.

4.2.1 Dark images

The variations due to dark noise are estimated by calculating a robust standard deviation in the temporal direction for intensities in the range of $[0, 4]$ in both light and image space. We only consider intensities in this range, because there is not sufficient data for higher intensities in the dark image set. As shown in Table 4.1, dark noise appears to be slightly signal-dependent in light space. This may be due to the nature of dark current noise which follows Poisson statistics. Figure 4.1 shows the histogram of data corresponding to the intensity 3 in image space and light space.

To remove the dark offset we captured 600 images under no-light condition. These images were then averaged together to generate the dark offset image. Figure 4.2 shows a one dimensional representation of the offset image captured with KodakDCS260. As shown, most pixels in this image have values below 4.

Faulty pixels were identified as the outliers of the distribution corresponding to the offset image. Outliers were considered as the pixels whose intensities fall beyond the confidence interval $[\mu - 3\sigma, \mu + 3\sigma]$), where μ and σ are the average and standard deviation of the offset image respectively. Statistics of the dark offset image are provided in Table 4.2. Dark offset image is transformed into light space. This image is subtracted

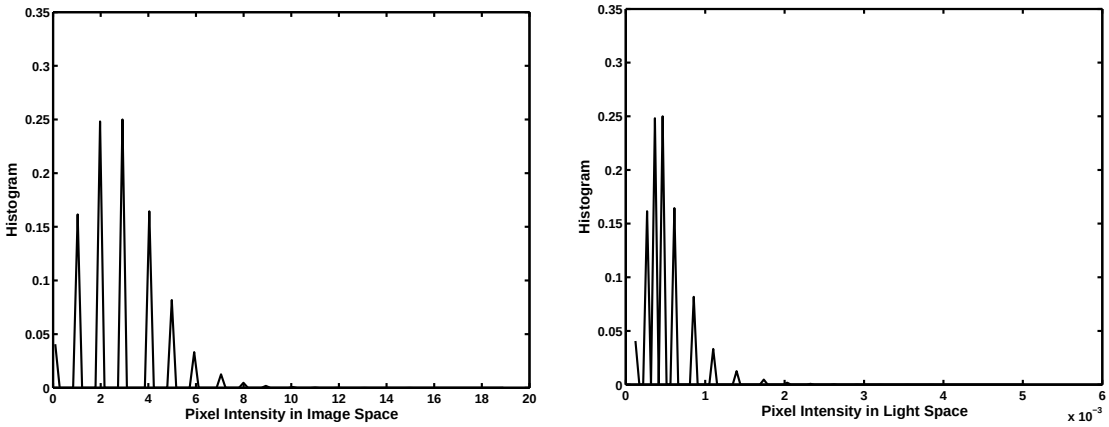

(a) (b)

Figure 4.1: Histogram of the non-dark-image data set corresponding to intensity of 3 (a) in image space and (b) in light space.

from the 700 non-dark images in light space.

Table 4.2: Dark offset statistics.

Mean	0.96
Standard Deviation	0.24
Range	[0 44]

4.2.2 Noise model

The resultant PHTC corresponding to the Kodak DCS260 digital camera is shown in Figure 4.3. The characteristic noise can be divided into three regions corresponding to the signal level. Since the PHTC is a logarithmic plot of signal against its noise standard-deviation, these regions exhibit slopes that can be associated with the nature of dominant noise. For instance the low signal region, $[0, 53]$, has approximately the slope of zero. This is consistent with the typical CCD noise characteristics in the low signal levels, as noise is mostly dominated by the CCD readout noise. The readout noise is independent of signal level. For the intermediate range, $[54, 168]$, the observed non-zero slope is 0.6 and is attributed to shot noise, which has a Poisson distribution. The maximum slope

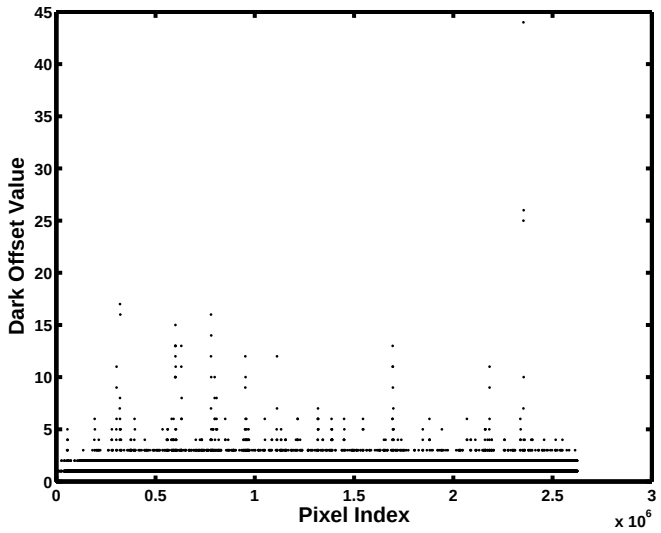

Figure 4.2: One-dimnesional offset image

is located in the high intensity region, which is dominated by fixed pattern noise. The observed value for the slope was 1.05.

Corresponding to each noise region we fit a straight line. The slope and offset of these straight lines determine the noise parameters γ and σ_u in each noise region. Noise parameters σ_u, γ, and σ_c are determined using the PHTC. For instance, on the logarithmic scale, the intercept of the simulated PHTC is σ_u and γ is the slope in the second region.

4.3 Simulation results

4.3.1 Comparison of noise characteristics in light space and image space

Due to the nonlinearity of the camera response function (CRF), noise characteristics are different in image space than they are in light space. The noise curve in image space represents the logarithmic plot of image intensity against its noise variance. As a simple case let us begin with a Gaussian noise in in light space and examine the effect of nonlinearity on the corresponding noise curve in image space. Figure 4.4 illustrates that

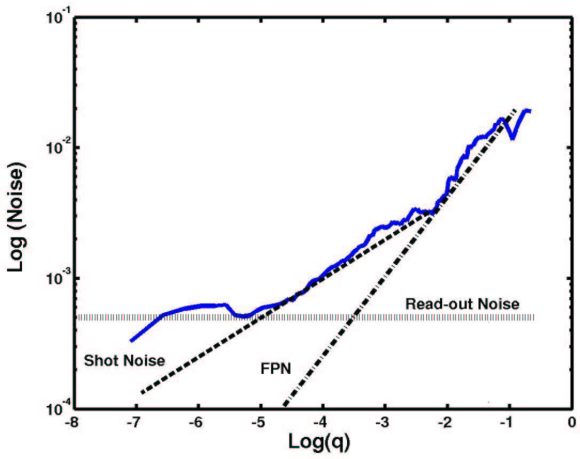

Figure 4.3: Photon transfer curve (Kodak DCS260). Dotted lines denote the linear approximation to the different regions of the curve. The q values are normalized to the range $[0, 1]$.

an independent one-region noise curve in light space is transformed to a noise curve with three regions, in which all the regions exhibit signal-dependent characteristics.

As outlined earlier, the derivative of the CRF exerts the main influence on noise characteristics in image space. This is because

$$\begin{aligned} \mathcal{F}(q + n_q) &\approx \mathcal{F}(q) + \dot{\mathcal{F}}(q) n_q, \\ \Longrightarrow n_I &\approx \dot{\mathcal{F}}(q) n_q \end{aligned} \tag{4.1}$$

where q is the light space value, n_q is noise in light space, $\mathcal{F}$ is the CRF, and n_I is noise in image space. As shown in Figure 4.4, for intensities in the range of ($[0, 100]$), γ is close to zero. The negative slope in the second noise region (image space) is due to the reduction in $\dot{\mathcal{F}}$ for higher intensities. When $\mathcal{F}$ reaches the saturation area, its derivative approaches zero, leading to a sharp decrease in noise variance in image space.

If the CRF is linear, regardless of light space intensity, the noise model in both domains will have the same features. Figure 4.5 shows two images with the assumption of linear CRF (a), and nonlinear response function (b). The noise is Gaussian in light

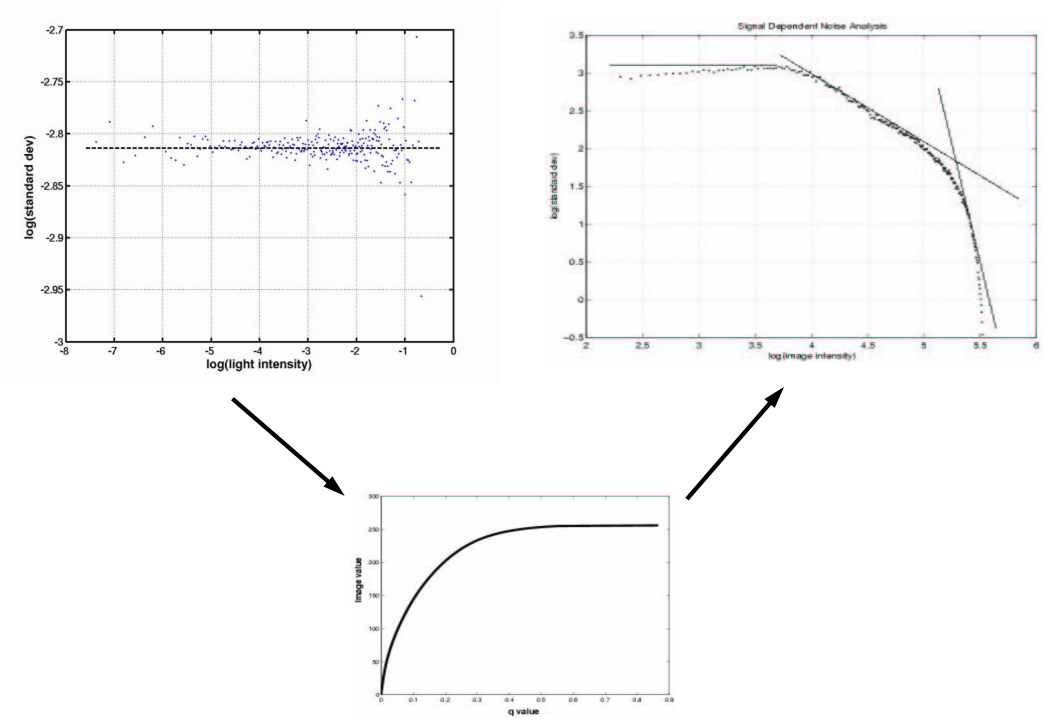

Figure 4.4: Constant noise in light space (left) converts to signal-dependent noise in image space due to the nonlinear CRF. The noise curve in image space has three distinct regions shown by straight lines.

space for both images. The effect of nonlinearity is more apparent in light regions of the image as shown in Figures 4.5 and 4.6.

(a) (b)

Figure 4.5: (a) Gaussian noise in light space is transformed to Gaussian noise in image space, if the CRF is linear. The second image (b) is the resultant noisy image corresponding to a nonlinear CRF. Light regions in (b) are less affected by noise due to the nonlinearity.

Now let us assume that noise in light space is signal-dependent for all intensities. We now wish to observe the effect of signal dependent noise in the transformed noise curve in image space. In light space we assume an exponential noise model such that

$$\begin{aligned} q_n &= q + n_q, \\ n_q &= q^\gamma \mathcal{N}(0, \sigma_u) \end{aligned} \tag{4.2}$$

The resultant noise in image space can then be written as

$$\begin{aligned} \mathcal{F}(q_n) &= \mathcal{F}(q + n_q) \\ &\approx \mathcal{F}(q) + \dot{\mathcal{F}}(q) n_q \\ &\approx \mathcal{F}(q) + \dot{\mathcal{F}}(q) q^\gamma \mathcal{N}(0, \sigma_u) \end{aligned} \tag{4.3}$$

Figure 4.7 shows how a one-region noise curve in light space converts to a three-region

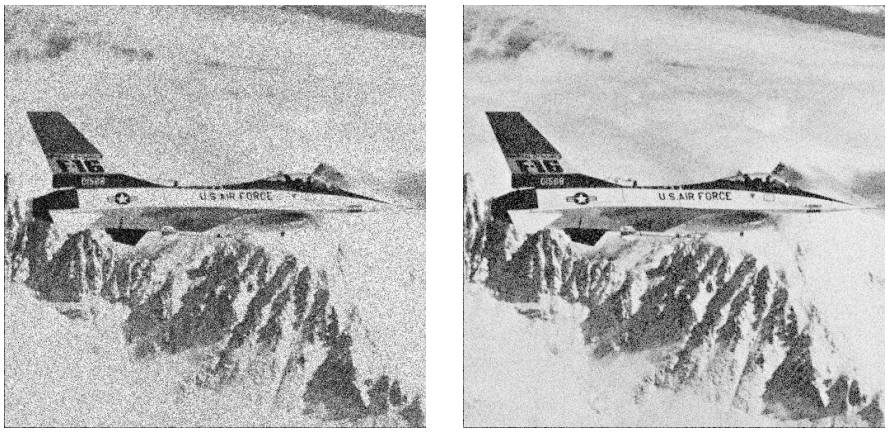

(a) (b)

Figure 4.6: (a) A noisy image corresponding to a linear CRF, (b) the noisy image as result of nonlinear CRF. The effect of nonlinearity is more apparent when an image includes many high-intensity regions.

noise curve in image space. For low intensities (in the range of $[0, 54]$), noise has similar characteristics in both domains. In other words parameter γ remains the same in image space. The negative slopes in the other noise regions are on account of $\dot{\mathcal{F}}$ decreasing as q increases.

We now simulate a noise model similar to the typical photon transfer curve. Let σ_c denote the noise standard-deviation in the first region of the PHTC. The total noise standard deviation σ_n associated with a typical CCD sensor can be formulated as

$$\sigma_n = \begin{cases} \sigma_c & f \leq e^B \\ \sigma_u \cdot f^\gamma & f > e^B \end{cases} \tag{4.4}$$

where e^B is the breakpoint between the two regions. When the image intensity is less than a certain value e^B, noise can be modeled as constant.

The simulated noise model in light space is shown in Figure 4.8. The breakpoint is located at the intensity of 24. We select this location based on the Kodak DCS250 photon transfer curve.

Depending on the noise parameters γ, σ_u, σ_c, and the location of the border between

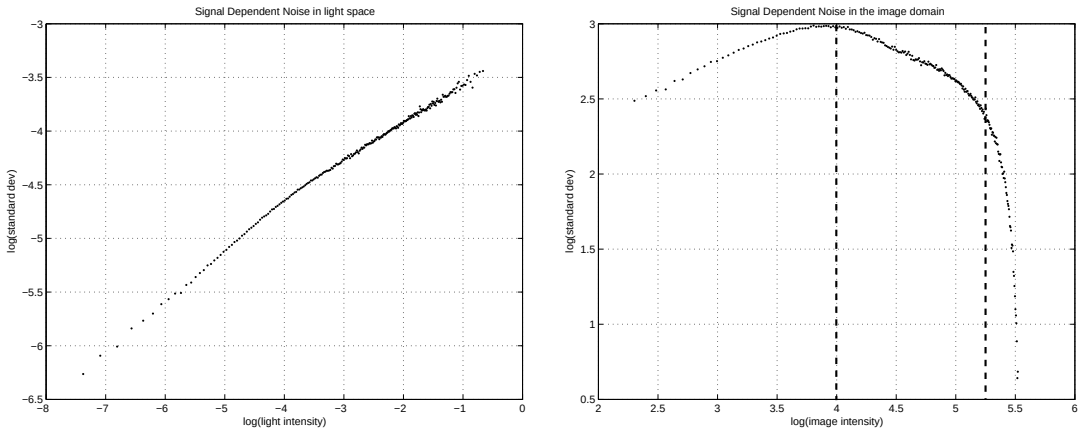

(a) (b)

Figure 4.7: (a) Exponential noise curve in light space with noise parameter $\gamma = 0.35$. (b) The resultant noise curve in image space. Dotted vertical lines partition different noise regions. The slope (exponent) of noise curves in each region varies as a function of $\dot{\mathcal{F}}$.

the two noise regions in light space, various noise models result in image space. In what follows, we fix each noise parameter and examine the effect of the other parameters on noise features in image space. We first set γ equal to 0.4 and vary σ_u. The resultant noise curves in image space are shown in Figure 4.9.

It seems that the discontinuity of the noise curve in light space is more evident when dealing with larger σ_u. Noise curve in image space appears to have three or four distinct regions with different lengths depending on the σ_u value. For low σ_u values, noise in image space can be approximately divided into three regions. The noise curve in image space tends to have four regions as σ_u increases.

It is also interesting to investigate the effect of exponent γ on the noise curves in image space. As shown in Figure 4.10, increasing γ results in less noise in image space but steeper slopes for the first region.

Overall, the location of the breakpoint in light space, the type of CRF and the amount of noise added in the light space, can influence the slope, length and the number of regions of the noise curve in image space.

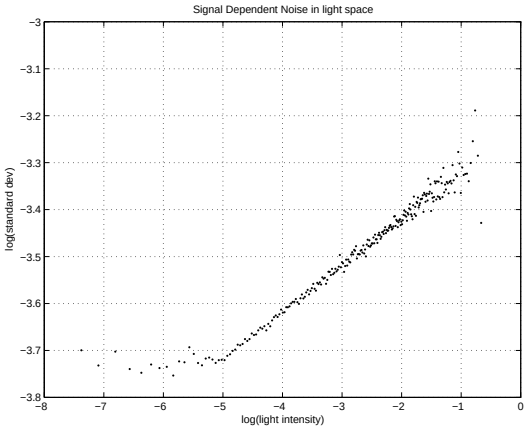

Figure 4.8: PHTC for a simulated two-region noise model in light space

4.3.2 Filtering algorithm

The performance of our restoration methods is assessed by using images, degraded by synthetic noise according to the model presented in Figure 4.8. Based on our general denoising scheme, we do two sets of experiments on the test images. The first set of experiments deals with filtering of noise in light space, while the second set attempts to restore the degraded images in image space.

Denoising in light space

Our restoration approach in light space is based on the light space denoising diagram shown in Figure 3.3 in Section 3.3. An image is initially converted to light space. The transformed image is then degraded by noise, whose model is shown in Figure 4.8. The degraded image is processed by a combination of adaptive noise smoothing (ANS) filters. Signal-independent noise is addressed by an adaptive Wiener filter.

In the signal-dependent region of the PHTC we apply 3×3 and 9×9 ANS filters. We use various window sizes to examine the effect of filters on uniform areas and their effect on high-frequency areas. Figure 4.11 illustrates that the ANS filter with the larger window size, even though it performs better in uniform areas, distorts the edges. The

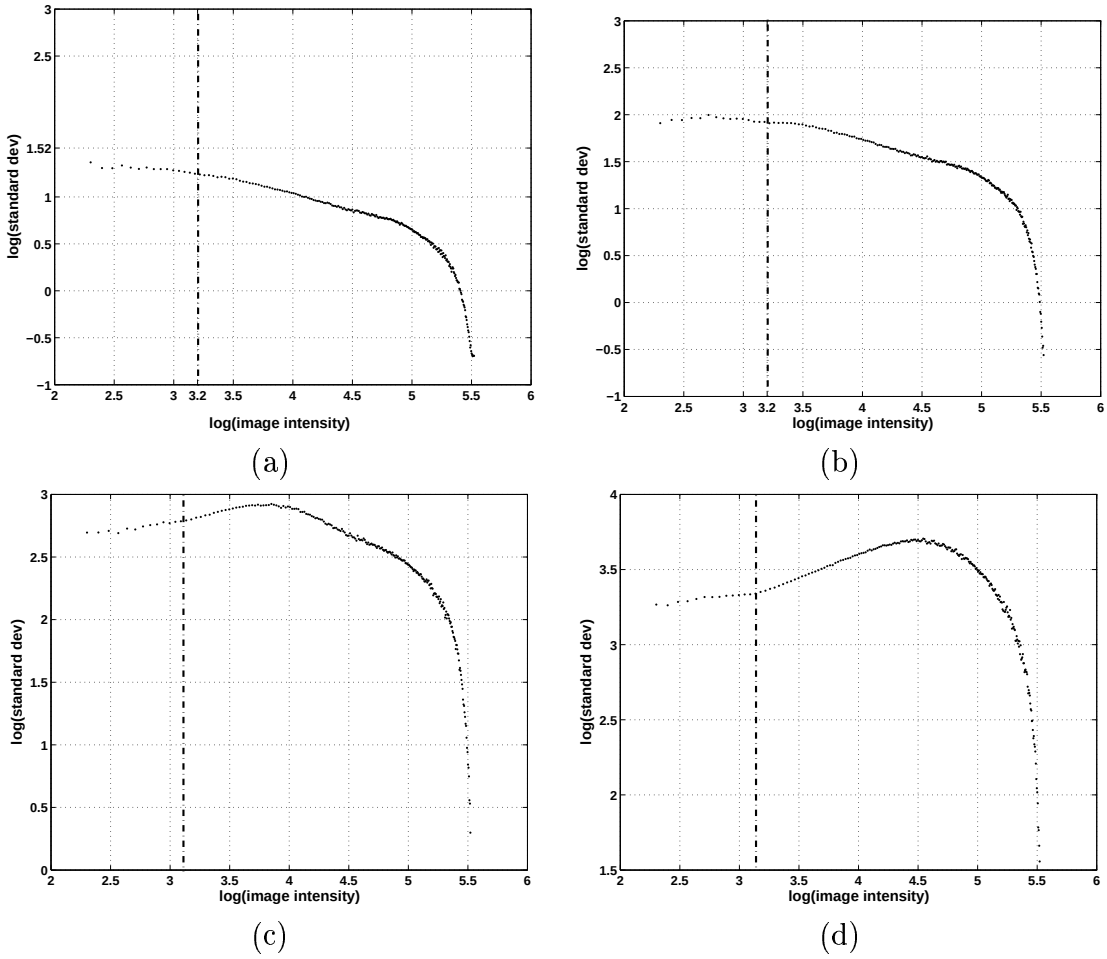

Figure 4.9: Noise curves in image space with parameter γ fixed and σ_u varying. Parameter σ_u is 0.005 in (a), 0.01 in (b), 0.03 in (c), and 0.08 in (d).

bigger the window size, the wider the distortion area. This is due to the inaccurate local estimate of noisy-image statistics in the areas around edges. To reduce this side effect, we use the robust technique to estimate the local mean values in the noisy image. Local mean values are computed as the trim mean estimates. To improve the results and use a correct neighborhood, we also design an edge map, which combines the results of the two ANS filters. The edge detector is based on the ratio of noise-free signal variance to that of the noisy signal. For every local region in the image the ratio of $\frac{\sigma_f^2}{\sigma_g^2}$ is estimated,

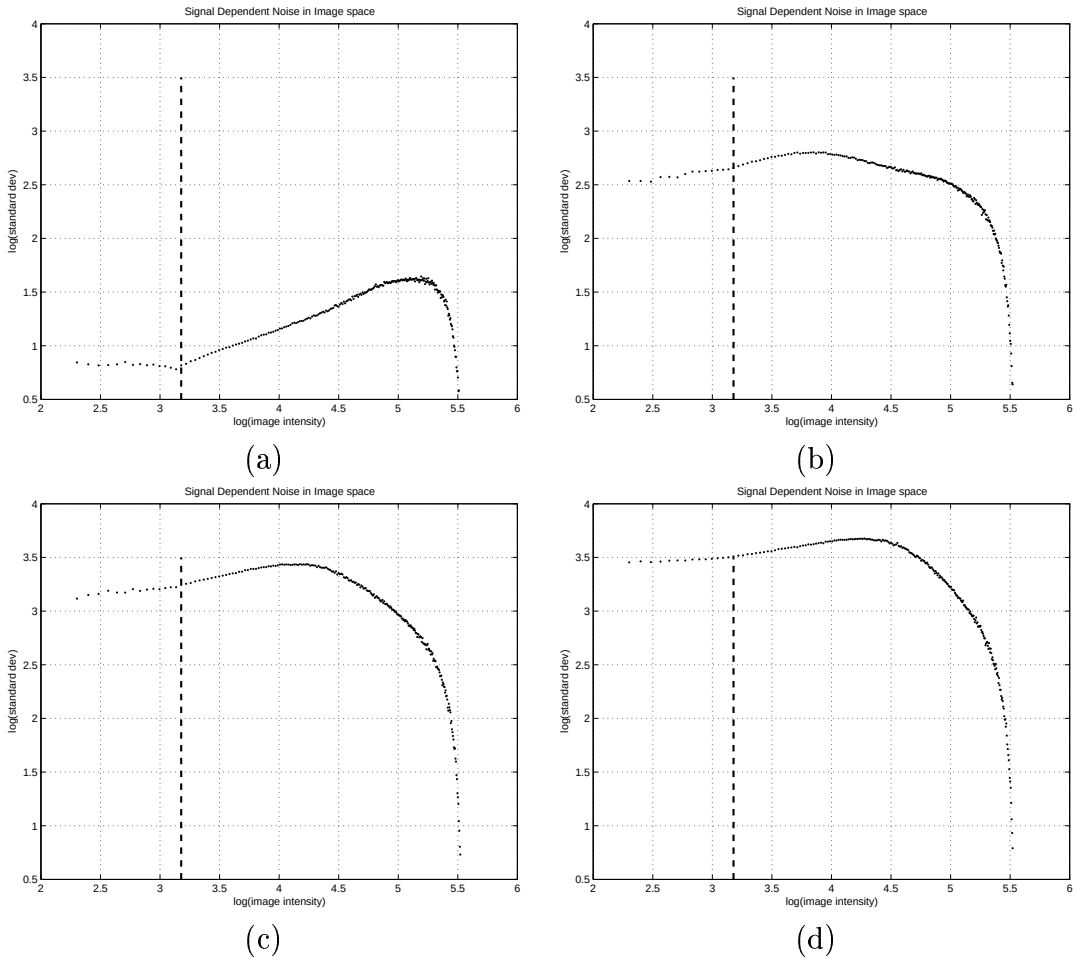

Figure 4.10: Noise curves in image space with parameter γ varying and σ_u fixed. Parameter γ is 0.6 in (a), 0.4 in (b), 0.3 in (c), and 0.2 in (d). The vertical dotted lines show the breakpoint between the two noise regions in light.

such that

$$\sigma_f^2 = \frac{\sigma_g^2 - \sigma_u^2 \mu_f^{2\gamma}}{1 + \gamma(2\gamma - 1)\mu_f^{2\gamma-2}\sigma_u^2} \tag{4.5}$$

where γ and σ_u are signal-dependent noise parameters. Since σ_f^2 is an estimate of the true value, artifacts are also created in non-edge areas. The smaller the local neighborhood the more artifacts. The data associated with the ratio values for every pixel is then screened by applying a threshold. In doing so, we reject any area as an edge whose ratio is smaller than this value. We find the optimal threshold value by examining the

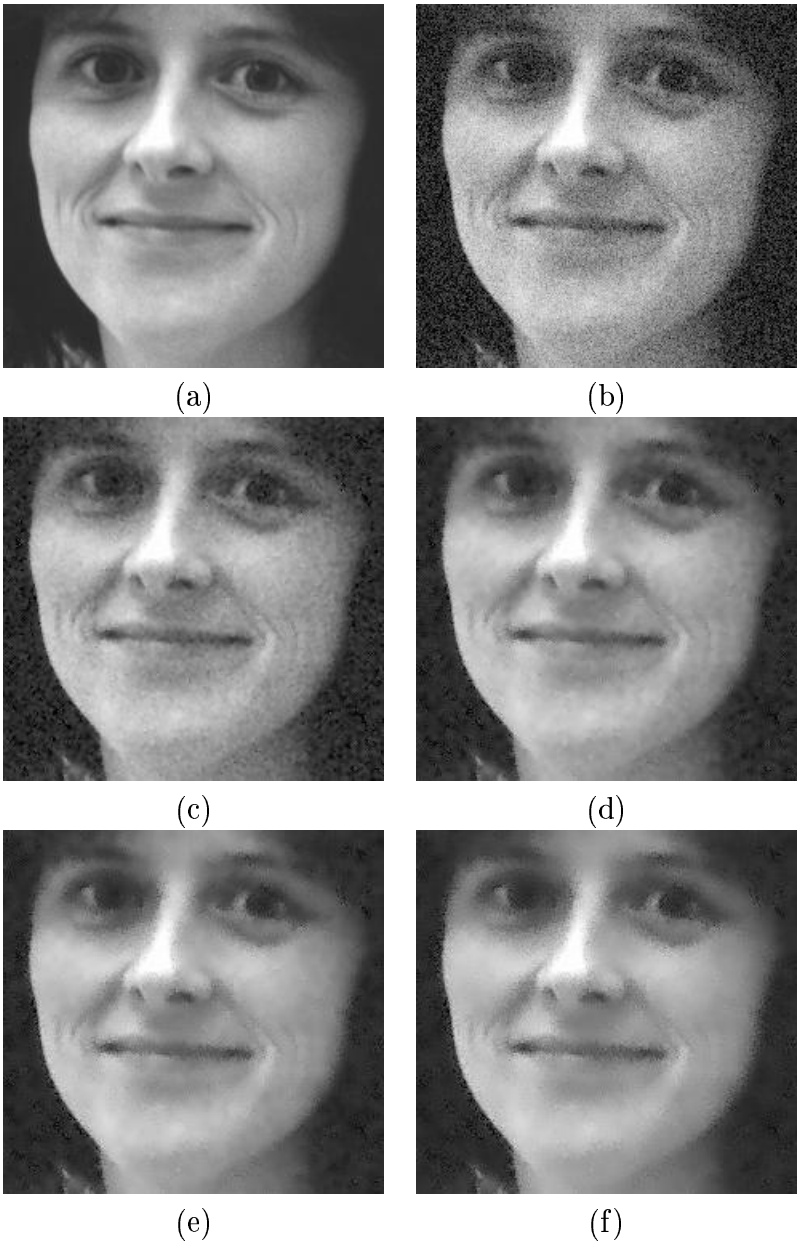

Figure 4.11: Effect of the ANS filter window size on the outputs. Filters with larger window sizes tend to perform better in uniform areas at the expense of creating more artifacts. (a) Original image, (b) Image degraded with noise with $\gamma = 0.3$ and $\sigma_u = 0.03$, (c) a 3×3 ANS filter,(d) a 5×5 ANS filter, (e) a 7×7 ANS filter, and (f) a 9×9 ANS filter.

histogram of the raw edge map. Depending on the noise parameters we select different thresholds. Through the sensitivity analysis process explained in Section 3.6, an optimal range for the threshold is found. In this process we degrade various images equally (the same noise parameters), estimate the edge map, and finally find the best threshold value for each image. We determine the final threshold by averaging over all measured thresholds. We use the average threshold on a variety of images to evaluate the effect of possibly inaccurate threshold values on the edge maps. For the same noise parameters, different images seem to yield very similar threshold values. Experimental results show that threshold values appear to be only dependent on the noise parameters rather than the type of image. For instance if γ and σ_u are 0.3 and 0.04 respectively, the threshold value of 0.65 works well for a variety of test images. Figure 4.12 shows the edge maps corresponding to these noise parameters and the selected threshold. We use a window size of 7×7, which gives a reasonable size for a variety of test images.

After the optimal edge maps are created, they are dilated to make a smooth transition between the two ANS filters. The LNMSE filter is

$$\hat{f}_{LNMMSE}(m) = EG(m)\hat{f}_S(m) + (1 - EG(m))\hat{f}_L(m) \tag{4.6}$$

where m is the image location, EG is the edge map in the range of $[0, 1]$, and $\hat{f}_{LNMMSE}$ is the LNMMSE estimate. As an example, an LNMSE output image is shown in Figure 4.13 for "Lena" image. As shown in this figure, the performance of the 3×3 ANS filter in uniform regions is poor, but the edges are preserved. The 9×9 ANS filter significantly smoothes the uniform areas, but generates artifacts in edge regions. Combining the two ANS filters deals with the artifact problem.

Median filters are known to preserve edges. If instead of a 3×3 ANS filter we apply a 3×3 median filter, fine details are more blurred but it generates slightly less artifacts in the vicinity of edges. This may be because median filters do not depend on the inaccurate

estimate of σ_g^2. Figure 4.14 shows a cropped original image along with the corresponding noisy and filtered images. Comparing Figure 4.14 (c)-(d), we can see that the results of the adaptive smoothing filter is closer to the original image. The LNMSE preserves edges and smoothes the noise in the same ways as an average filtering. We can see that median filter performs poorly as expected in the presence of short-tailed noise, thus making a lower-contrast output image.

Finally, the LNMSE is then smoothly combined with the results of adaptive Wiener filter through a intensity map whose graph is shown in shown in Figure 3.7 in Section 3.5.4. Figure 4.15 shows how the weight function combines the results of the LNMSE, and adaptive Wiener filters. As shown, the adaptive Wiener filter blurs the image, while the LNMSE filter performs poorly in dark regions. These problems are removed by applying this map on both output images and combining the results.

Denoising in image space

At this stage we will describe the restoration of noisy images in image space. In our experiments, synthetic noise is added to images in light space and the noisy images are transformed back to image space. In contrast to denoising in light space, where the noise parameters are known *a priori*, the parameters for each noise region in the noise curve in image space need to be estimated. After obtaining the noise curve in image space and finding the borders between the noise regions, we approximate each region by a straight line. The slope and the offset corresponding to each line represent γ and σ_u for that specific noise region. Since the last region in the noise curve results in a very large intercept, it is not possible to apply ANS filter due to the numerical round-off problems when σ_u is significantly large.

We use an adaptive Wiener filter for the last noise region. For example, let us consider an image degraded with noise in light space ($\gamma = 0.4$ and $\sigma_u = 0.06$). The corresponding noise curve in image space consists of three regions as shown in Figure 4.16. The first

noise region includes intensities in the range of $[0, e^4]$ and the second region begins at the intensity of e^4, ends at the intensity of $e^{5.2}$.

For the same noise parameters in light space, noise curves in image space have almost the same shape. This enables using a general three-region noise model for every image degraded with noise whose model is fixed in light space. Figure 4.17 shows some examples of noise curves as a result of setting light space noise parameters γ and σ_u to 0.3 and 0.04 respectively. As shown in Figure 4.17, we consider three distinct noise regions. For image intensities in the range of $[0, e^4]$, γ ranges from 0.06 to 0.1 for different images. The slope in the second region, which covers intensities in the range of $[e^4, e^{5.2}]$, is approximately -0.5. These two noise regions are handled with LNMSE filters. We apply an adaptive Wiener filter to deal with noise associated with the last region of the noise curve. Figure 4.18 show the individual effect of each of these filters on one region of our test image "Gauge".

Similar to light space, 3×3 and 9×9 ANS filters are applied to the image. We also use local robust estimate for ANS filter parameters. Figure 4.19 illustrates the effect of the rejection percentage of the local trim mean when it is set to 0, 10, and 20 in Figure 4.19(b), (c), and (d) respectively.

An edge map then combines the results. The thresholds are selected by the same procedure used in light space. For example the threshold is selected as 0.56 if γ in light space is 0.3 and is set to 0.65 if γ is 0.6. We combine the three individual outputs, shown in Figure 4.18, with three weight functions as shown in Figure 3.8 in Section 3.5.4.

The final restored image is then the smooth weighted average of three output images such that

$$\hat{f}_{Final}(m) = \sum_{k=1}^{3} W_K(m) \hat{f}_k(m) \tag{4.7}$$

where m is the image location, and W_k and $\hat{f}_k$ are the weight function and the filtered

image corresponding to the kth noise region, and finally $\hat{f}_{Final}$ is final output. In Figure 4.20, the final estimates in both light space and image space along with the noisy image are given.

Various images are processed using both denoising schemes and the results associated with three images, whose edge maps are provided in Figure 4.12, are shown in Figure 4.21. We also show final results for images, which are degraded by less noise. In this set of experiments γ and σ_u are set to 0.6 and 0.06 in light space. Figure 4.22 shows the noise curves of some images associated with these noise parameters. The noise regions are partitioned at intensities $e^{3.2}$ and e^5.

Similar to the case where γ was 0.3, the noise curve is divided into three noise regions. The slope in the first region is in the range of $[0.07, 0.1]$, and 0.12 for the second region. Noise in the third region has a sharp decrease due to the saturation region in the camera response curve. As an example the final filtered image is shown in Figure 4.23-(a). The filtered image in light space is also given in Figure 4.23-(b) for comparison.

4.4 Quantitative performance criteria

Both qualitative and quantitative measures are utilized to judge the performance of our restoration algorithms. Uniform region smoothing and edge and fine detail preservation performance are assessed visually, therefore used as qualitative performance criteria. These qualitative assessments are included throughout this chapter. In order to evaluate the performance of our restoration methods mathematically, we compute Mean Square Error (MSE), Mean Absolute Error (MAE) and SNR as quantitative noise-attenuation measures. In light space, we compare the performance of our filter with the adaptive Wiener, and LNMSE filters. It shows how the combination of multiple filters applied on the same noisy image can improve the final results. Table 4.3 provides MSE values for various values of γ and compares the performance of adaptive Wiener, LNMSE, and the

final combined filters. As shown, noise level in the final combined image is significantly lower than the other filtered images.

Table 4.3: MSE measures of the "Peppers" image for three values of γ.

γ	Noisy	Wiener	LNMSE	Final combined
0.3	323.481	98.736	100.066	65.134
0.5	104.889	94.897	39.488	38.226
0.7	35.048	94.161	24.888	18.225

Table 4.3 also indicates that our final combined filter outperforms adaptive Wiener, LLMSE, and LNMSE filters by smoothing uniform regions and removing the artifacts around the edges, the blurriness effect of Wiener filter, and the artifacts in dark regions as a result of LNMSE filters effect.

We also compute these performance criteria in order to compare the performance of final filters in image space versus light space. Tables 4.4, 4.5, and 4.6 provide the comparison of performance of denoising in image space and light space for "Lena", "Peppers", and "Gauge" images.

Table 4.4: MSE, MAE and SNR measures associated with "Lena" image. Noise parameter γ is 0.3.

Image	MSE	MAE	SNR
Noisy	322.704	13.644	54.782
Filtered in light space	61.037	5.366	289.633
Filtered in image space	63.574	5.509	278.076

Experimental results with test images suggest that denoising in light space usually result in slightly higher quantitative performance (higher SNR, lower MSE and MAE) as shown in Tables 4.4 and 4.5. Since in image space, the last noise region is handled with an adaptive Wiener filter, the results in high-intensity regions are more blurred in comparison with the outputs filtered in light space as shown in Figure 4.24. Therefore it

Table 4.5: MSE, MAE and SNR measures associated with "Peppers" image. Noise parameter γ is 0.3.

Image	MSE	MAE	SNR
Noisy	331.363	13.895	52.065
Filtered in light space	68.715	5.775	251.072
Filtered in image space	68.875	5.909	250.492

Table 4.6: MSE, MAE and SNR measures associated with "Gauge" image. Noise parameter γ is 0.3.

Image	MSE	MAE	SNR
Noisy	406.128	16.695	22.967
Filtered in light space	40.849	4.290	228.350
Filtered in image space	39.712	4.441	234.886

is likely that decreasing contrast in bright regions contributes to a rise in the total error between the filtered image and th original image.

On the basis of the experiments performed, it appears that except for bright areas, restoration in image space and light space visually seem to result in outputs with almost equal quality in term of noise smoothing and edge preservation. This is also supported by quantitative measures. For bright areas however, light space denoising is superior to image space filtering as mentioned earlier.

In summary, despite the similar performance in both domains, denoising in light space is still preferable because

- The restoration scheme has a simpler structure due to a simpler noise model in light space,
- denoising in light space is computationally less demanding, due to the lower number of weight functions and filters developed in light space,
- for the same noise parameters a shift in the breakpoint partitioning the two noise regions in the PHTC, may considerably change the shape of image space noise

curve, which may require a more complex denoising scheme. As an example, Figure 4.25(a)-(b) shows the noise curves with breakpoints at e^{-5} and e^{-4} in light space. The corresponding image space noise curves are shown in Figure 4.25(c)-(d).

- and finally, light space denoising is superior when dealing with bright regions. As outlined earlier, the image space filter, addressing the noise associated with light regions, does not perform well. This, however needs further investigation in image space.

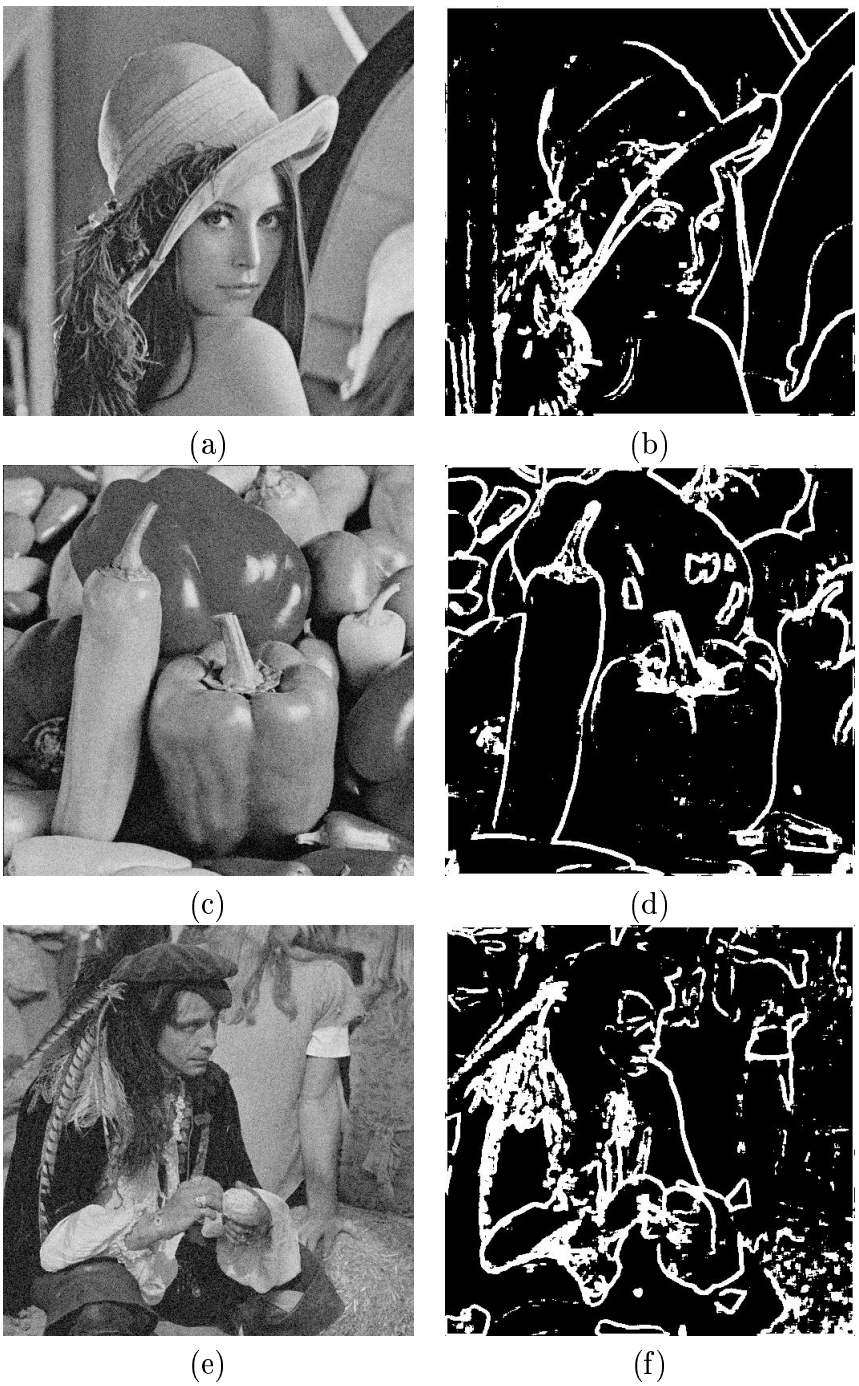

Figure 4.12: Edge maps estimated from the noisy images "Lena", "Peppers", and "Scene". Noise parameters γ and σ_u are 0.3 and 0.04 respectively. Edge map threshold is 0.65.

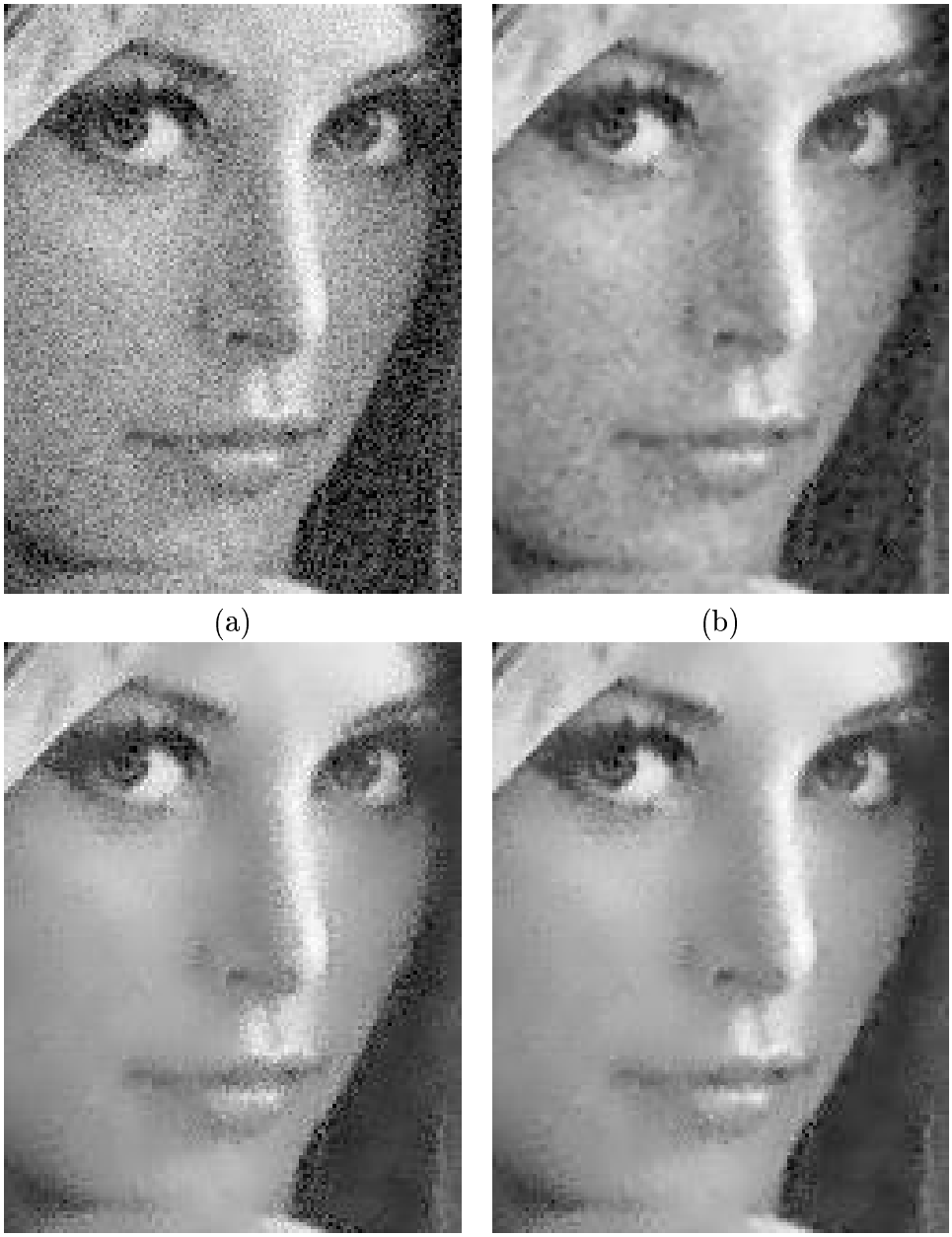

(a) (b)

(c) (d)

Figure 4.13: Effect of edge map on artifact reduction: (a) corrupted "Lena" image with $\gamma = 0.3$ and $\sigma_u = 0.05$, (b) filtered image with a 3×3 ANS filter,(c) a 9×9 ANS filtered image, and (d) the LNMSE result. The two resultant images are combined so that the filter with smaller window size is dominant in edge regions, but gradually reduces its influence in uniform regions where the second filter becomes dominant.

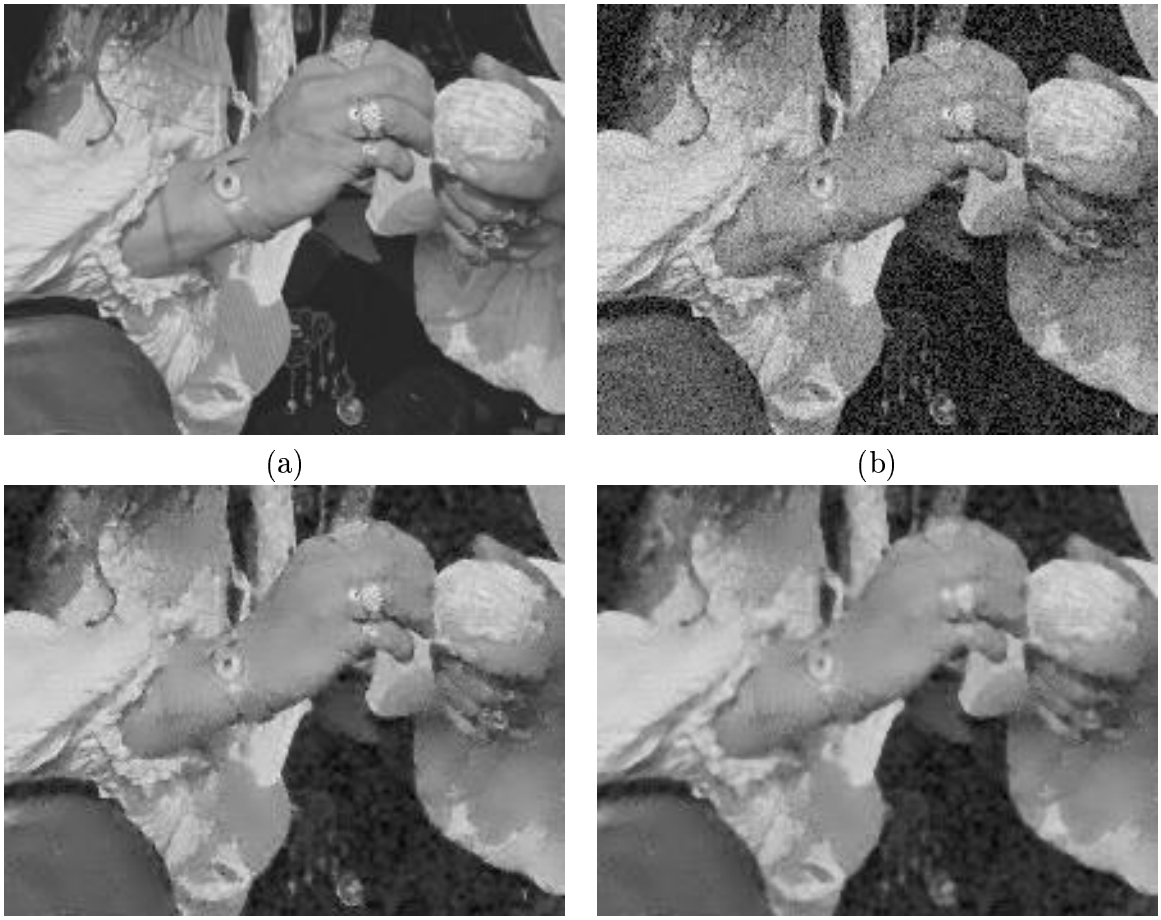

(a) (b)

(c) (d)

Figure 4.14: Effect of median filtering on the final combination results. (a) Cropped image, (b) the degraded image with $\gamma = 0.3$ and $\sigma_u = 0.04$, (c) final image as a result of combining two ANS filters, and (d) final image as a result of combining a 9×9 ANS filter and a median filter. Fine details, such as areas close to the ring and watch, have more contrast in comparison with median filtering.

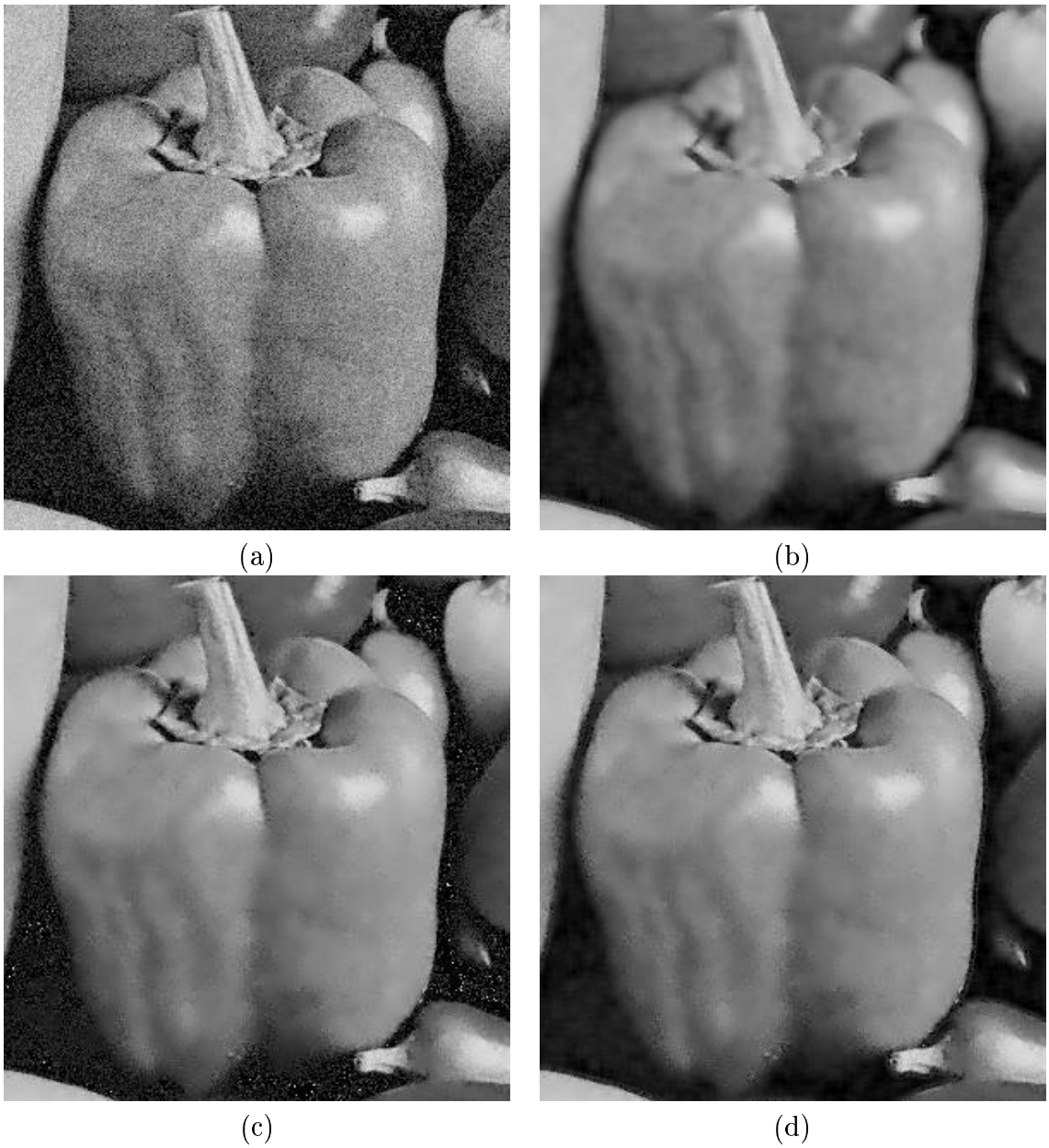

(a) (b)

(c) (d)

Figure 4.15: Effect of the weight function: (a) cropped "Peppers" image degraded by $\sigma_u = 0.04$ and $\gamma = 0.3$, (b) adaptive Wiener estimate, (c) LNMSE estimate, and (d) final combined denoised image, artifacts in dark regions are removed.

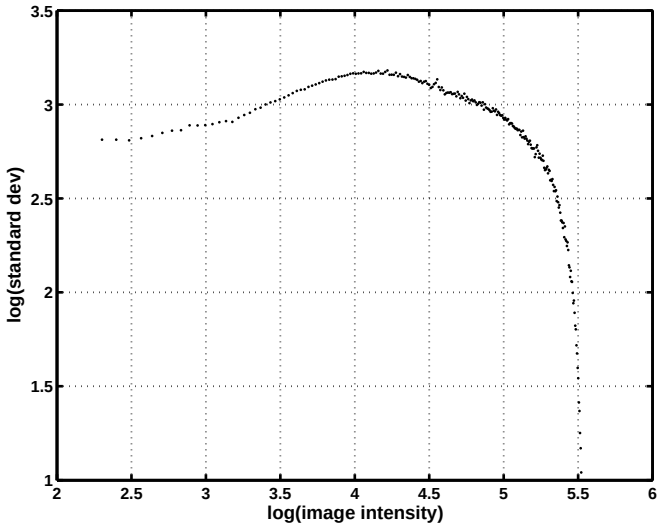

Figure 4.16: The noise curve in image space, where $\gamma = 0.4$ and $\sigma_u = 0.06$ in light space. Except for the last region, other regions are approximated by straight lines whose slopes and interprets are the noise parameters to be fed into the ANS filters.

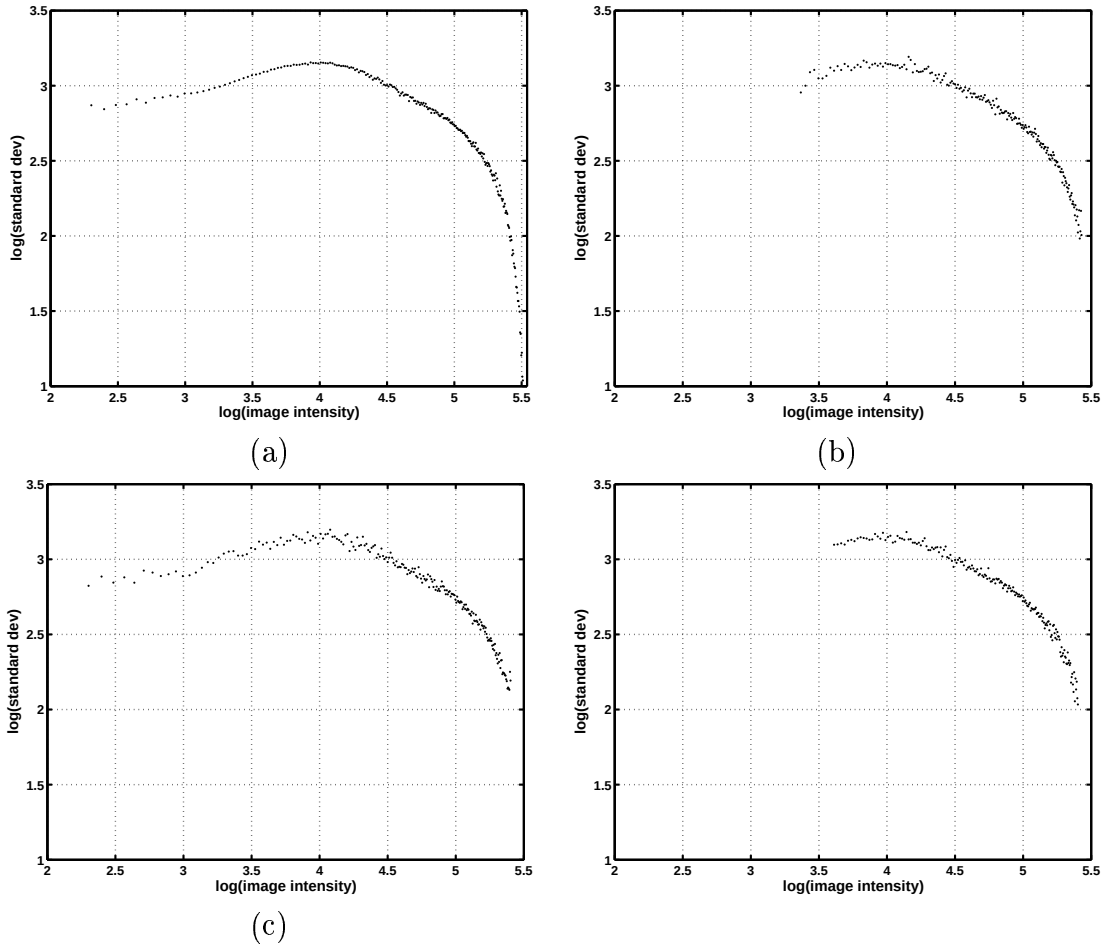

Figure 4.17: Noise curves corresponding to different images , when γ and σ_u are 0.3 and 0.04 respectively in light space.

(a)

(b)

(c)

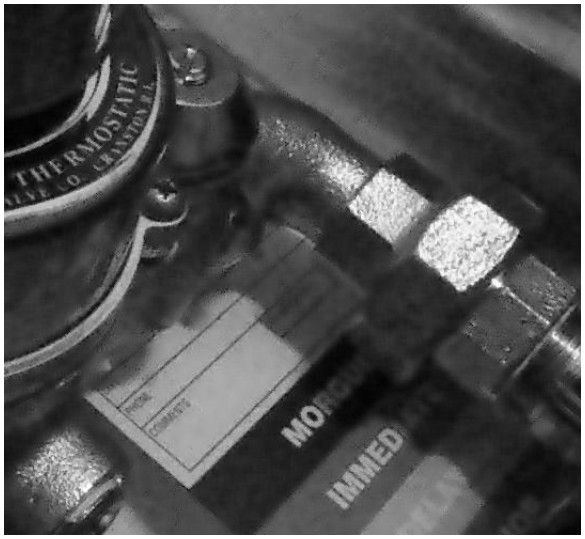

(d)

(d)

Figure 4.18: A degraded image is restored in image space using three separate adaptive filters, each of which addresses one region in the noise curve. Therefore they perform poorly outside the target noise region. The original and noisy images are shown in part (a) and (b) respectively. Dark areas are denoised in (c), middle range intensities are the targets in (d), and finally the adaptive Wiener filter removes noise from the bright areas of the image in (e).

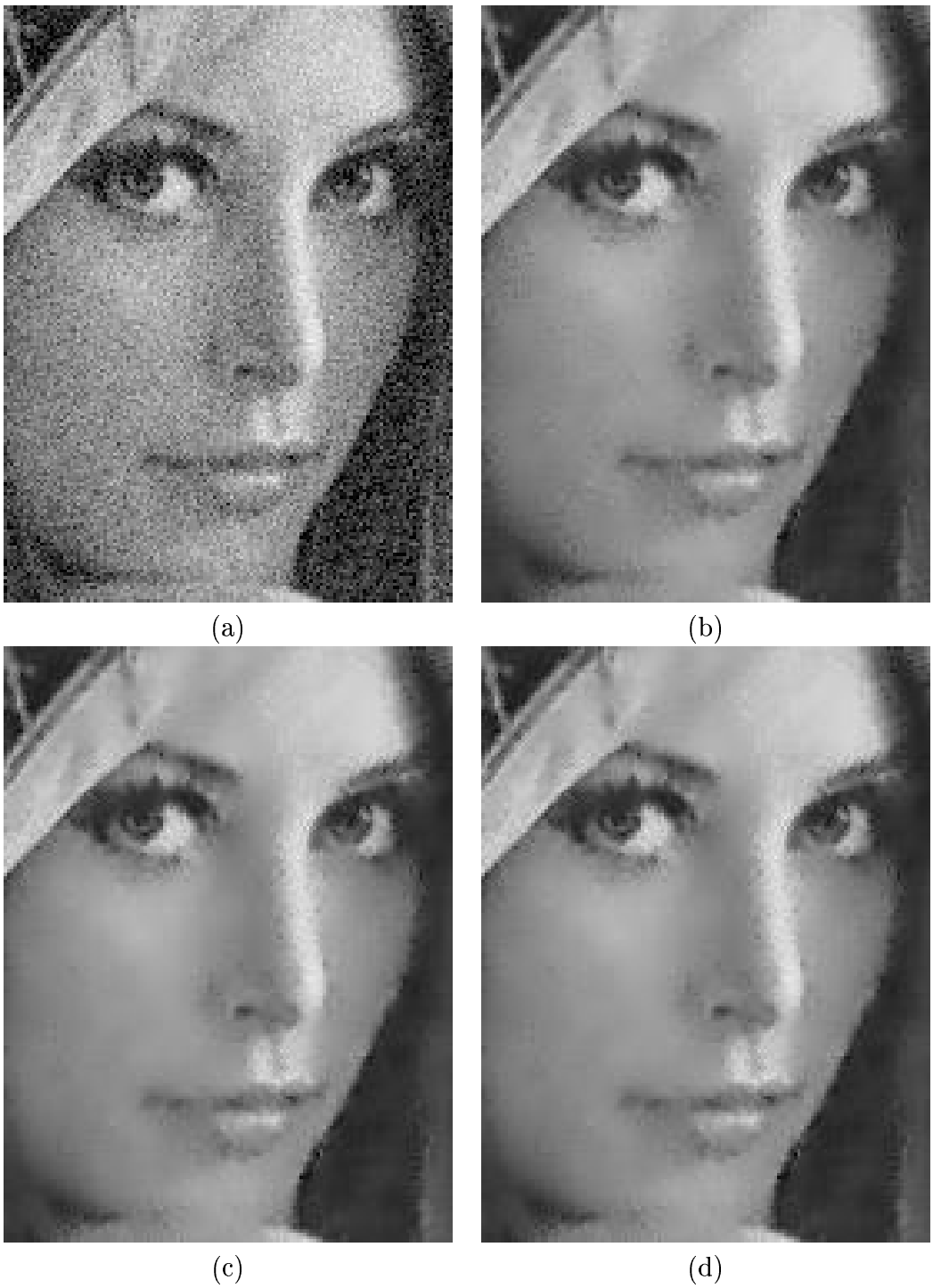

Figure 4.19: The ANS filter performs better if the local estimate of image statistics are more accurate. One way is to use local trim mean instead of simple averaging process. In doing so less artifacts are observed in the edge regions. (a) corrupted "Lena" image with $\gamma = 0.3$ and $\sigma_u = 0.04$, (b) Final filtered image using simple averaging for local mean estimates,(c) Filtered image as a result of using local trim mean with the rejection percentage of 10. (d) Filtered image when using local trim mean with the rejection percentage of 20.

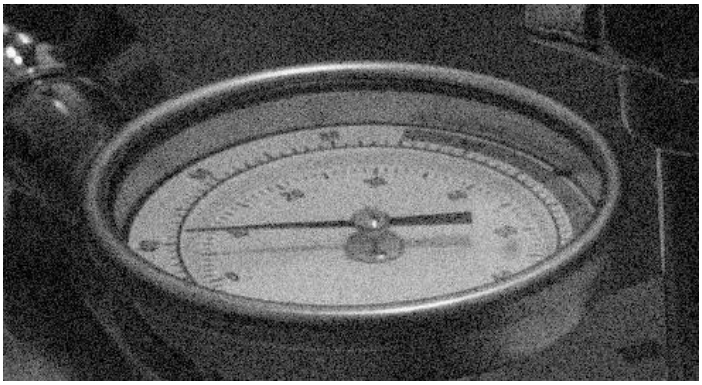

(a)

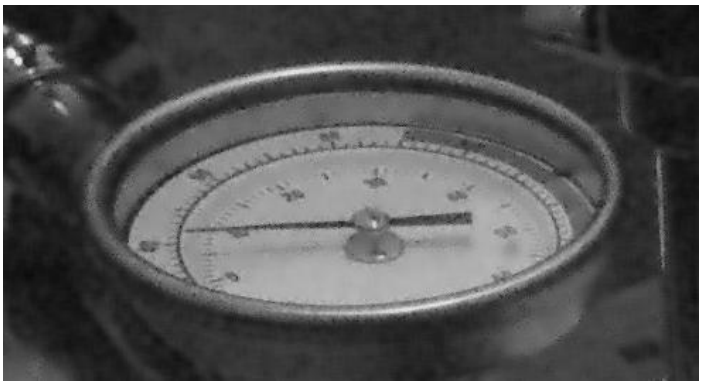

(b)

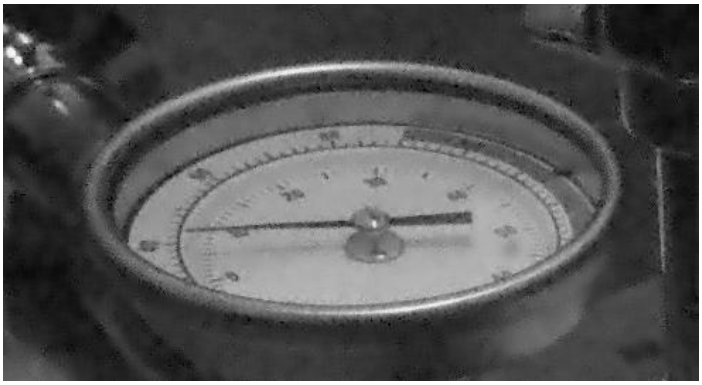

(c)

Figure 4.20: Apart from light regions, both denoising in image and light space have satisfactory performance in terms of smoothing the noise and preserving image boundaries. The noise-free image is degraded in light space with $\gamma = 0.3$ and $\sigma_u = 0.04$. The image shown in (b) is the restored image in image space, while (c) shows the restored image in light space.

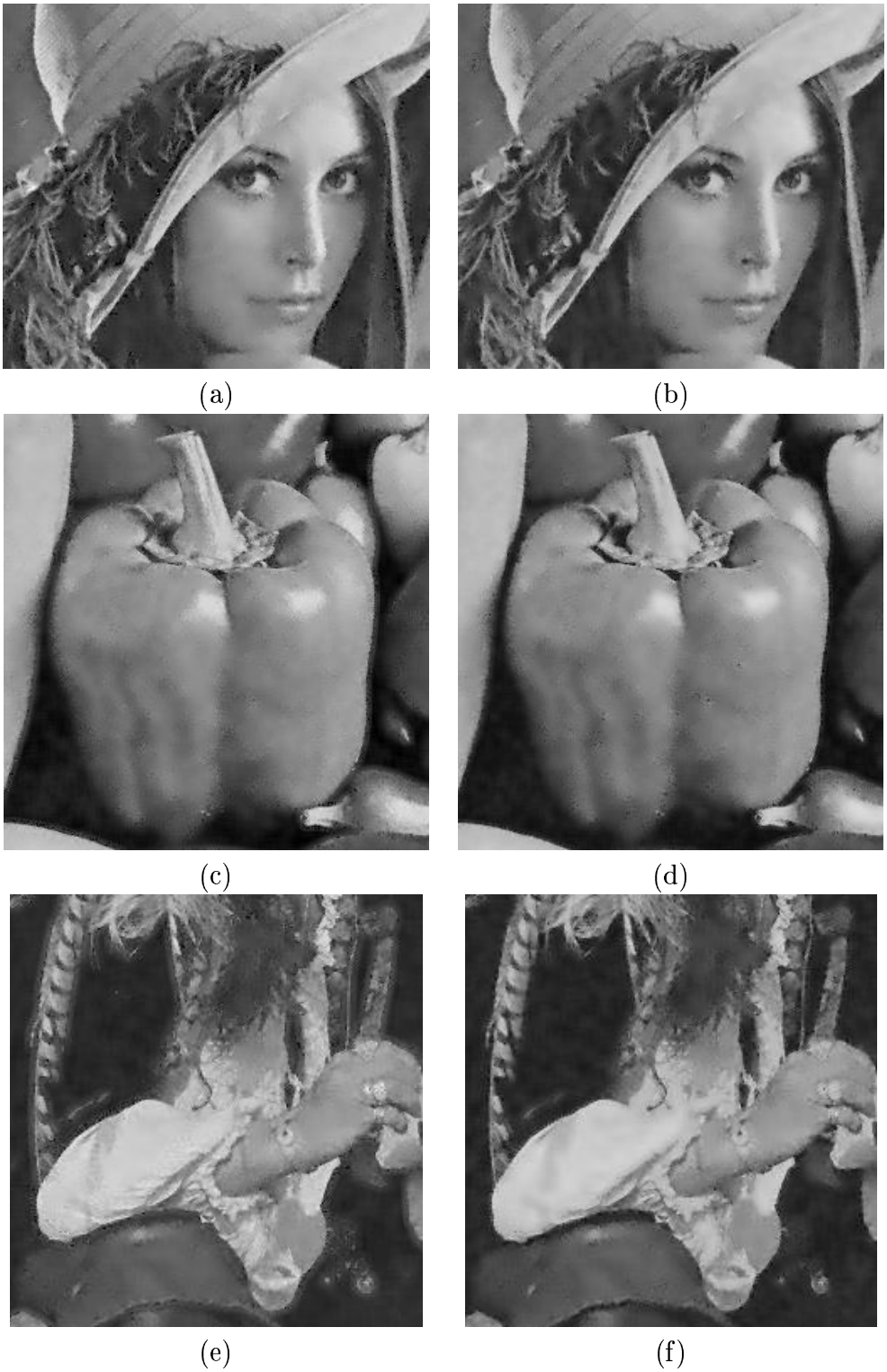

Figure 4.21: Final outputs of standard images "Lena", "Peppers", and "Scene" in light space are provided in (a), (c), and (e). image space results are shown in (b), (d), and (f). Light space noise parameters γ and σ_u are 0.3 and 0.04 respectively.

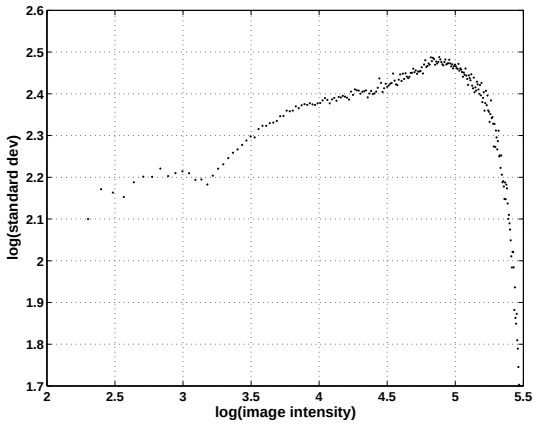

(a)

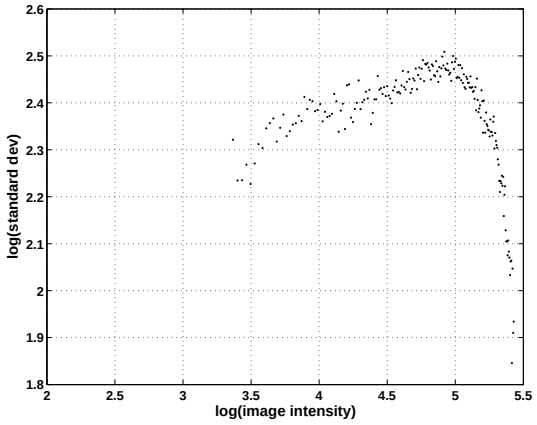

(b)

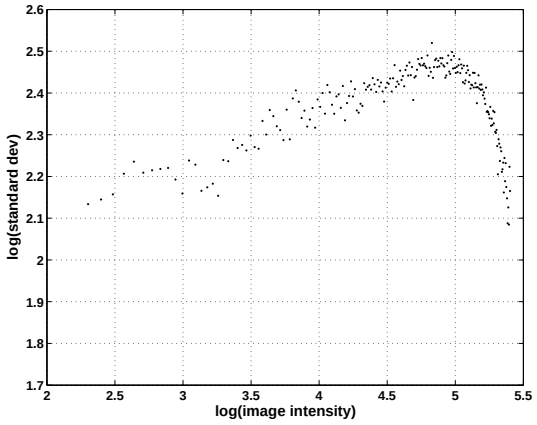

(c)

Figure 4.22: Noise curves corresponding to standard images "Gauge" (a), " Lena" (b), and "Peppers" (c), when γ and σ_u are 0.6 and 0.06 respectively in light space. Breakpoints are located at $e^{3.2}$ and e^5.

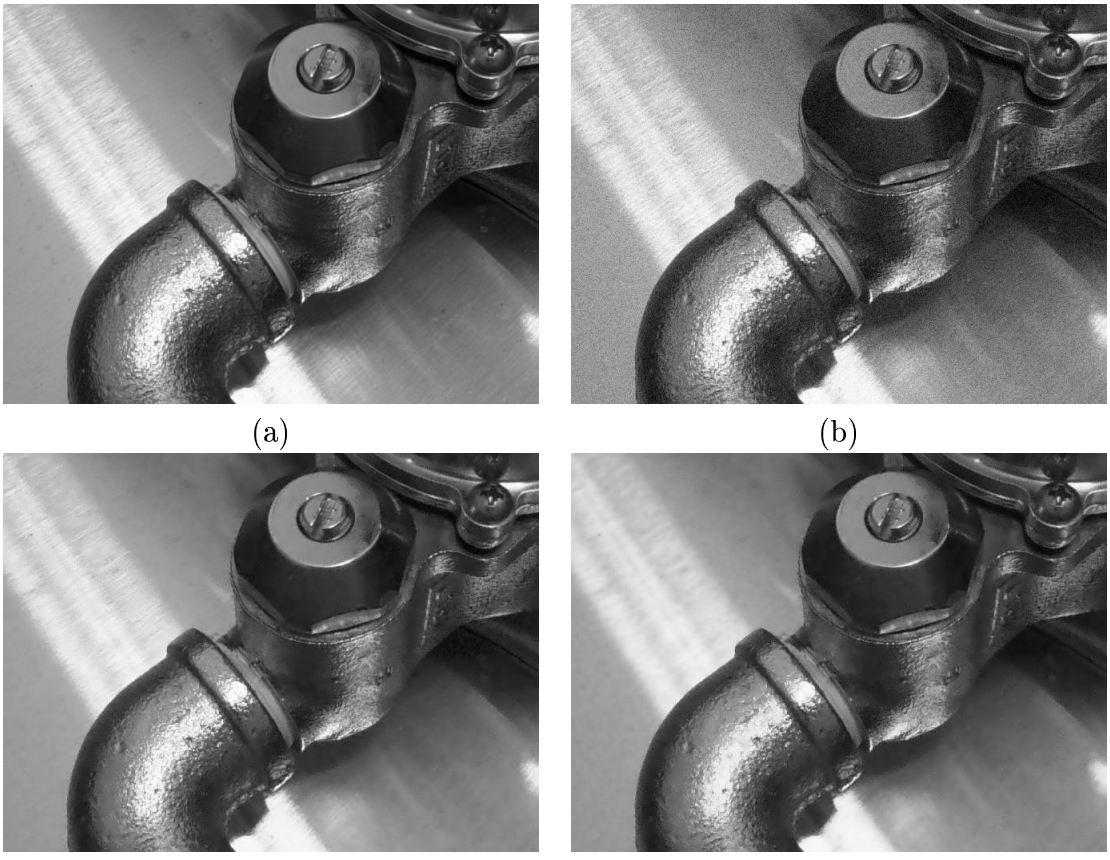

(a) (b)

(c) (d)

Figure 4.23: Cropped noise-free "Gauge" image (a), along with the noisy image (b), filtered image in light space (c), and filtered image in image space (d). Noise parameters γ and σ_u are 0.6 and 0.06 respectively.

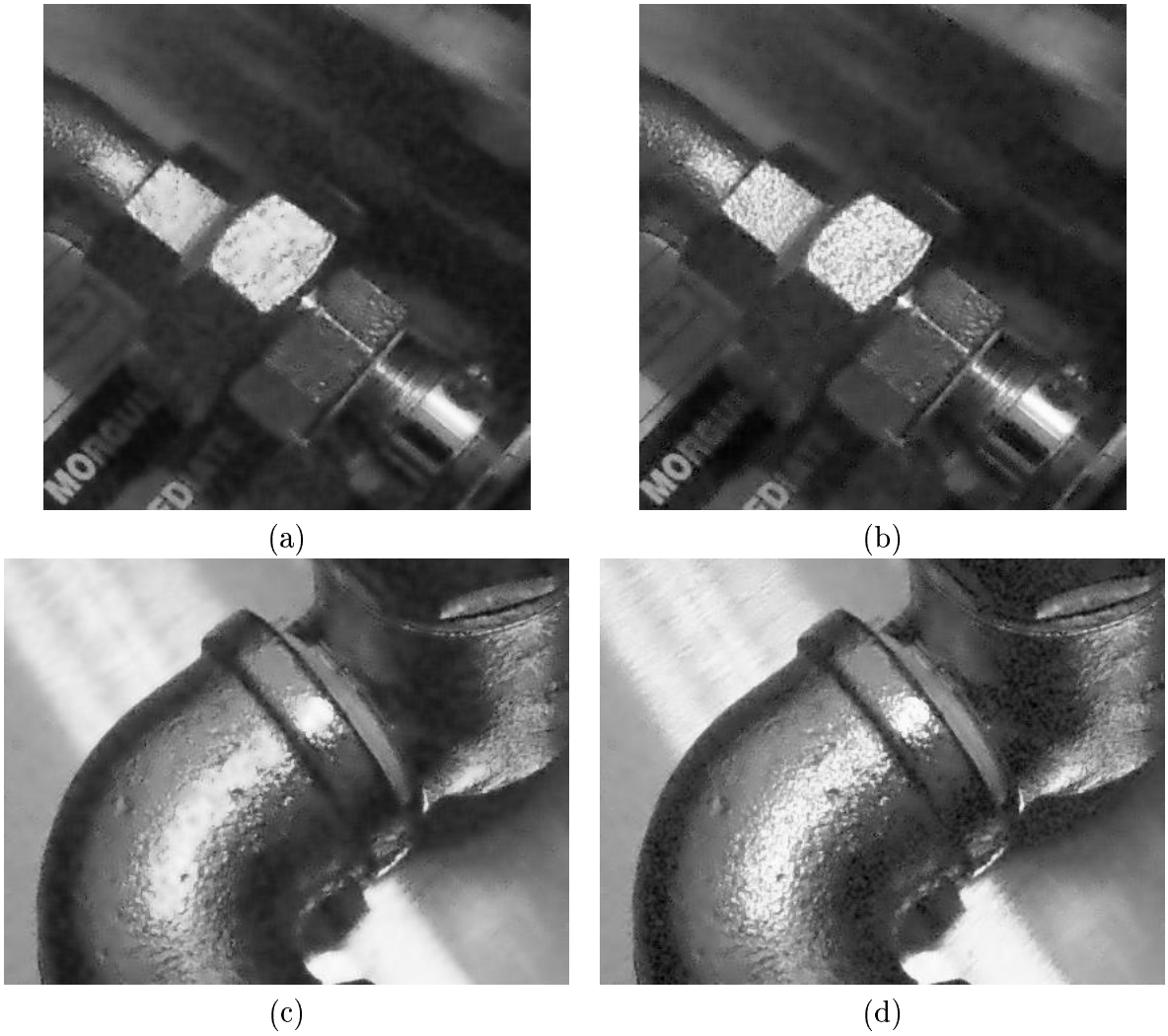

(a) (b)

(c) (d)

Figure 4.24: Cropped "Gauge" image denoised in image space (a) and (c) along with the denoised image in light space (b) and (d). The bright areas in (a) seem to have lost contrast as a result of heavy denoising, while in (b) all fine details are preserved.

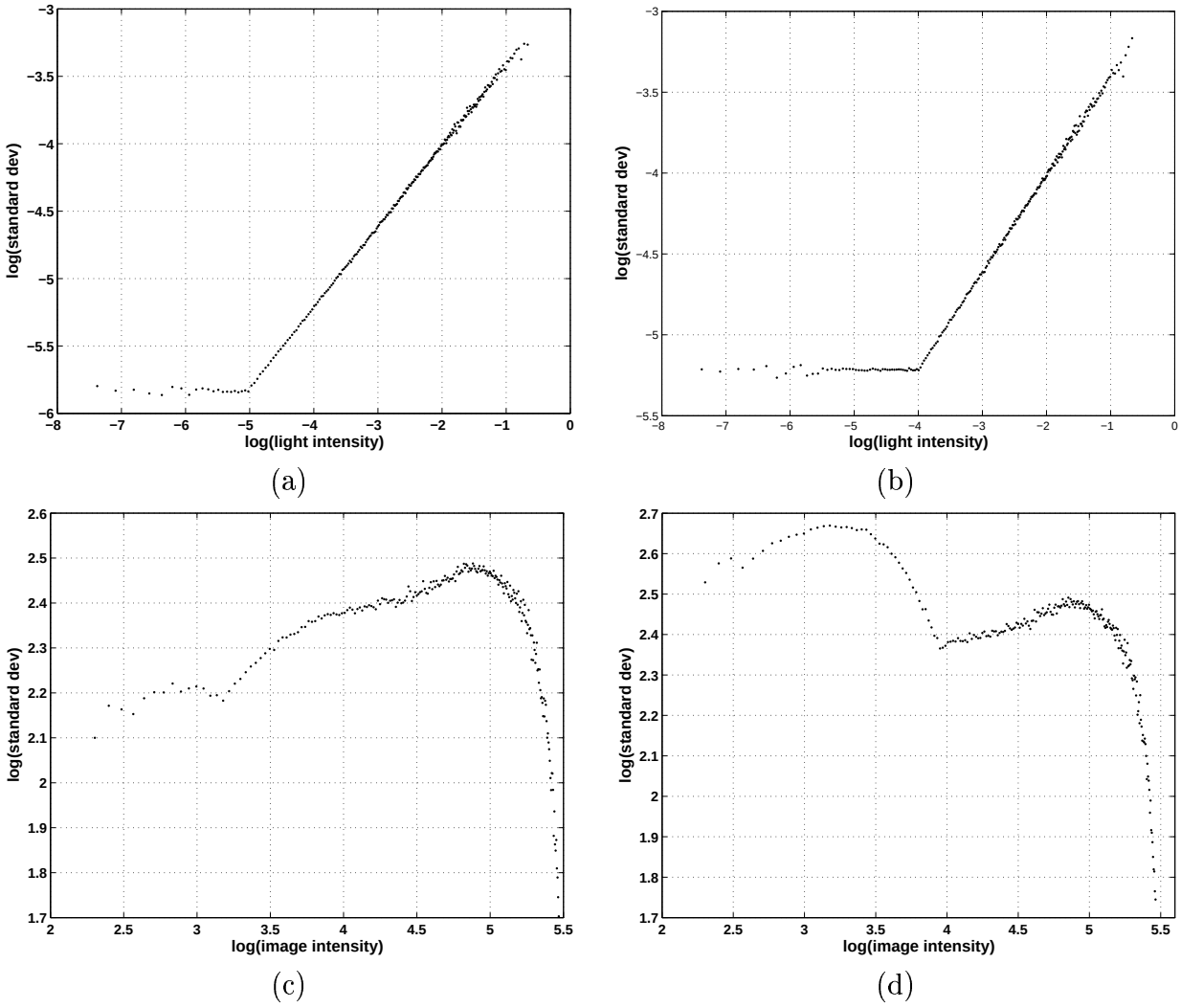

Figure 4.25: Noise curve corresponding to the "Gauge" image. Curves in (a) and (b) show the noise curves with breakpoints at e^{-5} and e^{-4} in light space. The image space noise curves are shown in (c)-(d). A shift in the breakpoint can considerably change the noise curve in image space. Therefore the filtering algorithm applied on (c), is not applicable in case of (d).

Chapter 5

Conclusion and future work

5.1 Conclusion

Digital images are prone to a variety of CCD noise sources, which can seriously restrict the ability to achieve high quality images with commercial sensors. Typically, restoration algorithms assume a linear mapping between the incident light space and image space. However, in practice a camera response function performs a nonlinear mapping on the sensor output and as a result the CCD noise model in image space is different from the typical photon transfer curve, and somewhat more complex. In this work we have presented two restoration algorithms for images degraded by CCD sensor noise. Both algorithms take into account this nonlinearity. One corrects for this nonlinearity by filtering in light space, where the relationship between the incident light and light space values is linear and noise model is simpler. The second method, filtering in image space, uses a version of the light space noise model transformed by the camera response function.

Denoising images degraded by CCD noise requires an appropriate sensor noise model. Access to the sensor data is necessary in order to obtain the proper CCD sensor noise model. To estimate the noise model in light space, we have estimated the sensor data by representing a series of test images in light space. These images, exhibiting most of the

dynamic range, were captured at the same exposure level and represented the same scene. This allowed us to compute the variations in any intensity and therefore generate the light space noise model. The resultant noise model, which resembles a photon transfer curve, exhibits three noise regions. For low signal levels, noise is dominated by read-out noise which is independent of signal and has constant power. The second and third noise regions are dominated by shot-noise and fixed pattern noise. Our recovered noise model in light space verifies this. We also generated the corresponding CCD noise model in image space; this is the noise model which our image space restoration algorithm is based on. The results show that regardless of any domain, characteristic noise associated with CCD sensors can be modeled as a signal-dependent process, for which the degree of dependency on the noise-free signal varies as a function of intensity.

The adaptive restoration algorithms presented in this thesis involve applying multiple adaptive noise smoothing (ANS) filters so that the non-stationary characteristics of both noise and image are taken into account. These filters are in principle a nonlinear modification of LLMMSE estimates, which use local statistics of signal and noise through two separate moving windows. The algorithm changes operation according to the ratio of the local signal variance to local noisy signal variance. To smooth the uniform areas, while preserving the image boundaries, an LNMSE is developed as a combination of two ANS filters with different window sizes. Several test images with signal-independent and signal-dependent noise at various noise levels were used to evaluate the performance of our denoising algorithms by comparing the filtered images with the original images. The results corresponding to any noise region are then smoothly blended using intensity maps. The experimental results illustrate that our final combined filter outperforms adaptive Wiener, LLMSE, and LNMSE filters by smoothing uniform regions and avoiding artifacts around the edges, the blurriness of the Wiener filter, and the remaining errors in the dark regions.

A comparison of the performance of light space denoising and image space restoration

demonstrates that both techniques yield almost equally satisfactory results, both qualitatively and quantitatively. Nevertheless light space denoising enables the design of a simpler restoration algorithm due to the simpler noise model in light space. In addition, denoising in light space is computationally less demanding, since less filters need to be developed and applied in light space. This is because the noise model in light space is reasonably assumed to consist of only two noise regions. Moreover, for the same noise parameters, a shift in the breakpoint partitioning the two noise regimes in the PHTC may considerably change the shape of the image space noise curve, which may then require a more complex denoising scheme. It should also be mentioned that light space denoising is superior when dealing with bright regions. This is because an adaptive Wiener filter in image space, when operating in light regions, does not achieve its optimal performance in the presence of signal-dependent noise. This needs further investigation in image space.

Overall, simulation results show promising performance; uniform regions are smoothed, while abrupt changes such as edges are preserved. We summarize the main contributions of this research as follows

- We design a new software-based CCD noise removal technique based on the standard electronic noise model (PHTC).

- The effect of the nonlinear camera response function is accounted for in both denoising schemes.

- We apply multiple filters to a single corrupted image, each of which deals with one noise region in the noise model. We then combine the results of these filters to give the final output by using a proper intensity map.

- We also reduce the side effect of ANS filters in the edge regions, by applying a combination of ANS filters with different window sizes.

5.2 Future work

There are some issues in our work that require further study and experiments. In the following sections we briefly highlight these concerns.

5.2.1 Noise model

In our experiments to generate the photon transfer curve, we used a large number of images at a fixed exposure time. To reduce the number of images, this curve can be generated by collecting multiple images corresponding to a standard uniform scene at different exposure levels. First the images are converted to light space. The noise-free sensor data are then estimated as the average of light space values over the entire image. Thus each image yields one point on the PHTC. Since the scene object is uniform, the image variance can be used to model the total sensor noise variance. Therefore, there is no need to capture such a large number of images. This may make the procedure easier as it will allow us to compute the statistics spatially rather than temporally. However, since it is assumed that all the pixels in the image belong to the same ensemble, more attention should be paid to assure an even lighting setup.

As a future direction it is worth experimenting with several types of digital cameras, thus acquiring various photon transfer curves, and finally examining the possible differences in the noise curves.

In our work we assumed a two region noise model. For the next set of experiments we can carry out the flat-fielding process to remove the fixed pattern noise, so that the resultant noise curves are shot noise dominant for high intensities as well. In doing so we will make the two-region noise model assumption more valid.

5.2.2 Filtering algorithm

One disadvantage of ANS filters is the way they handle noise near edges. As a result of an inaccurate estimate of local mean and consequently local variance, the filtered images exhibit artifacts in the vicinity of edge areas. We reduced this problem by decreasing the size of neighborhood window on which the filter operated. This improves the final results considerably, but does not entirely eliminate the problem. Given the promising results, the performance and accuracy may be increased by incorporating an improved representation of the image domain in which the NMNV model is not violated in the presence of edges.

5.2.3 Image space denoising

As outlined earlier, one of the disadvantages of filtering in image space is dealing with bright regions. This is because the image space noise curve for bright intensities exhibits an abrupt decrease in the noise power. Neither our ANS filters nor the adaptive Wiener filter could handle this type of noise well. Therefore the design of a new filter to address this type of noise in image space needs to be investigated.

5.3 Outlook

Digital image restoration continues to be an on-going and wide research area. A variety of digital consumer products, which use digital images, are on the market today, and more on the horizon. In particular, consumer digital cameras provide great opportunities for the application of denoising algorithms , since a variety of sensor noise sources impair the image quality. The techniques developed in this thesis have the potential to improve image quality either in hardware or as a post-processing software procedure for consumer and industrial digital cameras.

Bibliography

[1] B. Aiazzi, L. Alparone, and S. Baronti. A robust method for parameter estimation of signal-dependent noise models in digital images. In *Proceeding of IEEE International Conference on Digital Signal Processing*, pages 601–604, July 1997.

[2] F. Argenti, G. Torricelli, and L. Alparone. Signal-dependent noise removal in the undecimated wavelet domain. In *IEEE International Conference on Acoustics, Speech, and Signal Processing Proceeding*, volume 4, pages 3293–3296, May 2002.

[3] M. Boudaoud and L.F. Chaparro. Nonstationary composite modeling of images. *IEEE Transactions on Systems, Man and Cybernetics*, 19(1):112–117, 1989.

[4] T. K. Darwin and A. Alexander. Adaptive noise smoothing filter for images with signal-dependent noise. *IEEE Transactions on Pattern Analysis and Machine Intelligence*, 7(2):165–177, 1985.

[5] G. E. Healey and R. Kondepudy. Radiometric CCD camera calibration and noise estimation. *IEEE Transactions on Pattern Analysis and Machine Intelligence*, 16(3):267–276, 1994.

[6] Roper Scientific Inc. Keep the noise down, low noise: an integral part of high-performance CCD (HCCD) camera systems. Technical report, Roper Scientific Inc., 1999.

[7] K. Anil Jain. *Fundamentals of Digital Image Processing.* Prentice Hall, 1989.

[8] J. Janesick. Dueling detectors. *SPIE, The international society of optical engineering magazine*, 4669A:30–33, 2002.

[9] James R. Janesick. *Scientific Charge-Coupled Devices.* SPIE Press, Bellingham, Wash., 2001.

[10] S. M. Kay. *Fundamentals of Statistical Signal Processing.* Prentice-Hall, 1993.

[11] J.S. Lim. *Two-Dimensional Signal and Image Processing.* Prentice-Hall, 1990.

[12] D. Litwiller. CCD vs. CMOS: facts and fiction. *Photonics Spectra*, 2001.

[13] C. Manders and S. Mann. Eigentracking in lights pace. Submitted to IEEE International Conference on Acoustics, Speech, and Signal Processing, 2004.

[14] Corey Manders. Comparametric lights pace imaging and analysis. Master's thesis, University of Toronto, 2002.

[15] S. Mann. Comparametric equations with practical applications in quantigraphic image processing. *IEEE Transactions on Image Processing*, 9(8):1389–1406, 2000.

[16] S. Mann, C. Manders, and J. Fung. The light space change constraint equation (lcce) with practical application to estimation of the projectivity+gain transformation between multiple pictures of the same subject matter. In *IEEE International Conference on Acoustics, Speech, and Signal Processing*, volume 3, pages 481–484, April 2003.

[17] S. Mann and R. Mann. Quantigraphic imaging: Estimating the camera response and exposures from differently exposed image. In *Proceeding of IEEE Computer Society Conference on Computer Vision and Pattern Recognition*, Kauai, Hawaii, December 2001.

[18] Steve Mann. *Intelligent Image Processing.* A John Wiley and Sons, INC., 2002.

[19] D.R. Mendoza. An analysis of CCD camera noise and its effect on pressure sensitive paint instrumentation system signal-to-noise ratio. In *Instrumentation in Aerospace Simulation Facilities, ICIASF*, pages 22–29, Pacific Grove, CA, USA, Sept. 1997.

[20] G. Pavlovic and A.M. Tekalp. Restoration in the presence of multiplicative noise with application to scanned photographic images. In *IEEE, IEEE International Conference on Acoustics, Speech, and Signal Processing*, pages 1913 –1916 (vol.4), NM, USA, 1990.

[21] I. Pitas and A.N.Venetsanopoulos. Order statistics in digital image processing. *Proceedings of the IEEE*, 80(12):1893–1921, 1992.

[22] I. Pitas and A.N. Venetsanopoulos. *Nonlinear Digital Filters; Principles and Applications*. Boston, MA: Kluwer, 1990.

[23] M. I. Sezan. Selected papers on digital image restoration. Technical report, Electronic Imaging Research Laboratories, 1992.

[24] B. G. Streetman. *Solid State Electronic Devices*. Prentice Hall, third edition, 1990.

[25] Microelectronics technology division. CCD primer, conversion of light to electronic charge. Technical report, Eastman Kodak company, 1999.

[26] H. Trussell and B. Hunt. Sectioned methods for image restoration. *IEEE, IEEE International Conference on Acoustics, Speech, and Signal Processing*, 26(2):157–164, 1978.

[27] Y. Tsin, V. Ramesh, and T. Kanade. Statistical calibration of CCD imaging process. *IEEE, International Conference on Computer Vision*, 1:480–487, 2001.

[28] T.L. Veldhuizen and M.E. Jernigan. Grid filters for local nonlinear image restoration. In *IEEE International Conference on Acoustics, Speech, and Signal Processing Proceeding*, pages 2885–2888 vol.(5), WA, USA, May 1998.

[29] H. Zhang. Spatially adaptive wiener filtering for image denoising using undecimated wavelet transform. Technical report, Rice University, 1999. URL: http://citeseer.nj.nec.com/zhang99spatially.html.